

Design procedures for Strain Hardening Cement Composites (SHCC) and measurement of their
shear properties by mechanical and 2-D Digital Image Correlation (DIC) method

by

Karan Aswani

A Thesis Presented in Partial Fulfillment
of the Requirements for the Degree
Master of Science

Approved April 2014 by the
Graduate Supervisory Committee:

Barzin Mobasher, Chair
Subramaniam Dharmarajan
Narayanan Neithalath

ARIZONA STATE UNIVERSITY

May 2014

ABSTRACT

The main objective of this study is to investigate the behaviour and applications of strain hardening cement composites (SHCC). Application of SHCC for use in slabs of common configurations was studied and design procedures are prepared by employing yield line theory and integrating it with simplified tri-linear model developed in Arizona State University by Dr. Barzin Mobasher and Dr. Chote Soranakom. Intrinsic material property of moment-curvature response for SHCC was used to derive the relationship between applied load and deflection in a two-step process involving the limit state analysis and kinematically admissible displacements. For application of SHCC in structures such as shear walls, tensile and shear properties are necessary for design. Lot of research has already been done to study the tensile properties and therefore shear property study was undertaken to prepare a design guide. Shear response of textile reinforced concrete was investigated based on picture frame shear test method. The effects of orientation, volume of cement paste per layer, planar cross-section and volume fraction of textiles were investigated. Pultrusion was used for the production of textile reinforced concrete. It is an automated set-up with low equipment cost which provides uniform production and smooth final surface of the TRC. A 3-D optical non-contacting deformation measurement technique of digital image correlation (DIC) was used to conduct the image analysis on the shear samples by means of tracking the displacement field through comparison between the reference image and deformed images. DIC successfully obtained full-field strain distribution, displacement and strain versus time responses, demonstrated the bonding mechanism from perspective of strain field, and gave a relation between shear angle and shear strain.

ACKNOWLEDGEMENTS

I would like to specially thank my advisor Dr. Barzin Mobasher, who provides me the opportunity to work in the field of research that I could go through variety of excited topics and experimental programs. Let alone all the attention, invaluable intellectual insights he gave me. I also want to extend my appreciation to Dr. Subramaniam D. Rajan and Dr. Narayanan Neithalath who served as my committee members, helping and supervising my progress in Master's degree program.

I would also like to thank Vikram Dey, who actually taught me many skills including preparing and conducting experiment, data analysis and all of his supports and ideas throughout my research work. Outstanding work done by my peers, Dr. Deju Zhu and Dr. Chote Soranakom established the basis and a straight forward path that I could follow up and extended my work to further areas.

I greatly appreciate the assistance provided by Mr. Peter Goguen and Mr. Kenny Witczak for all of their great works in the laboratory, especially the trouble-shooting and maintenance on testing devices. Without their help, I could definitely not finish my experiments.

Absolutely, I would express my gratitude to my dear colleagues and friend, Yiming Yao, Robert Kachala and Xinmeng Wang for their help and more importantly, the great time we spent together.

TABLE OF CONTENTS

| CHAPTER | Page |
|---|------|
| LIST OF FIGURES | vii |
| LIST OF TABLES | xii |
| CHAPTER 1 - INTRODUCTION..... | 1 |
| 1.1 Overview | 1 |
| 1.1.1 Strain Hardening Cement Composite | 2 |
| 1.1.2 Textile Reinforced Concrete as a Strain Hardening Cement Composite..... | 2 |
| 1.1.3 Materials | 4 |
| 1.2 Simplified Strain-hardening Cement composites (SHCC) Model | 5 |
| 1.2.1. Derivation of Moment-Curvature Capacity | 8 |
| 1.3 Production Techniques..... | 15 |
| CHAPTER 2 - LIMIT STATE ANALYSIS OF STRAIN HARDENING STRUCTURAL PANELS..... | 18 |
| 2.1 Yield Line Analysis Approach..... | 20 |
| 2.2 2-D Analysis of Panels for Moment-Load Relationship..... | 21 |
| 2.2.1 Case 1 – Applied Load vs. Yield Line Moment Relationship for Square Slabs..... | 21 |
| 2.2.2 Case 2- Applied Load vs. Yield Line Moment Relationship for Rectangular Slabs..... | 26 |
| 2.2.3 Case 3 - Applied Load vs. Yield Line Moment for Round Panels | 32 |

| CHAPTER | Page |
|---|---|
| 2.3 | Analysis of Panels for Curvature-Deflection Relationship35 |
| 2.3.1 | Hinge Length, L^*35 |
| 2.3.2 | Curvature-Deflection Relationship for a Square Slab37 |
| 2.3.3 | Curvature-Deflection Relationship for Rectangular Slab39 |
| 2.3.4 | Curvature-Deflection Relationship for Round Panels46 |
| 2.4 | Applied load - Deflection Response.....48 |
| 2.5 | Shortcomings of the Methodology - Increased Load Bearing Strength at Large Vertical Displacements49 |
| 2.6 | Comparison with Experimental Data50 |
| 2.6.1 | Data Set 150 |
| 2.6.2 | Data Set 255 |
| 2.7 | Interaction of the Different Tensile Zones on the Load-Deflection Response of the Panels Based on the Moment-Curvature and Limit Analysis59 |
| 2.8 | Post-Crack Analysis of ASTM C1550 Test results using the Proposed Yield Line Load-Deflection Model64 |
| CHAPTER 3 - SHEAR PROPERTIES OF TEXTILE REINFORCED CONCRETE BY MECHANICAL TESTS AND DIGITAL IMAGE CORRELATION67 | |
| 3.1 | Experimental Program.....69 |
| 3.2 | Shear Test Procedure and Instrumentation.....70 |
| 3.3 | Data Reduction Methods73 |
| 3.3.1 | Determination of Shear Force73 |

| CHAPTER | Page |
|--|------|
| 3.3.2 Determination of Shear Angle | 75 |
| 3.3.3 Determination of Shear Strain | 77 |
| 3.1 Digital Image Correlation (DIC) method | 78 |
| 3.1.1 Introduction and applications..... | 78 |
| 3.1.2 DIC discipline | 81 |
| 3.2 Experimental Parameters..... | 86 |
| 3.3 Analysis of Test Data | 89 |
| 3.4 Test Results | 89 |
| 3.5 Discussion of Experimental Results..... | 94 |
| 3.6 Effect of Thickness..... | 95 |
| 3.7 Effect of Orientation..... | 96 |
| 3.8 Effect of Planar Cross-section..... | 99 |
| 3.9 Effect of Textile Type | 100 |
| 3.10 Conclusion of Results..... | 102 |
| 3.11 Digital Image Correlation Results..... | 104 |
| 3.12 Discussion of Digital Image Correlation results | 108 |
| 3.13 Relationship between Shear Angle and Shear Strain | 109 |
| 3.14 Constitutive Model for Calculating Shear Stress | 111 |
| 3.1 Crack Pattern | 113 |
| 4. REFERENCES | 119 |

LIST OF FIGURES

| Figure | Page |
|--|------|
| 1.1 Textile Reinforced Concrete | 4 |
| 1.2 Full option material models for both strain-hardening and strain-softening material: (a) tension model; and (b) compression model | 7 |
| 1.3 Strain and stress diagrams at the post crack stage (Ranges 2.1 and 3.1 - Table 1-2), (a) strain distribution; and (b) stress distribution | 8 |
| 1.4 Effect of a) Depth of Neutral axis on the moment capacity of a section, and b) the moment curvature response in the Range 2.1 | 12 |
| 1.5 Schematics of pultrusion process..... | 15 |
| 1.6 Pultrusion setup with motors attached to the rollers..... | 16 |
| 1.7 Hand lay-up..... | 17 |
| 1.8 Hydraulic press | 17 |
| 2.1 Process for applied load-deflection derivation | 19 |
| 2.2 Construction and applications of SHCC material slabs [] | 20 |
| 2.3 Simply supported square Panel with (a) yield lines and (b) loading and rotation conditions through section A-A. | 23 |
| 2.4 Applied load and yield line moment for a clamped square slab. | 24 |
| 2.5 Two sides clamped and other two sides simply supported rectangular slab..... | 27 |
| 2.6 Applied load and yield line moment for a rectangular slab clamped on three sides and free on fourth..... | 31 |
| 2.7 Principle of virtual work to determine the ultimate load carrying capacity of a round panel test simply supported in its contour and subjected to center point load..... | 33 |

| Figure | Page |
|--|------|
| 2.8 Hinge rotation mechanism (a) Steel fiber reinforced beam (BASF), (b) Rigid body hinge rotation [16]..... | 36 |
| 2.9 Load-deflection relationship for Square slab | 37 |
| 2.10 Planes AED and EBC | 37 |
| 2.11 Load-deflection relationship for Rectangular slab..... | 40 |
| 2.12 Planes KON and PLM | 41 |
| 2.13 Planes KON and NOPM | 42 |
| 2.14 Load-deflection for rectangular slab fixed from 3 sides and free from fourth | 44 |
| 2.15 Deflection-curvature relationship when yield lines are not at 45° | 44 |
| 2.16 Load-deflection relationship for Circular slab | 46 |
| 2.17 Flowchart for the derivation of applied load-deflection relationship for SHCC materials | 49 |
| 2.18 Different zones for slabs subjected to large displacements [21]..... | 50 |
| 2.19 Strain hardening-softening tension model with the parameters used for fitting the model ($\eta=0.01$, $\mu=0.6$, $\alpha=5$)..... | 53 |
| 2.20 Comparison of experimental results with methodology for round panels | 54 |
| 2.21 Effect of hinge length on simulated results..... | 55 |
| 2.22 Experimental results for square slabs [23]..... | 56 |
| 2.23 Comparison of experimental results with the methodology for square panels | 58 |
| 2.24 Problem parameters | 59 |
| 2.25 Moment-curvature relationship for SHCC..... | 62 |

| Figure | Page |
|--|------|
| 2.26 Moment-load response for (a) uniformly distrib. load, (b) point load at center. | 62 |
| 2.27 Deflection-curvature relationship | 63 |
| 2.28 (a) Applied load-deflection relationship | 63 |
| 2.29 (b) Equivalent applied load-deflection relationship..... | 64 |
| 2.30 Round panel tests (a) Test set up, (b) Comparison between the experimental data and simplified model based on Johansen’s formula | 66 |
| 3.1 Methods of measuring shear force – (a) direct shear force measurement and (b) picture frame test..... | 68 |
| 3.2 Standard Hobart mixer | 69 |
| 3.3 Test set-up | 71 |
| 3.4 Schematics of test set-up..... | 72 |
| 3.5 Different stages of experiment..... | 73 |
| 3.6 Schematics of picture frame tests | 73 |
| 3.7 Free body diagram for link BC | 74 |
| 3.8 Simplified Free body diagram for link BC | 74 |
| 3.9 Initial configuration | 76 |
| 3.10 Configuration after a displacement of D units | 76 |
| 3.11 Theoretical shear strain | 77 |
| 3.12 Setup of the 3D digital image correlation | 80 |
| 3.13 Tracking at different instances [] | 81 |
| 3.14 Mapping from original to deformed subset | 82 |
| 3.15 Speckled samples | 82 |

| Figure | Page |
|---|------|
| 3.16 Terms involved in correlation [56] | 83 |
| 3.17 Correlation of a displaced surface [56]..... | 84 |
| 3.18 Displacement tracking in 3D fields [56]..... | 85 |
| 3.19 Schematics for 3D image analysis [56] | 85 |
| 3.20 Load-deflection response for S1-T1- 0° | 90 |
| 3.21 Load-deflection response for S2-T1- 0° | 90 |
| 3.22 Load-deflection response for S1-T1- 45° | 91 |
| 3.23 Load-deflection response for S1-T2- 0° | 92 |
| 3.24 Load-deflection response for S1-T2- 45° | 93 |
| 3.25 Load-deflection response for Textile 2 - S1-T2- 0° | 94 |
| 3.26 Shear stress versus shear angle response for comparison between the two thicknesses - T1 (5.00 mm) and T2 (6.5 mm) for both the orientations | 96 |
| 3.27 Orientations before and after cutting | 97 |
| 3.28 Shear stress versus shear angle response for comparison between the two orientations- 0° and 45° for both the thicknesses | 98 |
| 3.29 Pictures of different planar cross-section..... | 99 |
| 3.30 Dimensions of the two planar cross-section | 99 |
| 3.31 Shear stress versus shear angle response for S1 and S2 | 100 |
| 3.32 Two textiles used in this study..... | 101 |
| 3.33 Shear stress versus shear angle response for textile 1 vs textile 2 | 101 |
| 3.34 Shear strength summary..... | 102 |
| 3.35 Shear strain from DIC versus shear angle..... | 110 |

| Figure | Page |
|---|------|
| 3.36 Shear strain from DIC versus shear angle..... | 111 |
| 3.37 Constitutive model to calculate the shear stress | 112 |
| 3.38 Different stage during the experiment | 113 |
| 3.39 Crack pattern for S1 – T1 - 0°..... | 114 |
| 3.40 Crack pattern for S1 – T1 - 45°..... | 114 |
| 3.41 Crack pattern for S2 – T1 - 0°..... | 115 |
| 3.42 Crack pattern for S1 – T0 - 0°..... | 116 |
| 3.43 Crack pattern for S1 – T2 - 0°..... | 117 |
| 3.44 Crack pattern for Textile 2 – S1 – T2 - 0° | 117 |

LIST OF TABLES

| Tables | Page |
|--|------|
| 2-1 : Applied load – yield line moment relationship for Cases 1.1 to 1.3 | 25 |
| 2-2 : Applied load – yield line moment relationship for Cases 2.1 to 2.4 | 29 |
| 2-3 : Applied load – yield line moment relationship for Cases 3.1 and 3.2..... | 34 |
| 2-4 : Empirically derived hinge lengths | 36 |
| 3-1 : Mix design | 69 |
| 3-2 : Parameters tested and their levels..... | 87 |
| 3-3 : Test combinations used in the experiment | 88 |
| 3-4 : Summary of test results | 95 |

1. CHAPTER 1 - INTRODUCTION

1.1 Overview

The civil engineering profession recognizes the reality of limited natural resources, the desire for sustainable development and the need for conservative consumption of resources. On a global level, there is a great demand of building material to sustain the exponential growth of infrastructure [1]. Concrete being one of the most consumed building materials; a lot of research is going on in increasing its durability, designing light weight structural members, developing building systems with low cement and utilizing renewable energy resources. Lowering the cost of building materials is also one of the key aspects of sustainable infrastructure especially in the developing nations. Plain concrete has always been known to be a brittle material with weak tension capacities. Fabric based cement composites aid in improving tensile strength and stiffness along with introduction of ductility in the infrastructure systems and come under the broad category of strain hardening or strain softening cement composites [2]. Therefore strain hardening cement composites (SHCC) such as textile reinforced concrete have become integral research topic. Applications of SHCC material has been further extended to panels and shear elements due to their improved performance taking into account serviceability and sustainability. This study is majorly based on evaluating the performance of strain hardening cement composites for improving durability and ductility.

1.1.1 Strain Hardening Cement Composite

Strain hardening materials are well suited for applications that eliminate conventional reinforcement or for the structures in seismic regions where high ductility is desired. In addition, these materials offer fatigue and impact resistance and are attractive for use in industrial structures, highways, bridges, earthquake, hurricane, and high wind loading conditions. The design and implementation of these systems requires one to acknowledge and use the strain-hardening response that is attributed to multiple cracking. Propagation of initial crack in strain hardening composites is resisted by bridging mechanism. Since a substantial amount of energy is required to further extend existing cracks, secondary cracks form. Single crack localization is therefore shifted to multiple distributed cracking mechanisms, leading to macroscopic pseudo-strain hardening behaviors. The dominant toughening mechanisms in these systems are attributed to matrix cracking, ply delamination, and crack deflection mechanisms as studied by means of fluorescent microscopy and scanning electron microscopy.

1.1.2 Textile Reinforced Concrete as a Strain Hardening Cement Composite

Reinforcement is commonly combined with plain concrete to enhance its tensile strength [3]. There are various types of materials and forms used for reinforcing, but the most common is round steel bars with ribs. Reinforced concrete structures with steel are vulnerable to corrosion attack if the protective medium provided by concrete is weakened. In an attempt to improve the durability, other reinforcement options such as stainless steel bars, epoxy-coated steel bars, fiber-reinforced polymer (FRP) bars, steel welded-wire fabric, and fibers (steel and synthetic) have been explored. A recent

innovative attempt to improve the sustainability of reinforced concrete is the development of Textile Reinforced Concrete (TRC). It was discovered that TRC can be utilized to build slender, lightweight, modular and freeform structures and eliminate the risk of corrosion. TRC provides high strength in compression and tension and is proven to be a suitable option for the strengthening of existing structures. This composite material is fabricated using a fine-grained concrete matrix reinforced by multi-axial textile fabrics. The underlying concept of TRC is based on a combination of traditionally used reinforcement bars and FRC, wherein the shortcomings of both reinforcement methods, namely durability and design control, are overcome. TRC is explored as a sustainable solution because its design minimizes the use of binder material such as concrete, which when made of Portland cement is one of the most pollutant and energy consuming building materials used in the construction industry. Focusing on the reduction and replacement of energy-intensive materials like Portland cement not only helps to reduce the extraction of natural resources but also to reduce the high energy demands of the production process. The use of textile reinforcement made from non-corrosive materials, such as carbon and glass can reduce the required concrete material by up to 85%. Typical mechanical properties of the textile reinforced concrete measured using uniaxial tensile, flexural, and shear tests indicate that the tensile strength of around 25 MPa, and strain capacity of 1-8% [4]. The fracture toughness as compared to the conventional FRC materials is increased by as much as two orders of magnitude. For Textile Reinforced Concrete applications, bi- or multi-axial 2D and 3D textile meshes can be used as reinforcement. For a simple bi-axial case, the mesh comprises two groups of textile fiber yarns (threads), warp (0°) and weft (90°), interwoven perpendicularly to

each other. Yarns are composed of multiple single fibers of continuous length, also designed as filaments; grouping of continuous fibers is primarily done to obtain the desired thickness of yarn. Fabrication methods related to textile meshes are abundant and can be tailored to the needs of nearly any given application. In the case of TRC, an open-grid structure and displacement stability are favored in order to allow for adequate penetration of a cementitious matrix, whilst ensuring a relatively constant woven mesh structure in composite form.

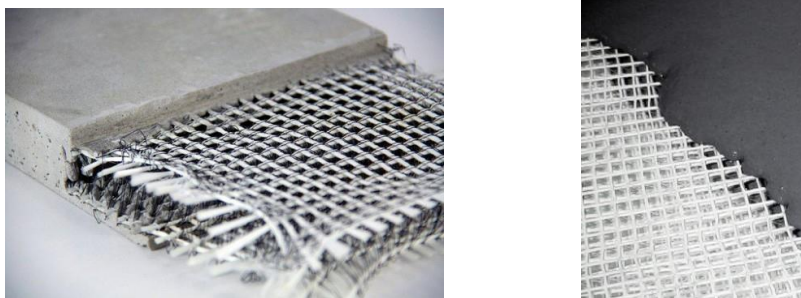


Figure 1.1 Textile Reinforced Concrete

1.1.3 Materials

The choice of fiber material for use in TRC is based on various factors such as material properties, corrosion and temperature resistance, bond quality, demand/production cost and even environmental impact. In terms of mechanical behavior, tensile strength, breaking elongation and modulus of elasticity superior to those related to the cementitious matrix is essential. The reinforcement ratio and placement of the textile reinforcement will also have a great impact on the composite behavior of a TRC member. Fiber materials which have generally been used and explored in TRC include, but are not limited to: alkali-resistant glass (AR-glass), carbon, basalt, aramid, polyvinyl-alcohol (PVA) with polyvinyl chloride (PVC) coating. In this thesis, only AR-glass has been explored, as it is the most readily available and applied material.

Glass fibers are chemical fibers derived from inorganic non-metallic raw materials. The raw materials needed to produce AR-glass are primarily silica sand (SiO_2) and the addition of zircon (ZrO_2) to provide superior alkali resistance, which are proportioned through a batching process. These raw materials undergo a melting process between 1250 to 1350°C, wherein molten glass is yielded. Fiberization of the molten glass takes place afterwards, meaning that fibers are produced through a wet-spinning process. The glass fiber filaments are then sized to primarily protect them against damage during packaging and finishing. Coating is often applied during sizing to obtain a specified surface wetting and bonding of the filaments. AR Glass used in this study had a tensile strength in range of 1270 – 2450 MPa and modulus of elasticity of 78 MPa.

1.2 Simplified Strain-hardening Cement composites (SHCC) Model

In strain hardening cement composites fabric systems are used with an efficient interface bond which enhances load transfer across a matrix crack. If fiber volume fraction is higher than a critical level, the entire load can be transferred through the fiber, and subsequent cracking of the matrix can take place leading to distributed cracking and significant strain capacity. Effect of distributed cracking on the stiffness degradation of the composite under tensile loading is then used to represent the reduction in the modulus and stiffness of the sample in the tension, allowing for the strain capacity to be included in the design procedure. Using damage function modeling, the post crack stiffness is calibrated by predicting the ultimate strength of composites under tensile and compressive loading and the results are utilized to correlate the distributed cracking in strain hardening composites with various fiber types and contents under tension [5].

Application of strain compatibility analysis to a new constitutive model requires layer discretization, iterative solution for neutral axis, and numerical integration to determine moment and curvature at each strain increment. Since the compression and tension response of various cement composites listed above are relatively close, closed-form solution of moment-curvature diagram, derived for a generic material can be used to predict flexural behavior of homogenized fiber/fabric reinforcement. Closed form solutions of a moment-curvature relationship can also be directly implemented in a structural analysis code, and/or spreadsheets.

A general strain hardening tensile, and an elastic perfectly plastic compression model as derived by Soranakom and Mobasher [6] [7] [8] and shown in figure 1.2 is used. Tensile response is defined by tensile stiffness, E , first crack tensile strain, ε_{cr} , Cracking tensile strength, $\sigma_{cr} = E\varepsilon_{cr}$, ultimate tensile capacity, ε_{peak} , and post crack modulus, E_{cr} . The softening range is shown as a constant stress level, $\mu E\varepsilon_{cr}$. The compression response is defined by the compressive strength, σ_{cy} defined as $\omega\gamma E\varepsilon_{cr}$. In order to simplify material characteristics of strain-hardening material, and yet obtain closed form design equation generation several assumptions are made. Equations can furthermore be simplified to idealized tri-linear tension and elastic compression models as shown in figure 1.2 (a) and (b) by ignoring the post-peak ranges in both tension and compression. In order to reduce the complexity of material response to the useable range, one has to disregard the post-peak tensile response and plasticity in the compression region. It has been shown that the difference in compressive and tensile modulus has negligible effect to the ultimate moment capacity. By defining all parameters as normalized with respect

to minimum number of variables, closed form derivations are obtained. Applied tensile and compressive strains at bottom and top fibers, β , and λ are defined as

$$\beta = \frac{\varepsilon_t}{\varepsilon_{cr}}, \quad \lambda = \frac{\varepsilon_c}{\varepsilon_{cr}} \quad (1-1)$$

Material parameters required for the simplified models are summarized as follows. Parameters, α , μ , η , ω , are defined respectively as representing normalized, tensile strain at peak strength, post-crack modulus, compressive yield strain:

$$\alpha = \frac{\varepsilon_{peak}}{\varepsilon_{cr}}, \quad \eta = \frac{E_{cr}}{E}, \quad \omega = \frac{\sigma_{cy}}{E\varepsilon_{cr}} = \frac{\sigma_{cy}}{\sigma_{cr}} \quad (1-2)$$

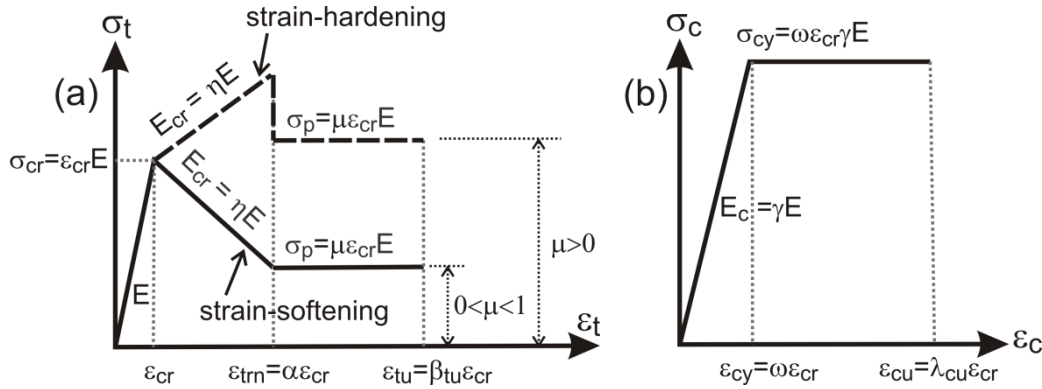


Figure 1.2 Full option material models for both strain-hardening and strain-softening material: (a) tension model; and (b) compression model

For typical strain-hardening material, the compressive strength is several times higher than the tensile strength. Thus, the flexural capacity is controlled by the weaker tension and the compressive stress is normally low in the elastic range. For this reason, the elastic compression model as shown in figure 1.2(b) is used. For the development of design equations, the compressive stress developed in a beam section is limited to the yield

compressive stress $\sigma_{cy} = 0.85f_c'$ at compressive yield strain ϵ_{cy} , where f_c' is the uniaxial compressive strength.

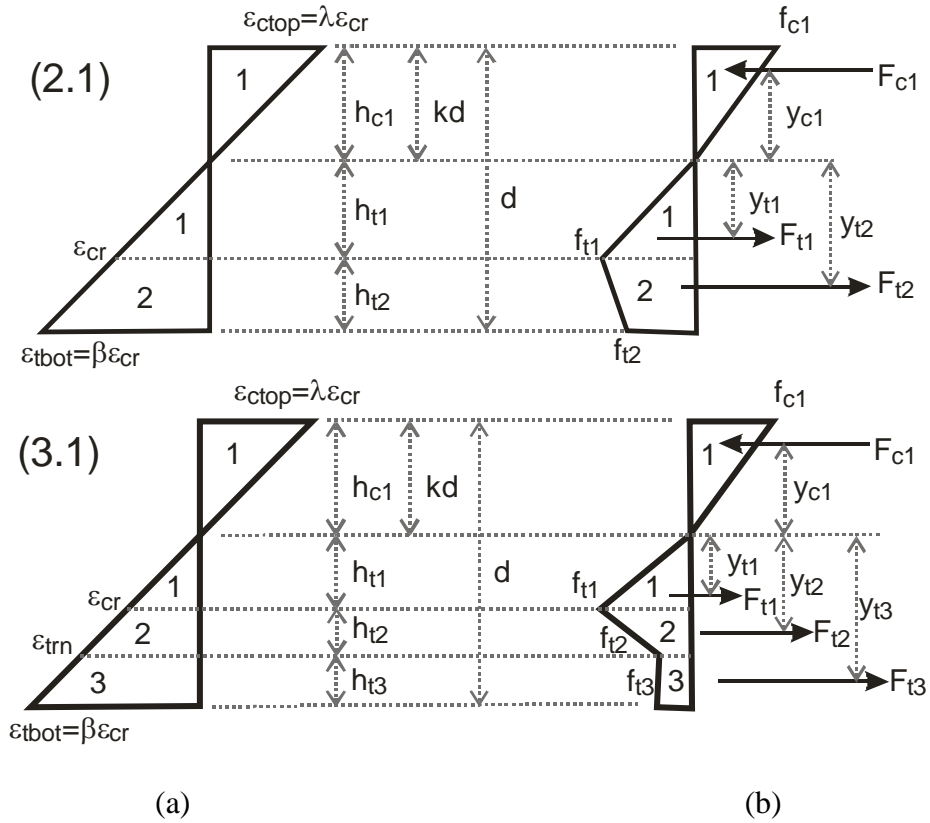


Figure 1.3 Strain and stress diagrams at the post crack stage (Ranges 2.1 and 3.1 - Table 1-2), (a) strain distribution; and (b) stress distribution

1.2.1. Derivation of Moment-Curvature Capacity

Moment capacity of a beam section according to the imposed tensile strain at the bottom fiber ($\epsilon_t = \beta\epsilon_{cr}$) can be derived based on the assumed linear strain distribution as shown in Fig. 2(a). By using material models described in figure 1.2 (a) and (b), the corresponding stress diagram is obtained as shown in figure 1.3 (b) in which the stress distribution is subdivided into a compression zone 1, tension zone 1 and 2. Force components and their centroidal distance to the neutral axis in each zone can be expressed as:

$$\frac{F_{c1}}{bh\sigma_{cr}} = \frac{\beta\gamma k^2}{2(1-k)}; \quad \frac{y_{c1}}{h} = \frac{2}{3}k \quad (1-3)$$

$$\frac{F_{t1}}{bh\sigma_{cr}} = \frac{(1-k)}{2\beta}; \quad \frac{y_{t1}}{h} = \frac{2(1-k)}{3\beta} \quad (1-4)$$

$$\frac{F_{t2}}{bh\sigma_{cr}} = \frac{(1-k)(\beta-1)(\eta\beta-\eta+2)}{2\beta}; \quad \frac{y_{t2}}{h} = \frac{2\eta\beta^2 - \eta\beta - \eta + 3\beta + 3}{3\beta(\eta\beta - \eta + 2)}(1-k) \quad (1-5)$$

where F and y are the force and its centroid, respectively; subscripts $c1, t1, t2$ designate compression zone 1, tension zone 1 and 2, respectively; b and h are the width and the height of the beam, respectively. The neutral axis parameter k is found by solving the equilibrium of net internal forces equal to zero, $F_{c1} + F_{t1} + F_{t2} = 0$.

$$k = \frac{C_1 - \sqrt{\beta^2 C_1}}{C_1 - \beta^2}; \quad \text{where } C_1 = \eta(\beta^2 - 2\beta + 1) + 2\beta - 1 \quad (1-6)$$

The nominal moment capacity M_n is obtained by taking the first moment of force about the neutral axis, $M_n = F_{c1}y_{c1} + F_{t1}y_{t1} + F_{t2}y_{t2}$, and it is expressed as a product of the normalized nominal moment m_n and the cracking moment M_{cr} as follows:

$$M_n = m_n M_{cr} \quad , \quad M_{cr} = \frac{\sigma_{cr} b h^2}{6} \quad (1-7)$$

$$m_n = C_2 \frac{k^2 - 2k + 1}{\beta^2} + \frac{2\beta k^3}{1-k}; \quad \text{where } C_2 = C_1 + 2C_1\beta - \beta^2 \quad (1-8)$$

If the full stress strain response is desired, then the location of neutral axis and moment capacity are obtained under the definitions provided in Table 1.2. In this table the

derivations of all potential combinations for the interaction of tensile and compressive response are presented. Note that depending on the relationship among material parameters, any of the zones 2.1, and 2.2, or 3.1, and 3.2 are potentially possible.

Analysis of these equations indicates that the contribution of fibers is mostly apparent in the post cracking tensile region, where the response continues to increase after cracking [figure 1.2 (a)]. The post-crack modulus E_{cr} is relatively flat with values of $\eta = 0.00-0.4$ for a majority of cement composites. The tensile strain at peak strength ϵ_{peak} is relatively large compared to the cracking tensile strain ϵ_{cr} and may be as high as $\alpha = 100$ for polymeric based fiber systems. These unique characteristics cause the flexural strength to continue to increase after cracking. Since typical strain-hardening material do not have significant post-peak tensile strength, the flexural strength drops after passing the tensile strain at peak strength. Furthermore the effect of post crack tensile response parameter μ can be ignored for a simplified analysis. In the most simplistic way, one needs to determine two parameters in terms of post crack stiffness η , and post crack ultimate strain capacity α , to estimate the maximum moment capacity for the design purposes.

According to bilinear tension and elastic compression models shown in figure 1.2 (a) and (b), the maximum moment capacity is obtained when the normalized tensile strain at the bottom fiber ($\beta = \epsilon_t/\epsilon_{cr}$) reaches the tensile strain at peak strength ($\alpha = \epsilon_{peak}/\epsilon_{cr}$). However, the simplified equations 1-6 to 1-8 for moment capacity are applicable for the compressive stress in elastic region only. The elastic condition must be checked by computing the normalized compressive strain developed at the top fiber λ and compare it

to the normalized yield compressive strain ω . The general solutions for all the cases are presented in table 1.2. Using the strain diagram in Fig. 1.3 (a), the relationship between the top compressive strain and bottom tensile strain as follow:

$$\frac{\varepsilon_c}{kh} = \frac{\varepsilon_t}{(1-k)h} \quad (1-9)$$

By substituting $\varepsilon_c = \lambda\varepsilon_{cr}$ and $\varepsilon_t = \beta\varepsilon_{cr}$ in equation 1-9, then defining the maximum compressive strain to the yield compressive strain $\varepsilon_{cy} = \omega\varepsilon_{cr}$, equation 1-9 is expressed in normalized form:

$$\lambda = \frac{k}{1-k}\beta \leq \omega \quad (1-10)$$

The case represented by case 2.1 of the table 1.2, where the tensile behavior is in elastic-plastic while the compressive behavior is still elastic is studied in this section. Equations for other cases can also be developed. The general solution presented in table 1.1 can be simplified as follows. The location of neutral axis represented as a function of applied tensile strain β is represented as:

$$k = \frac{\sqrt{A}}{\sqrt{A} + \beta\sqrt{\gamma}} \quad A = \eta(\beta^2 + 1 - 2\beta) + 2\beta - 1 \quad (1-11)$$

This equation can be easily simplified by assuming equal tension and compression stiffness ($\gamma=1$). For an elastic perfectly plastic tension material ($\eta=0$) equation 1-11 reduces to:

$$k = \frac{\sqrt{2\beta-1}}{\sqrt{2\beta-1} + \beta} \quad (1-12)$$

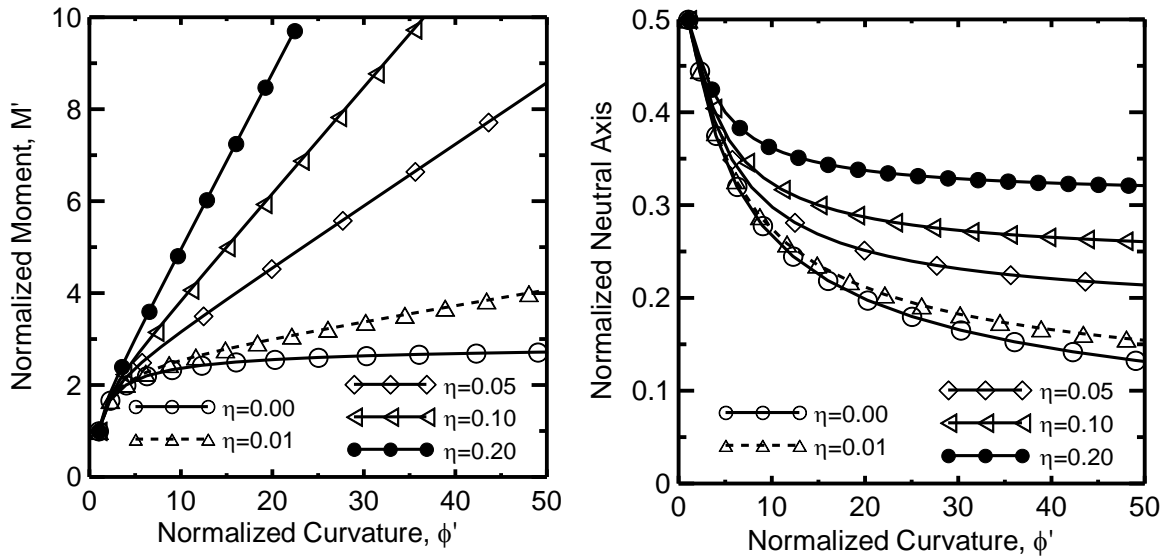


Figure 1.4 Effect of a) Depth of Neutral axis on the moment capacity of a section, and b) the moment curvature response in the Range 2.1

Table 1.1 presents the case of ($\gamma=1$), for different values of post-crack stiffness $\eta = 0.5, 0.2, 0.1, 0.05, 0.01$, and 0.001 . Note that the neutral axis is a function β and can be used in calculation of the moment, or the moment-curvature relationship. These general responses are shown in Figures 1.4a and 1.4b and show that with an increase in applied tensile strain, the neutral axis compression zone decreases; however this decrease is a function of post crack tensile stiffness factor. The moment curvature relationship in this range in ascending, however, its rate is a function of the post crack tensile stiffness. The parameter based fit equations in the third and fourth column are obtained by curve fitting the simulated response from the closed form derivations and are applicable within 1% accuracy of the closed form results. Using these equations, one can generate the moment

capacity and moment-curvature response for any cross section using basic tensile material parameters in the 2.1 range as defined.

| η | $A, (k = \frac{\sqrt{A}}{\sqrt{A + \beta}})$ | $M'(k)$ | $M'(\varphi)$ |
|--------|--|--|--------------------------------|
| 0.5 | $0.5(\beta^2 + 1 - 2\beta) + 2\beta - 1$ | $-0.773 + 0.108 \times 10^{-1} k^{-6}$ | $0.507 + 0.686\varphi$ |
| 0.2 | $0.2(\beta^2 + 1 - 2\beta) + 2\beta - 1$ | $0.654 + 0.516 \times 10^{-2} k^{-6}$ | $1.105 + 0.383\varphi$ |
| 0.1 | $0.1(\beta^2 + 1 - 2\beta) + 2\beta - 1$ | $1.276 + 0.289 \times 10^{-2} k^{-6}$ | $1.461 + .234\varphi$ |
| 0.05 | $0.05(\beta^2 + 1 - 2\beta) + 2\beta - 1$ | $1.645 + .1632 \times 10^{-2} k^{-6}$ | $1.720 + .1401\varphi$ |
| 0.01 | $0.01(\beta^2 + 1 - 2\beta) + 2\beta - 1$ | $0.852 + 0.456 k^{-1}$ | $1.342 + 0.371\sqrt{\varphi}$ |
| 0.0001 | $0.0001(\beta^2 + 1 - 2\beta) + 2\beta - 1$ | $3.177 - 3.068 k$ | $3.021 - 2.047/\sqrt{\varphi}$ |

Table 1-1: Location of Neutral axis, moment, and moment-curvature response of a strain hardening composite material with $\gamma = 1$, $\eta = 0.0001 - 0.5$.

| Stage | k | m = M/M _{cr} | ϕ = Φ/ Φ _{cr} |
|---|---|--|--|
| 1 0 < β ≤ 1 | $k_1 = \begin{cases} \frac{1}{2} & \text{for } \gamma=1 \\ \frac{-1+\sqrt{\gamma}}{-1+\gamma} & \text{for } \gamma \neq 1 \end{cases}$ | $m_1 = \frac{2\beta \left[(\gamma-1)k_1^3 + 3k_1^2 - 3k_1 + 1 \right]}{1-k_1}$ | $\phi'_1 = \frac{\beta}{2(1-k_1)}$ |
| 2.1 1 < β ≤ α 0 < λ ≤ ω | $k_{21} = \frac{D_{21} - \sqrt{D_{21}\gamma\beta^2}}{D_{21} - \gamma\beta^2}$ $D_{21} = \eta(\beta^2 - 2\beta + 1) + 2\beta - 1$ | $M'_{21} = \frac{(2\gamma\beta^3 - C_{21})k_{21}^3 + 3C_{21}k_{21}^2 - 3C_{21}k_{21} + C_{21}}{1-k_{21}}$ $C_{21} = \frac{(2\beta^3 - 3\beta^2 + 1)\eta + 3\beta^2 - 1}{\beta^2}$ | $\phi'_{21} = \frac{\beta}{2(1-k_{21})}$ |
| 2.2 1 < β ≤ α ω < λ ≤ λ _{cu} | $k_{22} = \frac{D_{22}}{D_{22} + 2\omega\gamma\beta}$ $D_{22} = D_{21} + \gamma\omega^2$ | $M'_{22} = (3\gamma\omega\beta^2 + C_{22})k_{22}^2 - 2C_{22}k_{22} + C_{22}$ $C_{22} = C_{21} - \frac{\gamma\omega^3}{\beta^2}$ | $\phi'_{22} = \frac{\beta}{2(1-k_{22})}$ |
| 3.1 α < β ≤ β _{tu} 0 < λ ≤ ω | $k_{31} = \frac{D_{31} - \sqrt{D_{31}\gamma\beta^2}}{D_{31} - \gamma\beta^2}$ $D_{31} = \eta(\alpha^2 - 2\alpha + 1) + 2\mu(\beta - \alpha) + 2\alpha - 1$ | $M'_{31} = \frac{(2\gamma\beta^3 - C_{31})k_{31}^3 + 3C_{31}k_{31}^2 - 3C_{31}k_{31} + C_{31}}{1-k_{31}}$ $C_{31} = \frac{(2\alpha^3 - 3\alpha^2 + 1)\eta - 3\mu(\alpha^2 - \beta^2) + 3\alpha^2 - 1}{\beta^2}$ | $\phi'_{31} = \frac{\beta}{2(1-k_{31})}$ |
| 3.2 α < β ≤ β _{tu} ω < λ ≤ λ _{cu} | $k_{32} = \frac{D_{32}}{D_{32} + 2\omega\gamma\beta}$ $D_{32} = D_{31} + \gamma\omega^2$ | $M'_{32} = (3\gamma\omega\beta^2 + C_{32})k_{32}^2 - 2C_{32}k_{32} + C_{32}$ $C_{32} = C_{31} - \frac{\gamma\omega^3}{\beta^2}$ | $\phi'_{32} = \frac{\beta}{2(1-k_{32})}$ |

Table 1-2 : Neutral axis parameter k , normalized moment m and normalized curvature ϕ for each stage of normalized tensile strain at bottom fiber (β)

1.3 Production Techniques

Strain hardening cement paste composites were prepared by pultrusion [9]. In the pultrusion process as shown in Figure 1.6 the fabrics were passed through a slurry infiltration chamber, and then pulled through a set of rollers to squeeze the paste in between the fabric openings while removing excessive paste. Gear motors were attached on both the rollers and were made to operate at the same rpm in opposite directions so that the infiltrated fabric can easily be passed through the rollers. This technique for the production of fabric-cement products requires relatively simple set-up using low cost equipment while allowing good control of the laminates alignment giving relatively smooth surface and uniform products. Through previous research done [10] it has been found that pultrusion process significantly improves the mechanical performance of the cement composites as it enables the spaces between the filaments of the bundle to be impregnated with the paste, resulting in a much better bond and maximized efficiency of the filaments, which leads to improved properties.

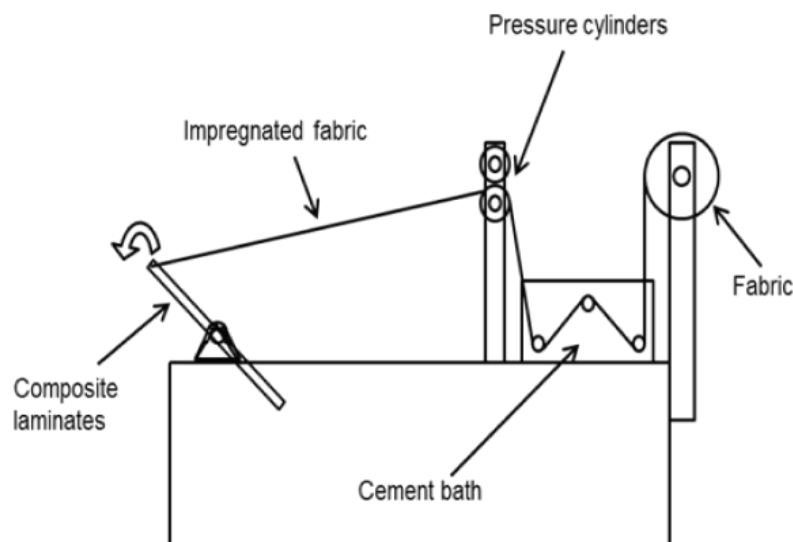


Figure 1.5 Schematics of pultrusion process



Figure 1.6 Pultrusion setup with motors attached to the rollers

Pultruded samples were very thin and not feasible for testing. Therefore, after the fabrics were passed through the rollers, additional cement paste was applied on each surface using the traditional hand lay-up technique. This was done to improve the thickness of the final composite and make it more workable. Consistent amount of cement paste (by weight) was added on each layer depending on the final thickness required. For the samples with final thickness of 5 mm, 350 grams of cement paste was added on each layer and for 6.5 mm thick samples, 450 grams of cement paste was applied on each layer. After forming the samples, pressure was applied on top of the fabric-cement laminates to improve penetration of the matrix in between the opening of the fabrics. A constant pressure of 13.95 kPa due to a 900 N load was applied on the surface of the fabric cement sheet of all specimens. Samples were then left for drying for 24 hours before de-molding them and placing them in curing room for next 6 days.



Figure 1.7 Hand lay-up

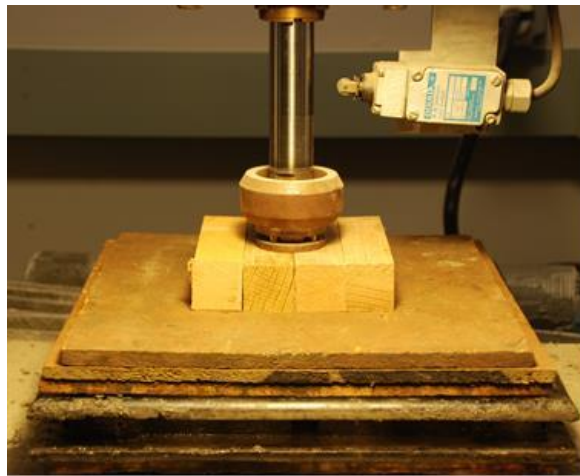


Figure 1.8 Hydraulic press

To minimize the marginal restriction due to the joints of the fixture, four corners of sample were cut into the desired shape by band saw and table saw. The size of the sample was smaller than clamped in the picture frame. The final shape of the samples was cut to meet the two main requirements. Firstly, there should not be any sharp edges. Sharp edges would cause stress concentration. Secondly, edges should be long enough so that all the three bolts could be passed through the sample. Clamping using three bolts minimized the slipping and twisting caused during the test.

2. CHAPTER 2 - LIMIT STATE ANALYSIS OF STRAIN HARDENING STRUCTURAL PANELS

An application of the use strain hardening cement composites for design of panels is discussed in this chapter. Strain hardening cement composites (SHCC) exhibits strain hardening, quasi-ductile behavior due to the bridging of fine multiple cracks by fibers or textiles as primary reinforcement. Fibers have been used as reinforcement in many applications such as heavily reinforced sections, shear critical regions, slabs-on-grade and pavements. The use of fibers in concrete slabs or flat plates supported on piles or columns is becoming popular due to practicality of installation, enhanced control of shrinkage cracks, durability, toughness, and cost savings in labor and equipment.

A key advantage is the reduction in construction time compared to the traditional installation of double layers of conventional reinforcing bars, stirrups, or other shear reinforcement. SHCC material slabs resist high moment intensities as well as high shear and punching shear stresses. Because the fiber-reinforced concrete can be directly pumped, the use of cranes for lifting reinforcing bars is eliminated. The total cost saving in construction can be as high as 30 percent compared with traditional methods of reinforced concrete slab construction. Another advantage of using SHCC materials in slabs is to reduce the number of joints.

The analytical strength of the slabs calculated by means of standard rectangular stress block calculations tend to underestimate the experimental results. This suggests that the failure mechanisms may be governed by yield-line theory. In this chapter a methodology to derive the load deflection response for a SHCC slab has been demonstrated. Moment

curvature response which is a material property has been extended to calculate the load deflection response of a strain hardening panel with known geometry and end conditions by integrating the three aspects of curvature-deflection relationship with applied load-yield line moment into the moment curvature relationship as shown in figure 2.1.

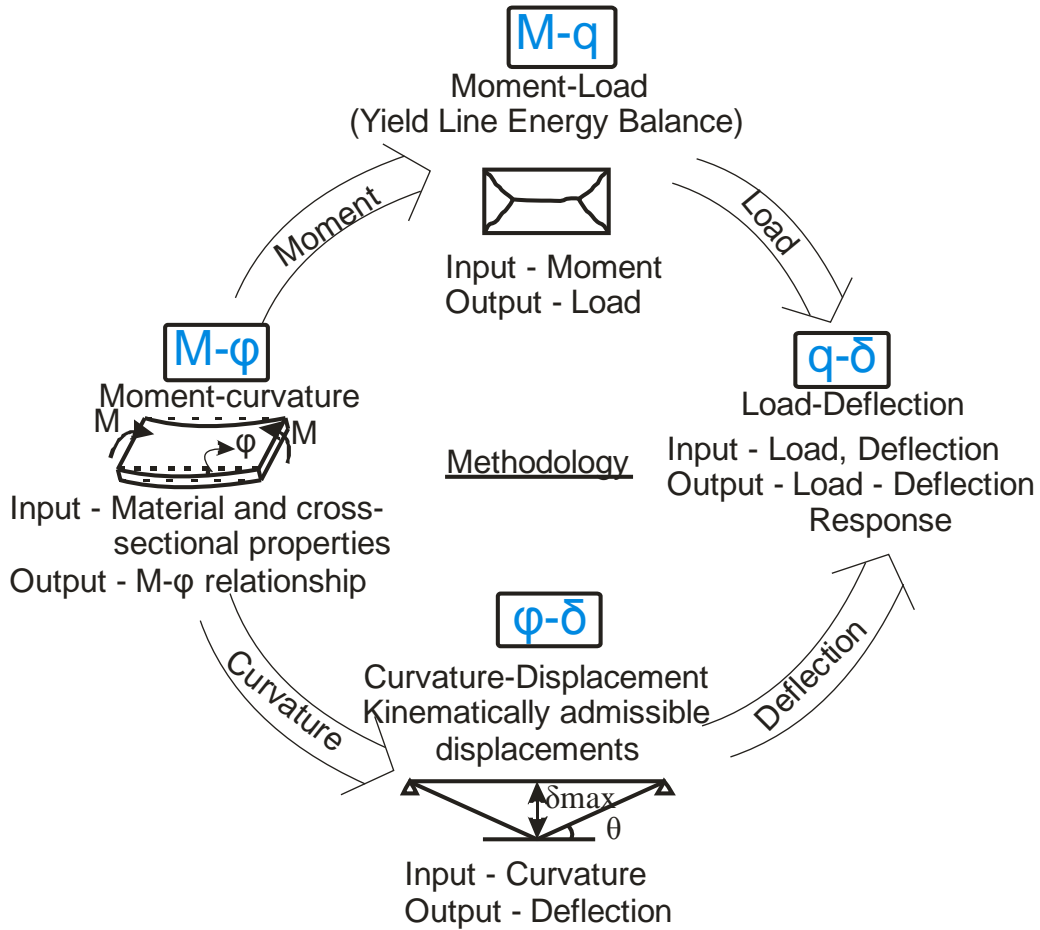


Figure 2.1 Process for applied load-deflection derivation



Figure 2.2 Construction and applications of SHCC material slabs [11]

2.1 Yield Line Analysis Approach

Yield line design is a well-founded method of designing reinforced concrete slabs, and similar types of elements. It uses yield line theory to investigate failure mechanisms at the ultimate limit state. The theory is based on the principle that work done in rotating yield lines is equal to work done in moving the loads [12][13]. When applying the Work Method for yield line analysis the calculations for the external work due to loads and the internal work due to dissipation of energy within the yield lines are carried out independently. The results are then made equal to each other and from the resulting equations the unknown, be it the ultimate moment 'm' generated in the yield lines or the ultimate failure distributed load 'q' of the slab is evaluated.

The slab is divided into rigid regions that rotate about their respective axes of rotation along the support lines. If the point of maximum deflection is given a value of unity then the vertical displacement of any point in the regions is thereby defined. The work done

due to external loads is evaluated by taking all external loads on each region, finding the center of gravity of each resultant load and multiplying it by the distance it travels.

The work done due to dissipation of energy is quantified by projecting all the yield lines around a region onto, and at right angles to, that region's axis of rotation. These projected lengths are multiplied by the moment acting on each length and by the angle of rotation of the region. At the small angles considered, the angle of rotation is equated to the tangent of the angle produced by the deflection of the region.

2.2 2-D Analysis of Panels for Moment-Load Relationship

Work method has been used to calculate the moment-load relationship for all the basic configurations of slabs namely square, rectangle and circular with all possible support conditions. It has been assumed that moment about each point on yield line is consistent and sagging moment is equal to hogging moment. Yield line formation in square and rectangular slabs has been assumed to be at 45° to the edges for simplification. General cases for yield lines not at 45° are also calculated. Load deflection results have been found out for square and rectangle slabs having uniformly distributed load of magnitude q and round slabs having a point load acting at center with a magnitude of P . Support conditions considered include (a) simply supported at the four vertexes in cases of square and rectangular panels and (b) clamped along the edges.

2.2.1 Case 1 – Applied Load vs. Yield Line Moment Relationship for Square Slabs

Square slab of edge length L is considered here with a distributed load of ' q ' acting on it. It is assumed that yield lines are at 45° to the sides and each point on the yield line is

consistent and under tension. Hogging moment about the yield lines and sagging moment about the clamped supports are also assumed to be equal in magnitude. Three end conditions can be considered which are –

- i) All sides are simply supported (Case 1.1)
- ii) All sides have clamped supports (Case 1.2)
- iii) Mixed boundary conditions with two adjacent sides simply supported whereas other two have clamped supports (Case 1.3)

Case 1.1 – Square Panel with Simply Supported Edges

Plastic analysis approach uses the principal of virtual work to equate the internal and external work to obtain the collapse load. Similarly the yield pattern is used to define the potential collapse mechanism of a plate supported along its two or four edges. If the panel has fixed edges, then the yielding along the edge is also needed to be included in the calculations.

From the relationship of equating the external work done by loads moving to the internal energy dissipated by rotations about yield line, one gets:

$$W_{\text{ext}} = W_{\text{int}} \quad (2-1)$$

$$\Sigma(N \delta) = \Sigma(m l \theta) \quad (2-2)$$

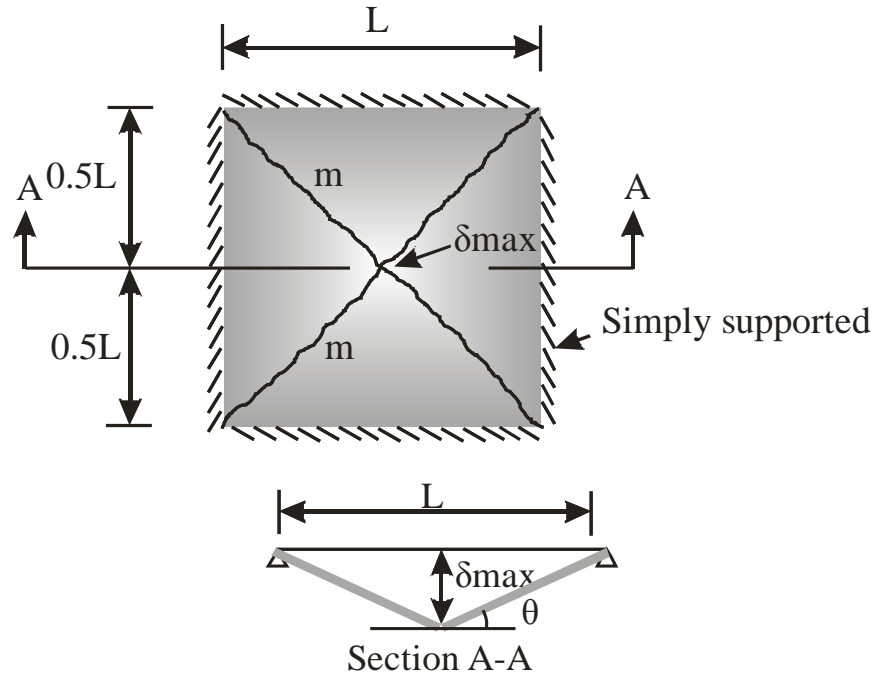


Figure 2.3 Simply supported square Panel with (a) yield lines and (b) loading and rotation conditions through section A-A.

In left hand side, q is the uniformly distributed load and $L^2/4$ is the area of each wedge (So the equivalent point load is $q \times L^2/4$) and $\delta_{max}/3$ is the deflection of the centroid. On the right hand side, L is the length of the square as the rotations are projected onto the sides. Rotation angle, θ , can be calculated from geometry shown in figure 2.3(b) as $\delta_{max}/0.5L$.

$$4 \left(q \frac{L^2}{4} \frac{\delta_{max}}{3} \right) = 4 \left(m L \frac{\delta_{max}}{0.5L} \right) \quad (2-3)$$

Simplifying equation 2-3 and solving for moment, one gets-

$$\frac{4L^2 q}{12} = 8m \quad , \quad m = \frac{qL^2}{24} \quad (2-4)$$

Where m is the moment along the yield lines, q is the uniformly distributed load and L is the length of the square side.

Case Study 1.2 – Square Panel with Edges clamped

External work due to energy expended is independent of the support conditions therefore it is the same as the expression obtained for simply supported slab. Internal work due to energy dissipation in case of clamped slabs will be higher due to rotation of the corner supports. All the four wedges have projection of their positive (sagging) yield line of a value m surrounding that region onto its axis of rotation with length as L . Sides also have continuous supports (clamped) and negative (hogging) yield line causing moment of value m' , that forms along the support.

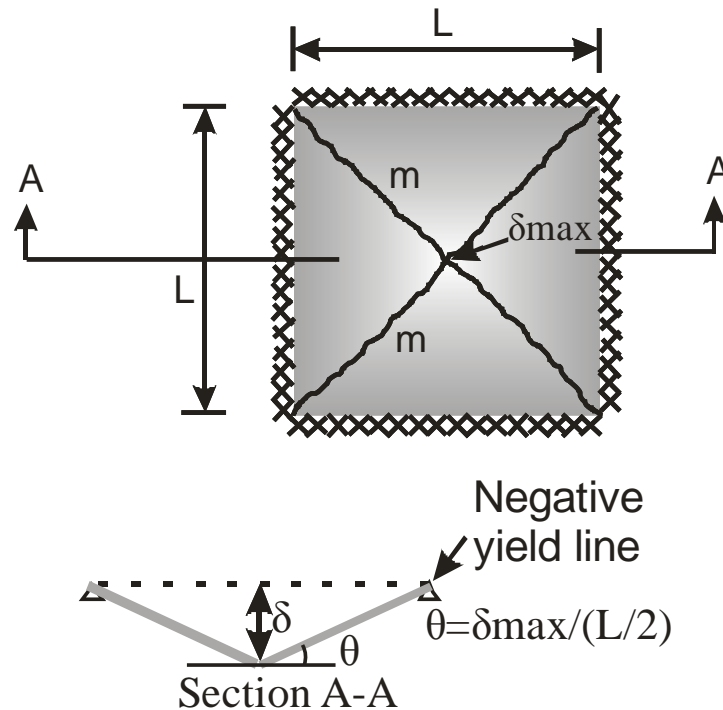


Figure 2.4 Applied load and yield line moment for a clamped square slab.

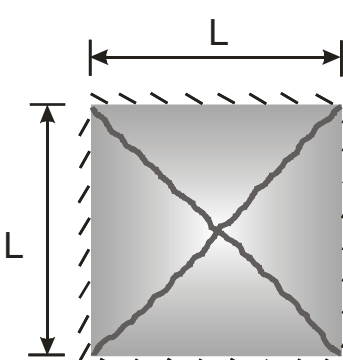
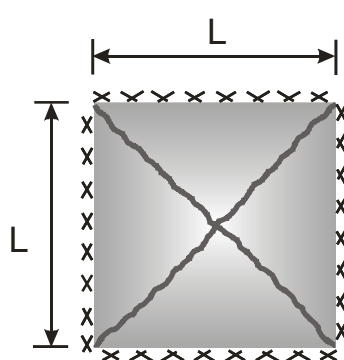
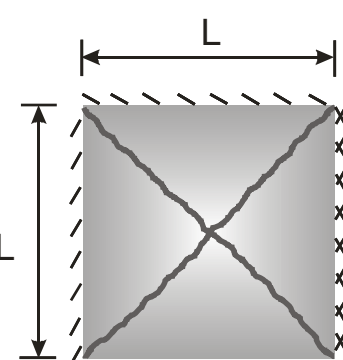
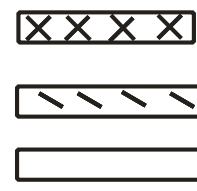
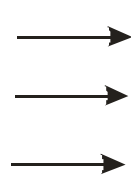
$$\begin{aligned}
 W_{\text{ext}} &= W_{\text{int}} \\
 \Sigma(N \delta) &= \Sigma(m l \theta) \tag{2-5} \\
 4 \left(q \frac{L^2}{4} \frac{\delta_{\text{max}}}{3} \right) &= 4 \left(m L \frac{\delta_{\text{max}}}{0.5L} + m' L \frac{\delta_{\text{max}}}{0.5L} \right)
 \end{aligned}$$

If one assumes $m=m'$ (that is the sagging is equal to the hogging moment), one gets:

$$\frac{4L^2 q}{12} = 16m \quad , \quad m = \frac{qL^2}{48} \tag{2-6}$$

Case 1.3 for mixed boundary condition can be derived similarly. Results for yield line moment relationship with applied load for square slabs for various end conditions in summarized in table 2-1.

Table 2-1 : Applied load – yield line moment relationship for Cases 1.1 to 1.3

| Case 1.1 | Case 1.2 | Case 1.3 | | | | | | | | |
|---|---|---|--------|----------|---|---|---|---|---|---|
|  |  |  | | | | | | | | |
| $m = \frac{qL^2}{24}$ | $m = \frac{qL^2}{48}$ | $m = \frac{qL^2}{36}$ | | | | | | | | |
| Where, | | | | | | | | | | |
|  |  | Clamped support Simply supported Free support | | | | | | | | |
| | | <table style="margin-left: auto; margin-right: auto;"> <thead> <tr> <th style="text-align: left;">Moment</th> <th style="text-align: left;">Rotation</th> </tr> </thead> <tbody> <tr> <td style="text-align: center;">✓</td> <td style="text-align: center;">✗</td> </tr> <tr> <td style="text-align: center;">✗</td> <td style="text-align: center;">✓</td> </tr> <tr> <td style="text-align: center;">✗</td> <td style="text-align: center;">✓</td> </tr> </tbody> </table> | Moment | Rotation | ✓ | ✗ | ✗ | ✓ | ✗ | ✓ |
| Moment | Rotation | | | | | | | | | |
| ✓ | ✗ | | | | | | | | | |
| ✗ | ✓ | | | | | | | | | |
| ✗ | ✓ | | | | | | | | | |

2.2.2 Case 2- Applied Load vs. Yield Line Moment Relationship for Rectangular Slabs

Rectangular slab of length 'a' and breadth 'b' has been considered here and a uniformly distributed load 'q' is acting on it. It is assumed that yield lines are at 45° to the sides and each point on the yield line is consistent and under tension. Hogging moment at yield line and sagging moment about the edges are also assumed to be equal in magnitude. Five end conditions can be considered and their results are summarized in table 2-2.

- i) Clamped support about one side and simply supported about other three (Case 2.1)
- ii) Clamped support about two adjacent sides and simply supported about other two adjacent sides (Case 2.2)
- iii) Clamped support about three sides and simply supported about one side (Case 2.3)
- iv) All 4 sides have same support conditions (Case 2.4)
- v) Fixed on three sides and free about one side (Case 2.5)

Derivation for two adjacent edges as clamped and remaining two as simply supported is presented first. Cases 2.1, 2.3 and 2.4 can be derived similarly.

Case Study 2.2 – Rectangular Slab with two adjacent edges clamped and other two as simply supported

The slab is divided into rigid regions that rotate about their respective axes of rotation along the support lines. If the point of maximum deflection is given a value of unity then the vertical displacement of any point in the regions is thereby defined.

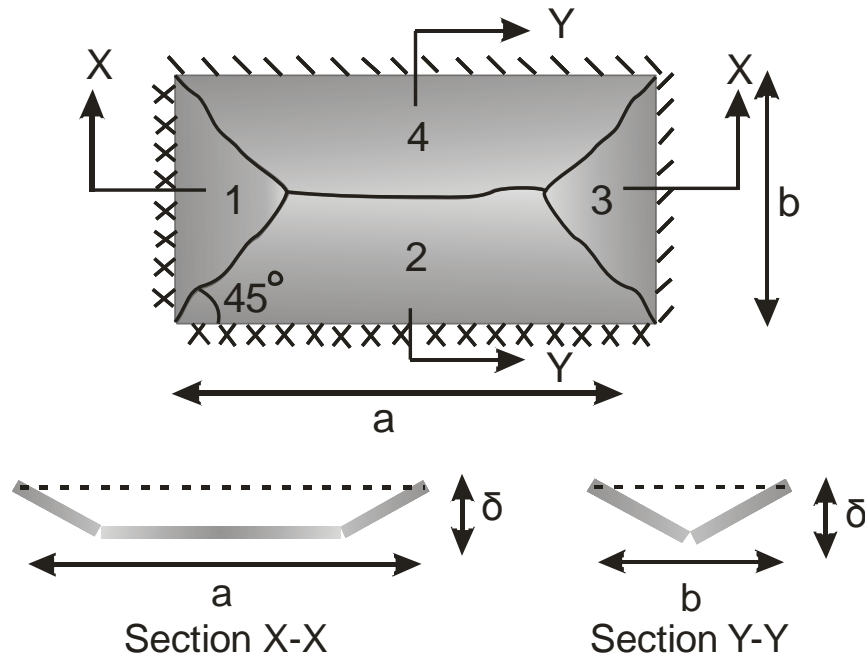


Figure 2.5 Two sides clamped and other two sides simply supported rectangular slab

The expenditure of external loads is evaluated by taking all external loads on each region, finding the center of gravity of each resultant load and multiplying it by the distance it travels. Two groups are considered the triangles and the trapezoidal sections:

$$W_{ext} = \sum(N \delta) = \left(\frac{1}{3} q b^2 \right) + \left(\frac{1}{2} q (a-b)b \right) = \frac{qb}{6} (3a-b) \quad (2-7)$$

In the above expression, the first half of the expression consists of both the triangles (regions 1 and 3 completely and parts of region 2 and 4). Their area is b^2 and therefore equivalent point load is expressed as qb^2 and $1/3$ is the deflection of the centroid when maximum deflection has been assumed as unity. Second half of the expression is composed of the rectangle at the center which consists of the remaining regions of two and four.

The internal work done due to dissipation of energy is quantified by projecting all the yield lines around a region onto, and at right angles to, that region's axis of rotation. These projected lengths are multiplied by the moment acting on each length and by the angle of rotation of the region. At the small angles considered, the angle of rotation is equated to the tangent of the angle produced by the deflection of the region. Assuming the moment caused due to the rotation of yield lines as m (positive/sagging) and moment caused due to the rotation about the clamped sides as m' (negative/hogging).

$$W_{\text{int}} = \sum (m l \theta) = \left(mb \frac{2}{b} \right) + \left(m' b \frac{2}{b} \right) + \left(ma \frac{2}{b} \right) + \left(m' a \frac{2}{b} \right) + m b \frac{2}{b} + ma \frac{2}{b} \quad (2-8)$$

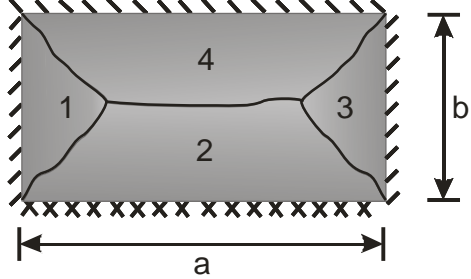
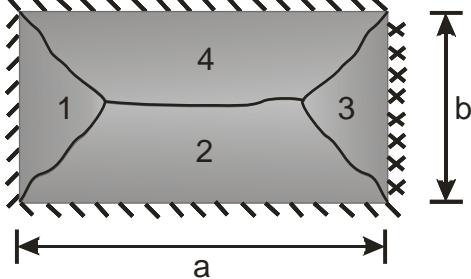
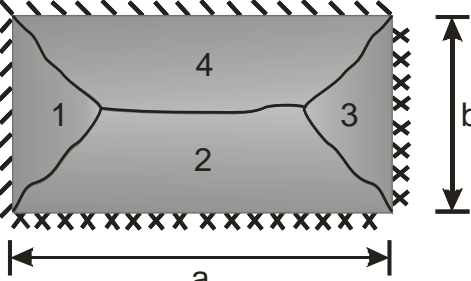
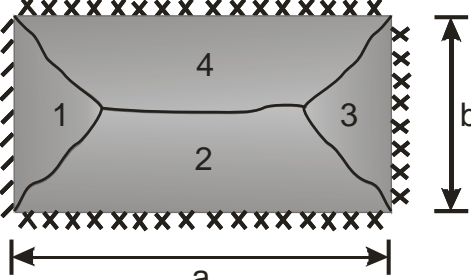
Term 1 and 3 represent the triangular portion, terms 2 and 4 represent the negative moments in the triangular portions, and terms 5 and 6 represent the Trapezoidal sections contributions. Assuming the moment acting about the yield line and the moment acting about the supports equal to each other, that is the positive and negative moments are

equal ($m = m'$), one gets -
$$W_{\text{int}} = 6m \left(1 + \frac{a}{b} \right)$$

Energy equilibrium requires: $W_{\text{ext}} = W_{\text{int}}$, from which one gets-

$$m = \frac{qb^2(3a-b)}{36(a+b)} \quad (2-9)$$

Table 2-2 : Applied load – yield line moment relationship for Cases 2.1 to 2.4

| Case # | Boundary Conditions | | Failure Modes | Yield line Moment – Applied load |
|--------|--|---------------------------------|--|------------------------------------|
| 2.1 | Clamped about one side and simply supported about other 3 | Clamped about long side |  | $m = \frac{qb^2(3a-b)}{12(3a+2b)}$ |
| | | Clamped about short side |  | $m = \frac{qb^2(3a-b)}{12(2a+3b)}$ |
| 2.2 | Clamped about two adjacent sides and simply supported about other two adjacent sides | |  | $m = \frac{qb^2(3a-b)}{12(3a+3b)}$ |
| 2.3 | Clamped about three sides and simply supported about one side | Simple support about short side |  | $m = \frac{qb^2(3a-b)}{12(4a+3b)}$ |

| | | | | | |
|--------|--|--------------------------------|--------------------|------------------------------------|----------|
| | | Simple support about long side | | $m = \frac{qb^2(3a-b)}{12(3a+4b)}$ | |
| 2.4 | All 4 sides have same support conditions | All supports clamped | | $m = \frac{qb^2(3a-b)}{12(4a+4b)}$ | |
| | | All simply supported | | $m = \frac{qb^2(3a-b)}{12(2a+2b)}$ | |
| Where, | | | | | |
| | | | → Clamped support | Moment | Rotation |
| | | | → Simply supported | ✓ | ✗ |
| | | | → Free support | ✗ | ✓ |

Case Study 2.5 – Fixed on three sides and free on fourth side

This case study addresses a slab with a free edge which is different than the previous cases. The number and pattern of yield lines are changed to accommodate the free deformation of the unsupported edge.

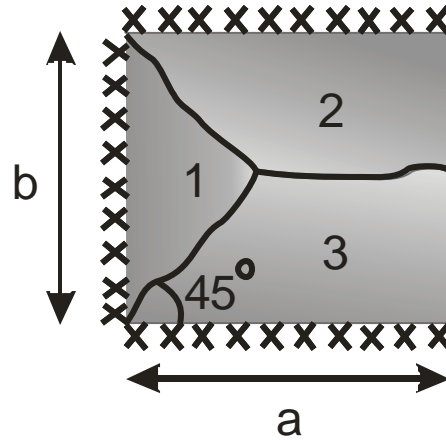


Figure 2.6 Applied load and yield line moment for a rectangular slab clamped on three sides and free on fourth

$$W_{\text{int}} = \sum (m l \theta) = \left(mb \frac{2}{b} \right) + \left(m' b \frac{2}{b} \right) + \left(ma \frac{2}{b} \right) + \left(m' a \frac{2}{b} \right) \quad (2-10)$$

Term 1 represent the triangular portion, term 2 represent the negative moments in the triangular portions, and terms 3 and 5 represent the trapezoidal sections contributions. Assuming the moment acting about the yield line and the moment acting about the supports equal to each other, that is the positive and negative moments are equal ($m = m'$), we get -

$$W_{\text{int}} = 4m \left[1 + \frac{a}{b} \right] \quad (2-11)$$

$$W_{ext} = \sum(N \delta) = \left(\frac{1}{6} q b^2\right) + \left(\frac{1}{2} q \left(a - \frac{b}{2}\right) b\right) = \frac{qb}{2} \left(a - \frac{b}{6}\right) \quad (2-12)$$

In the above expression, the first half of the expression consists of both the triangles (region 1 and parts of region 2 and 3). Their area is $0.5b^2$ and therefore equivalent point load is expressed as $0.5qb^2$ and $1/3$ is the deflection of the centroid when maximum deflection has been assumed as unity. Second half of the expression is composed of the rectangle which consists of the remaining regions of 2 and 3. Energy equilibrium requires: $W_{ext} = W_{int}$, we get-

$$m = \frac{qb^2(6a - b)}{48(a + b)} \quad (2-13)$$

2.2.3 Case 3 - Applied Load vs. Yield Line Moment for Round Panels

Round panels of radius R is considered here with a point load of 'P' acting at the center on it. Yield lines form a fan shaped design and it is considered that each point on the yield line is consistent and under tension. Hogging moment along the yields lines and sagging moment along the supports are also assumed to be equal in magnitude. Two end conditions can be considered which are –

- i) It is simply supported (Case 3.1)
- ii) It has clamped support (Case 3.2)

In figure 2.7 if one defines number of cracks as n, then the central angle α can be calculated as $2\pi/n$. It has been assumed here that when number of cracks, n tends to infinity, the angle α becomes zero. In case of a simply supported three point ring specimens, n is taken as 3. Flexural capacity of round slab simply supported (Case 3.1)

subjected to a center-point loading is shown in figure 2-7. Note that depending on the number of yield lines, the internal energy dissipation changes.

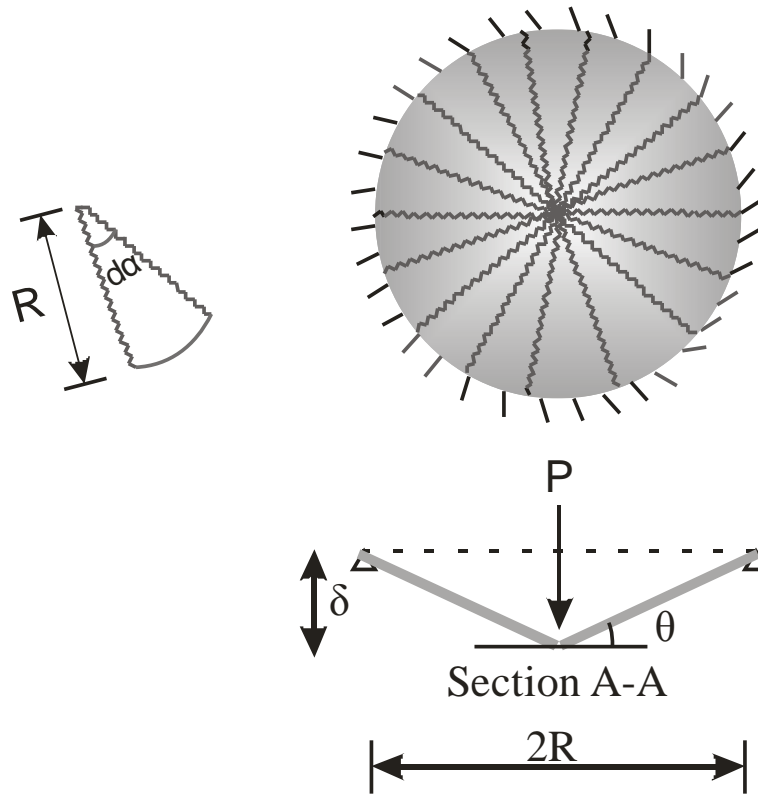


Figure 2.7 Principle of virtual work to determine the ultimate load carrying capacity of a round panel test simply supported in its contour and subjected to center point load

It is however shown that in the case of simply supported round slab, the allowable applied load can be related to the bending moment capacity which is determined through laboratory tests on flexural samples [22].

$$W_{int} = W_{ext} \quad ; \theta = \frac{\delta}{R}$$

$$dW_{int} = MR\theta d\alpha = M\delta d\alpha$$

$$W_{ext} = P\delta$$

$$W_{int} = W_{ext} = \int_0^{2\pi} M\delta d\alpha = 2\pi M\delta = P\delta$$

$$M = \frac{P}{2\pi} \quad (2-14)$$

If the support is fixed (Case 3.2), the solution would yield:

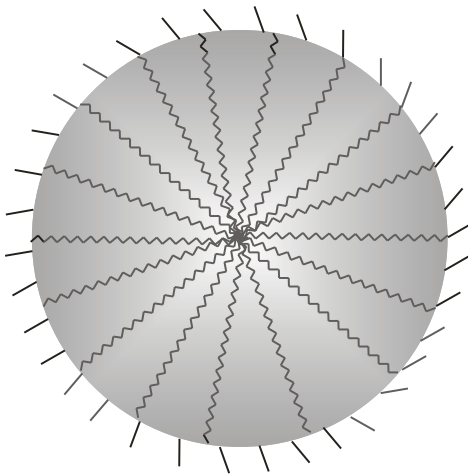
$$W_{int} = W_{ext}$$

$$\int_0^{2\pi} M\delta d\alpha + 2\pi RM\theta = 4\pi M\delta = P\delta \quad (2-15)$$

$$M = \frac{P}{4\pi} \quad (2-16)$$

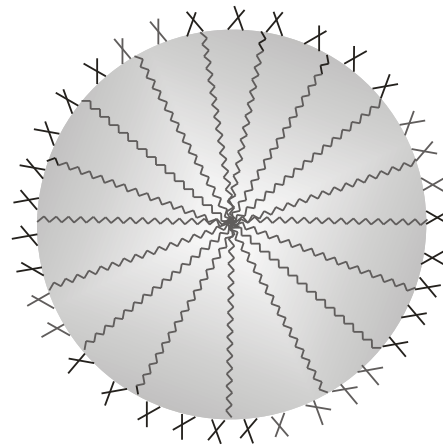
Table 2-3 : Applied load – yield line moment relationship for Cases 3.1 and 3.2

Case 3.1






$$m = \frac{P}{2\pi}$$

Case 3.2



$$m = \frac{P}{4\pi}$$

Where,

| | | | Moment | Rotation |
|---|---|------------------|--------|----------|
|  | → | Clamped support | ✓ | ✗ |
|  | → | Simply supported | ✗ | ✓ |
|  | → | Free support | ✗ | ✓ |

2.3 Analysis of Panels for Curvature-Deflection Relationship

Rotations that a slab undergoes at supports for certain deflections were calculated using the concepts of kinematics and geometry of slab. This rotation-deflection relationship was then further extended to give the curvature-deflection relationship by dividing rotation by hinge length, L^* to give the curvature. Details for hinge length are shown in section 2.3.1. All the case studies undertaken in section 2.2 are taken here as well. It can be seen that curvature-deflection relation is independent of end conditions. Yield line formation in square and rectangular slabs has been assumed to be at 45° to the edges same as what was considered for the derivation of load-moment relationship.

2.3.1 Hinge Length, L^*

A slab under bending can be considered to consist of two distinct regions: the small hinge region where concrete crushing is visible, where wide flexural cracks occur, and where most of the permanent rotation is concentrated around the wide flexural cracks so that the trend of the moment distribution has little effect; and the non-hinge region which applies to most of the length so that it is affected by the trend of the moment distribution, where

there are much narrower cracks, where, in particular, concrete crushing does not occur and where standard procedures of equilibrium can be applied [14][15].

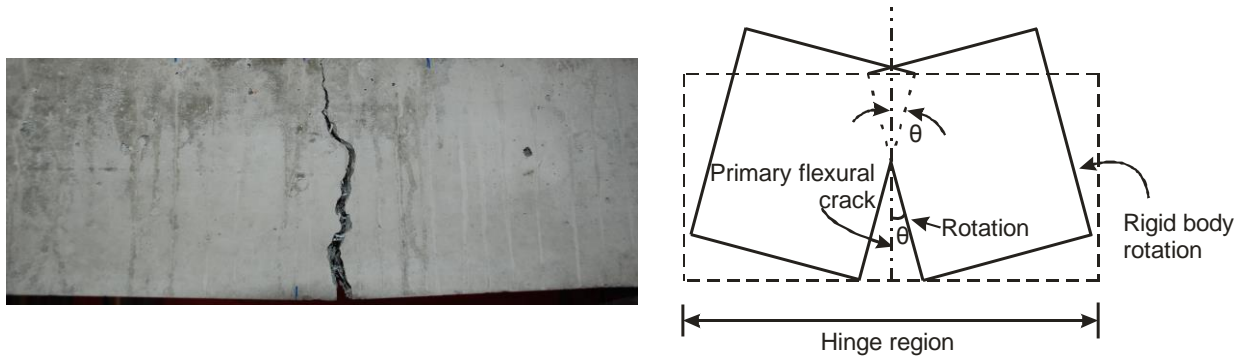


Figure 2.8 Hinge rotation mechanism (a) Steel fiber reinforced beam (BASF), (b) Rigid body hinge rotation [16]

Hinge length has been derived to be a function of span, depth or reinforcement [16]. Curvature is a measure of sectional ductility and rotation is a measure of member ductility. Product of sectional ductility (curvature) and hinge length gives the member ductility (rotation).

Many researchers have concentrated mainly on quantifying the hinge length, L^* empirically. Some suggested approaches are as shown in table below [16]:

Table 2-4 : Empirically derived hinge lengths

| Researcher reference | Hinge length (L^*) | Hinge length variables |
|----------------------|-------------------------|-----------------------------|
| Baker [17] | $k(z/d)^{1.4}d$ | Span (z), depth (d) |
| Sawyer [18] | $0.25d+0.075z$ | Span, depth |
| Corley [19] | $0.5d+0.2(z/d)\sqrt{d}$ | Span, depth |
| Mattock [20] | $0.5d+0.05z$ | Span, depth |

2.3.2 Curvature-Deflection Relationship for a Square Slab

Let us assume a square slab with side L for which yield lines are at 45° to the sides and meet at center and maximum deflection, δ also occurs at center.

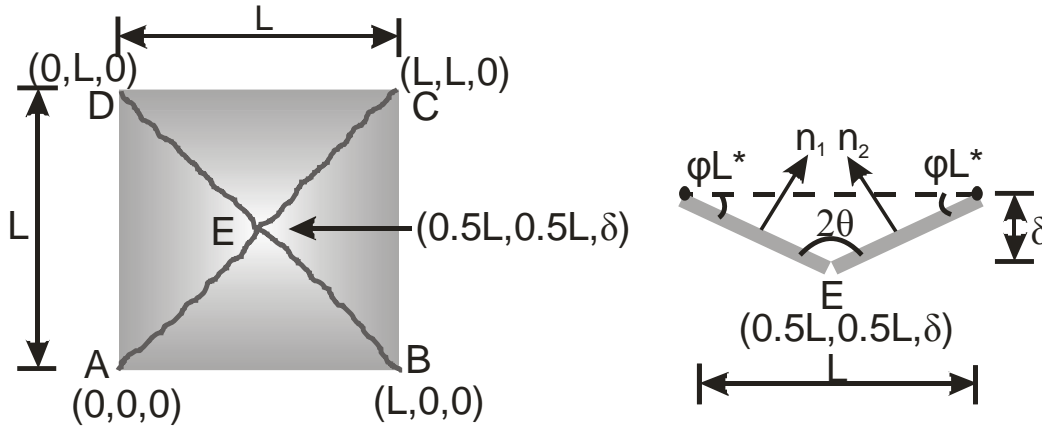


Figure 2.9 Load-deflection relationship for Square slab

To find the angle of rotation, we first find the angle at center between two surfaces.

Curvature, ϕ and angle between the planes, 2θ can then be related as $\phi = \frac{1}{L^*} \left[\frac{\pi}{2} - \theta \right]$

where L^* is the hinge length and ϕL^* is the rotation. For finding the angles between both surfaces we find the angle that the normal to these surfaces make with each other.

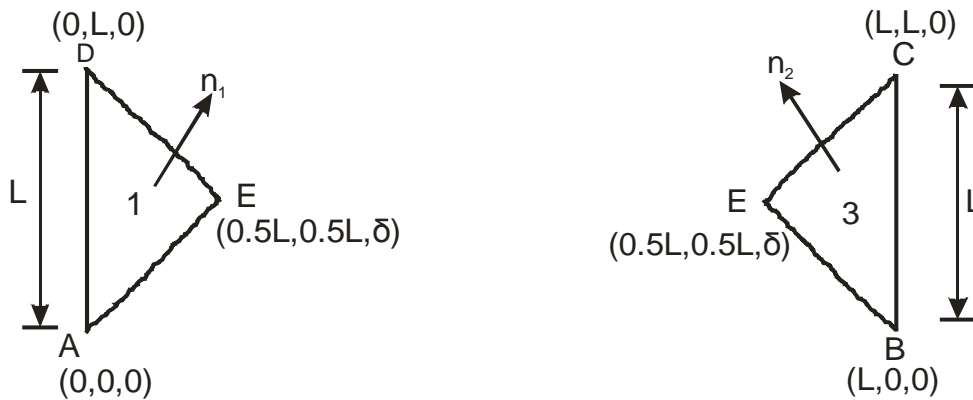


Figure 2.10 Planes AED and EBC

For plane # 1 (AED), the normal n_1 is the cross product of vectors \overline{AE} and \overline{AD} .

$$\overline{AE} = (0.5L, 0.5L, \delta)$$

$$\overline{AD} = (0, L, 0)$$

$$\vec{n}_1 = \overline{AE} \times \overline{AD} = \begin{vmatrix} \hat{i} & \hat{j} & \hat{k} \\ 0.5L & 0.5L & \delta \\ 0 & L & 0 \end{vmatrix} = (-L\delta)\hat{i} + 0.5L^2\hat{k}$$

Equation of the plane # 1 is given as

$$\begin{aligned} -L\delta(x-0) + 0(y-0) + 0.5L^2(z-0) &= 0 \\ (L\delta)x - 0.5L^2z &= 0 \end{aligned} \quad (2-17)$$

For plane # 3 (BCE), the normal n_2 is the cross product of vectors \overline{BE} and \overline{BC} .

$$\overline{BE} = (-0.5L, 0.5L, \delta)$$

$$\overline{BC} = (0, -L, 0)$$

$$\vec{n}_2 = \overline{BE} \times \overline{BC} = \begin{vmatrix} \hat{i} & \hat{j} & \hat{k} \\ -0.5L & 0.5L & \delta \\ 0 & -L & 0 \end{vmatrix} = (-L\delta)\hat{i} - 0.5L^2\hat{k}$$

Equation of the plane # 3 is given as

$$\begin{aligned} -L\delta(x-L) + 0(y-0) - 0.5L^2(z-0) &= 0 \\ (L\delta)x + 0.5L^2z - L^2\delta &= 0 \end{aligned} \quad (2-18)$$

The angle between planes is the angle between their normal vectors. If $A_1x + B_1y + C_1z + D_1 = 0$ and $A_2x + B_2y + C_2z + D_2 = 0$ are plane equations, then angle between planes can be found using the following formula:

$$\alpha = \cos^{-1} \left(\frac{|A_1A_2 + B_1B_2 + C_1C_2|}{(A_1^2 + B_1^2 + C_1^2)^{1/2} (A_2^2 + B_2^2 + C_2^2)^{1/2}} \right)$$

So the angle between two planes under yielding is given as:

$$\cos 2\theta = \cos(\pi - 2\varphi L^*) = \frac{L^2\delta^2 - 0.25L^4}{\sqrt{(L^2\delta^2 + 0.25L^4)}\sqrt{(L^2\delta^2 + 0.25L^4)}} = \frac{4\delta^2 - L^2}{4\delta^2 + L^2} \quad (2-19)$$

$$\varphi = \frac{1}{2L^*} \cos^{-1} \left(\frac{-4\delta^2 + L^2}{4\delta^2 + L^2} \right)$$

Deflection- curvature relationship is given as:

$$\delta = \frac{L}{2} \sqrt{\frac{1 - \cos 2\varphi L^*}{1 + \cos 2\varphi L^*}} \quad (2-20)$$

Where δ is the deflection, φ is the curvature, L^* is the hinge length and L is the dimension of the slab.

2.3.3 Curvature-Deflection Relationship for Rectangular Slab

Two cases are evaluated, a simplified case where the geometry of deformation is pre-specified, and a second case where the angle of the deformation is a variable. These are referred to as case (a) and case (b) and are addressed below.

Case (a) Yield Lines at edges are at 45° Angle to the sides

Let us assume a rectangular slab with length a and breadth b for which yield lines are at 45° to the sides and meet at points as show in the figure 2.11 below and maximum deflection occurs at that point.

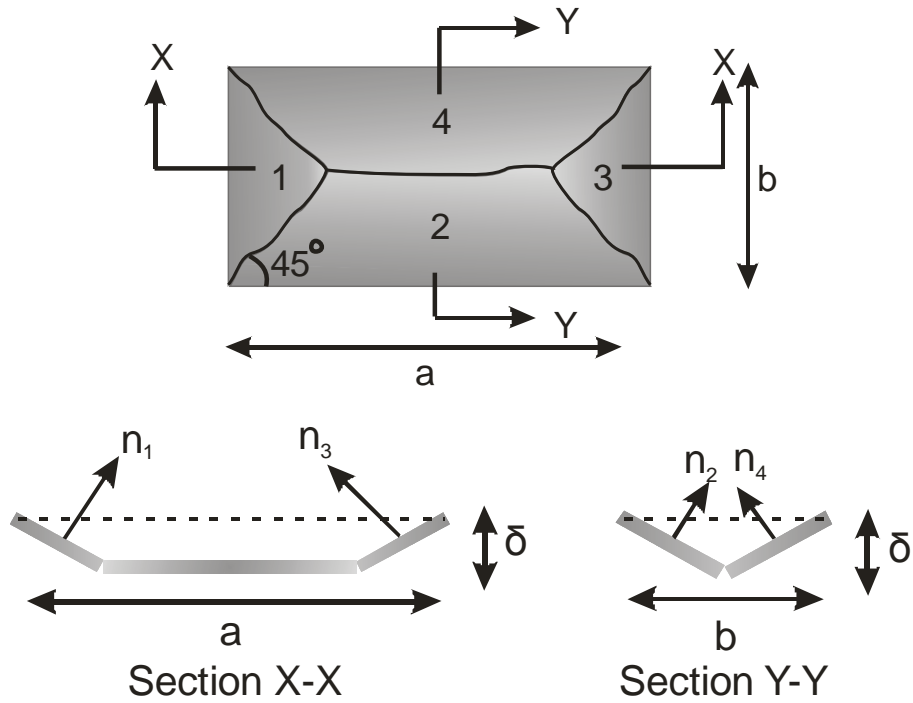


Figure 2.11 Load-deflection relationship for Rectangular slab

To find the angle of rotation, we first find the angle at center between two surfaces.

Curvature, ϕ and angle between the planes, 2θ can then be related as $\phi = \frac{1}{L^*} \left[\frac{\pi}{2} - \theta \right]$. For

finding the angles between both surfaces we find the angle that the normal to these surfaces make with each other.

First we find the angle between planes 1 and 3. This is similar to the case of square slab.

As we obtain the results we see that deflection expression is same as that obtained for square slab of dimension b .

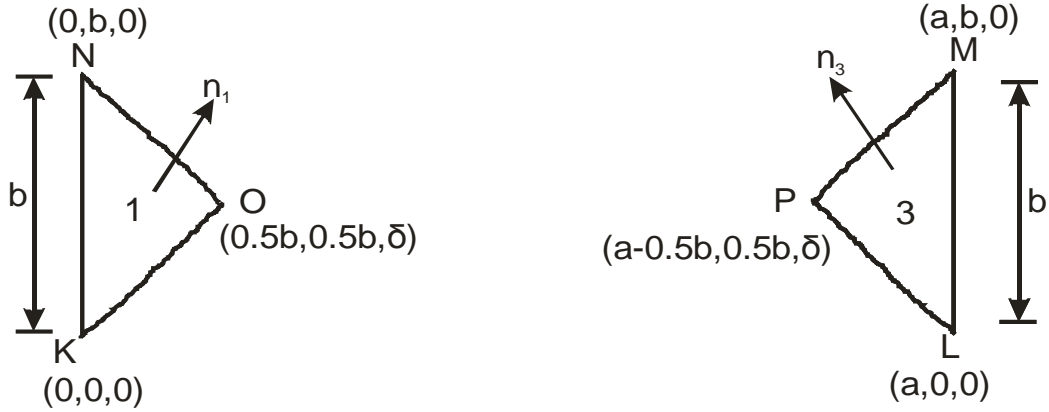


Figure 2.12 Planes KON and PLM

For plane # 1 (KON), normal n_1 is obtained by the cross product of vectors \overline{KO} and \overline{KN} .

$$\overline{KO} = (0.5b, 0.5b, \delta)$$

$$\overline{KN} = (0, b, 0)$$

$$\vec{n}_1 = \overline{KO} \times \overline{KN} = \begin{vmatrix} \hat{i} & \hat{j} & \hat{k} \\ 0.5b & 0.5b & \delta \\ 0 & b & 0 \end{vmatrix} = -b\delta\hat{i} + 0.5b^2\hat{k}$$

Equation of the plane # 1 is given as-

$$\begin{aligned} -b\delta(x-0) + 0(y-0) + 0.5b^2(z-0) &= 0 \\ (b\delta)x - (0.5b^2)z &= 0 \end{aligned} \quad (2-21)$$

For plane # 3 (PLM), the normal n_3 is obtained by the cross product of vectors \overline{LP} & \overline{LM}

$$\overline{LP} = (-0.5b, 0.5b, \delta)$$

$$\overline{LM} = (0, b, 0)$$

$$\vec{n}_2 = \overline{LP} \times \overline{LM} = \begin{vmatrix} \hat{i} & \hat{j} & \hat{k} \\ -0.5b & 0.5b & \delta \\ 0 & b & 0 \end{vmatrix} = (-b\delta)\hat{i} + (-0.5b)b\hat{k}$$

Equation of the plane # 3 is given as

$$\begin{aligned} -b\delta(x-a) + 0(y-0) + (-0.5b)b(z-0) &= 0 \\ (b\delta)x + (0.5b^2)z - ab\delta &= 0 \end{aligned} \quad (2-22)$$

So the angle between two planes under yielding is given as-

$$\cos 2\theta_{13} = \cos(\pi - 2\varphi_{13}L^*) = \left(\frac{b^2\delta^2 - 0.25b^4}{\sqrt{(b^2\delta^2 + 0.25b^4)}\sqrt{(b^2\delta^2 + 0.25b^4)}} \right) = \frac{4\delta^2 - b^2}{4\delta^2 + b^2}$$

Deflection in terms of curvature can be simplified as:

$$\delta = \frac{b}{2} \sqrt{\frac{1 - \cos 2\varphi_{13}L^*}{1 + \cos 2\varphi_{13}L^*}} \quad (2-23)$$

It is known by symmetry that $\varphi_{13} = \varphi_{24}$

Similarly, we find the angle between planes 1 and 4 by the same procedure –

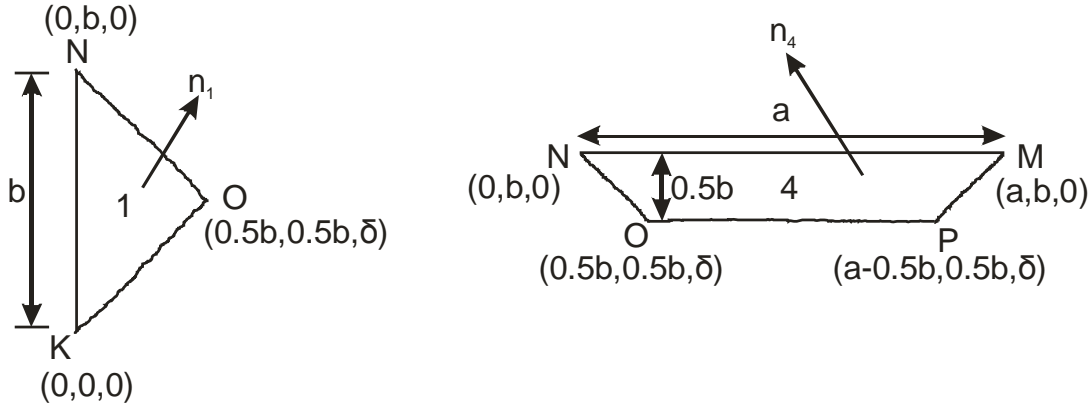


Figure 2.13 Planes KON and NOPM

For plane # 1 (KON), the normal n_1 by the cross product between the vectors \overline{KO} & \overline{KN}

$$\overline{KO} = (0.5b, 0.5b, \delta)$$

$$\overline{KN} = (0, b, 0)$$

$$\vec{n}_1 = \overline{KO} \times \overline{KN} = \begin{vmatrix} \hat{i} & \hat{j} & \hat{k} \\ 0.5b & 0.5b & \delta \\ 0 & b & 0 \end{vmatrix} = (-b\delta)\hat{i} + \frac{(b)b}{2}\hat{k}$$

Equation of the plane # 1 is given as

$$\begin{aligned}
-b\delta(x-0) + 0(y-0) + 0.5b^2(z-0) &= 0 \\
(b\delta)x - 0.5b^2z &= 0
\end{aligned} \tag{2-24}$$

For plane # 4 (NOPM), the normal n_4 is the cross product of vectors \overline{NO} and \overline{NM}

$$\overline{NO} = (-0.5b, 0.5b, -\delta)$$

$$\overline{NM} = (-a, 0, 0)$$

$$\vec{n}_4 = \overline{NO} \times \overline{NM} = \begin{vmatrix} \hat{i} & \hat{j} & \hat{k} \\ -0.5b & 0.5b & -\delta \\ -a & 0 & 0 \end{vmatrix} = (a\delta)\hat{j} + (0.5ab)\hat{k}$$

Equation of the plane # 4 is given as

$$a\delta(y-b) + (-0.5a)b(z-0) = 0$$

$$(a\delta)y + (0.5ab)z - ab\delta = 0$$

So the angle between two planes under yielding is given as-

$$\begin{aligned}
\cos 2\theta_{14} = \cos(\pi - 2\varphi_{14}L^*) &= \left(\frac{-0.25ab^3}{\sqrt{(b^2\delta^2 + 0.25b^4)}\sqrt{(a^2\delta^2 + 0.25a^2b^2)}} \right) = \frac{-b^2}{4\delta^2 + b^2} \\
\varphi_{14} &= \frac{1}{2L^*} \cos^{-1} \left[\frac{b^2}{4\delta^2 + b^2} \right]
\end{aligned} \tag{2-25}$$

Deflection in terms of curvature can be simplified as:

$$\delta = \frac{b}{2} \sqrt{\frac{1 - \cos 2(\varphi_{14}L^*)}{\cos 2(\varphi_{14}L^*)}} \tag{2-26}$$

By the geometry of slab we know that $\varphi_{12} = \varphi_{14} = \varphi_{23} = \varphi_{34}$.

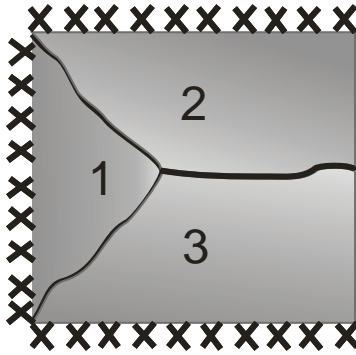


Figure 2.14 Load-deflection for rectangular slab fixed from 3 sides and free from fourth

For a two-way slab supported on 3 sides and free on fourth, the deflection-curvature relationship will remain unchanged and will be equal to equation 2-26.

Case (b) General Yield Lines at variable Angles

This case deals with generalized yield line formation when yield lines are not at 45° to the sides. A dimension of length c has been assumed as shown in figure 2.15, below.

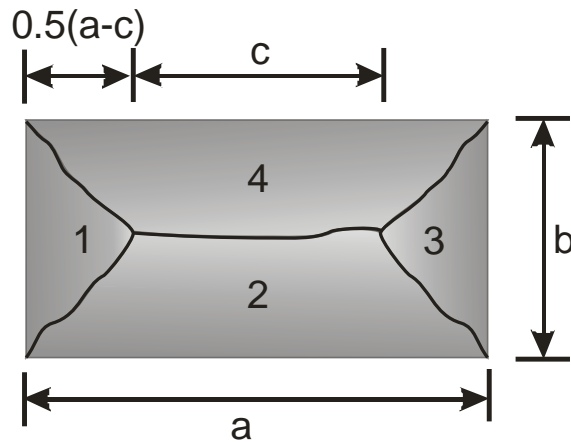
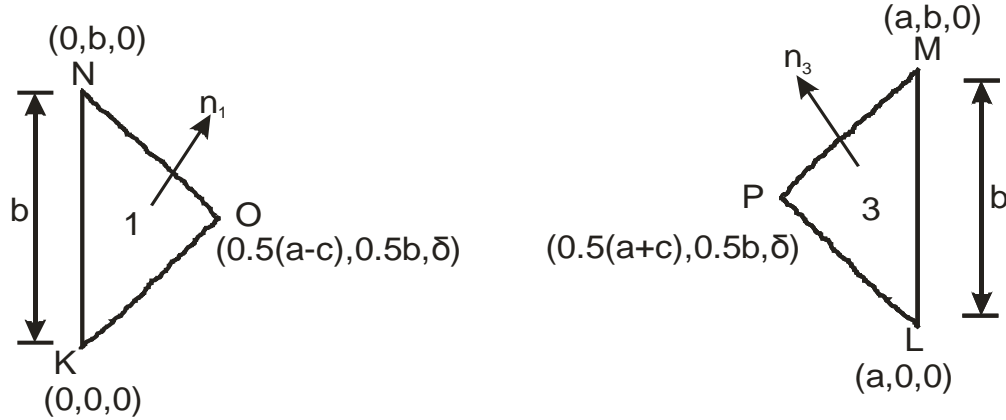


Figure 2.15 Deflection-curvature relationship when yield lines are not at 45°



For plane # 1 (KON), the normal n_1 is the cross product of vectors \overline{KO} and \overline{KN} .

$$\overline{KO} = (0.5(a-c), 0.5b, \delta)$$

$$\overline{KN} = (0, b, 0)$$

$$\vec{n}_1 = \overline{KO} \times \overline{KN} = \begin{vmatrix} \hat{i} & \hat{j} & \hat{k} \\ 0.5(a-c) & 0.5b & \delta \\ 0 & b & 0 \end{vmatrix} = -b\delta\hat{i} + 0.5(a-c)b\hat{k}$$

Equation of the plane # 1 is given as

$$\begin{aligned} -b\delta(x-0) + 0(y-0) + 0.5(a-c)b(z-0) &= 0 \\ b\delta x - 0.5(a-c)bz &= 0 \end{aligned} \quad (2-27)$$

For plane # 3 (PLM), the normal n_3 is the cross product of the vectors \overline{LP} and \overline{LM} .

$$\overline{LP} = (0.5(c-a), 0.5c, \delta)$$

$$\overline{LM} = (0, c, 0)$$

$$\vec{n}_2 = \overline{LP} \times \overline{LM} = \begin{vmatrix} \hat{i} & \hat{j} & \hat{k} \\ 0.5(c-a) & 0.5b & \delta \\ 0 & b & 0 \end{vmatrix} = (-b\delta)\hat{i} + 0.5(c-a)b\hat{k}$$

Equation of the plane # 3 is given as

$$\begin{aligned} -b\delta(x-a) + 0(y-0) - 0.5(a-c)b(z-0) &= 0 \\ (b\delta)x + 0.5(a-c)bz - ab\delta &= 0 \end{aligned} \quad (2-28)$$

So the angle between two planes under yielding is given as-

$$\cos 2\theta = \cos(\pi - 2\varphi L^*) = \frac{b^2 \delta^2 - 0.25(a-c)^2 b^2}{b^2 \delta^2 + 0.25(a-c)^2 b^2} = \frac{4\delta^2 - (a-c)^2}{4\delta^2 + (a-c)^2} \quad (2-29)$$

Deflection in terms of curvature can be simplified as

$$\delta = \frac{1}{2}(a-c) \sqrt{\frac{1 - \cos 2\varphi_{13} L^*}{1 + \cos 2\varphi_{13} L^*}} \quad (2-30)$$

By defining $c = \alpha a$

$$\delta = \frac{a}{2}(1-\alpha) \sqrt{\frac{1 - \cos 2\varphi_{13} L^*}{1 + \cos 2\varphi_{13} L^*}} \quad (2-31)$$

2.3.4 Curvature-Deflection Relationship for Round Panels

Assume a round slab with radius R for with yield lines are originating at the center and extending till the boundary of the slab as shown in the figure 2.16 below and maximum deflection occurs at that center [22].

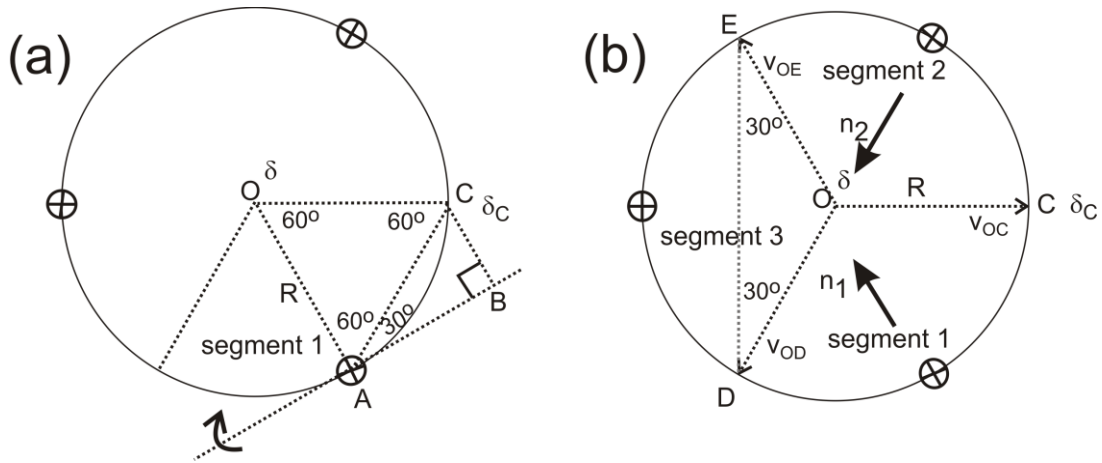


Figure 2.16 Load-deflection relationship for Circular slab

From figure 2.16 crack segment 1 rigidly rotate around the axis AB.

$$\frac{\delta_C}{\delta} = \frac{BC}{AO} = \frac{R \sin(30)}{R} = \frac{1}{2}$$

$$\delta_C = \frac{\delta}{2}$$

Thus, the deflection at the edge (point C) is half that of the center. Assume each crack segment is rigid and it rotates around the crack axis represented by vectors \overline{OC} , \overline{OD} and \overline{OE} as shown in Fig. 2.23.

$$\overline{OC} = (R, 0, 0.5\delta)$$

$$\overline{OD} = (-R \sin(30), -R \cos(30), 0.5\delta)$$

$$\overline{OE} = (-R \sin(30), R \cos(30), 0.5\delta)$$

The vectors normal to crack segment 1 and 2 can be found by cross product of the two adjacent vectors.

$$n_1 = \overline{OD} \times \overline{OC} = \left\{ -\frac{\sqrt{3}}{4} R\delta, \frac{3}{4} R\delta, \frac{\sqrt{3}}{2} R^2 \right\} \quad (2-32)$$

$$n_2 = \overline{OC} \times \overline{OE} = \left\{ -\frac{\sqrt{3}}{4} R\delta, -\frac{3}{4} R\delta, \frac{\sqrt{3}}{2} R^2 \right\} \quad (2-33)$$

The angle of curvature φ between segment 1 and 2 is the angle between these two normal vectors, determined by the dot product.

$$\varphi = \frac{1}{L^*} \cos^{-1} \left\{ \frac{n_1 \cdot n_2}{|n_1| |n_2|} \right\} = \frac{1}{L^*} \cos^{-1} \left\{ \frac{-\delta^2 + 2R^2}{2(\delta^2 + R^2)} \right\} \quad (2-34)$$

Deflection in terms of curvature can be simplified as:

$$\delta = \sqrt{\frac{2R^2(1 - \cos \varphi L^*)}{(1 + 2 \cos \varphi L^*)}} \quad (2-35)$$

2.4 Applied load - Deflection Response

Algorithm to calculate load deflection response for limit state analysis using yield line theory was developed by integrating the three aspects of curvature-deflection relationship with applied load-yield line moment into the moment curvature relationship. As shown in figure 2.17 all the components of the algorithm are defined and one can develop a step wise simplified approach. Using the simplified model for strain hardening cement composites model (Section 1.2) one can approach the problem in the following manner:

- i. For a given cross section and material properties and using $M' - \phi'$ relation from expressions in table 1-2 calculate normalized moment for discrete number of curvature values. Using the normalized moment relation $M = M'(\sigma_{cr}bh^2/6)$ and normalized curvature as $\phi = \phi'(2\varepsilon_{cr}/d)$, the moment-curvature response of the cross-section is obtained.
- ii. Using a discrete number of moment magnitudes along the moment curvature diagram, a load vector is generated using the relationship between moment and load for the panel configurations as derived by the yield line methodology in section 2.2.
- iii. The slab is segmented into finite sections and maximum deflection is calculated using the relationship between curvature and deflection as derived in section 2.3.
- iv. This procedure is applied at each step until a complete load deflection response is obtained for the corresponding moment curvature relationship.

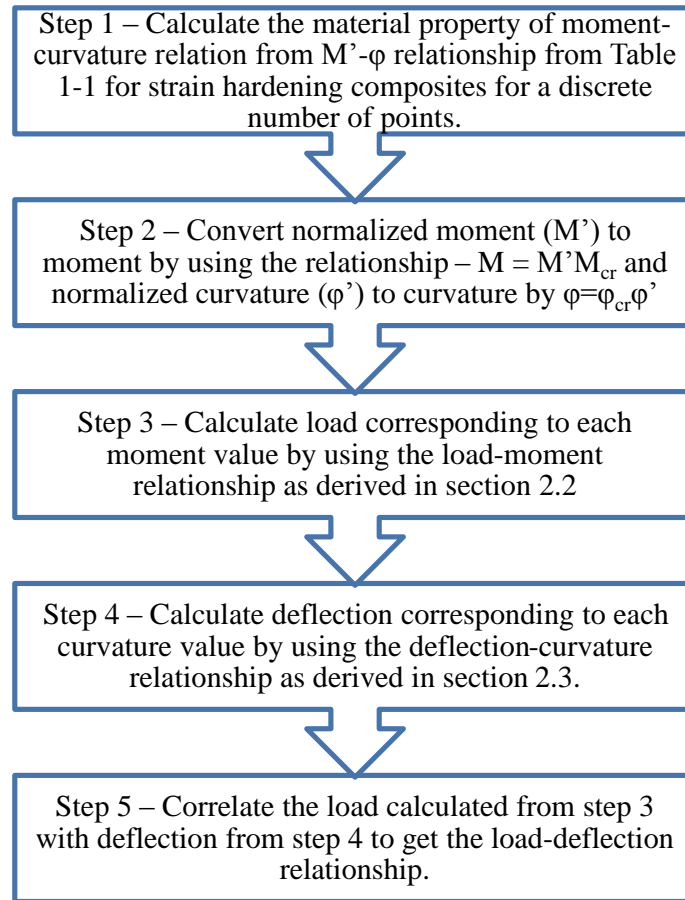


Figure 2.17 Flowchart for the derivation of applied load-deflection relationship for SHCC materials

2.5 Shortcomings of the Methodology - Increased Load Bearing Strength at Large Vertical Displacements

Concrete slabs at large vertical displacements could support loads considerably greater than those calculated using the yield-line approach [21]. The mechanism for supporting the load was shown to be tensile membrane action, which could form within the slab irrespective of whether it was restrained or unrestrained horizontally at its boundaries. For a slab which was unrestrained around its boundaries, compressive in-plane membrane

forces were shown to form within the depth of the slab around its perimeter, and these provided the required support to the in-plane tensile membrane forces in the central region of the slab. The mechanism is shown below in the figure 2.18.

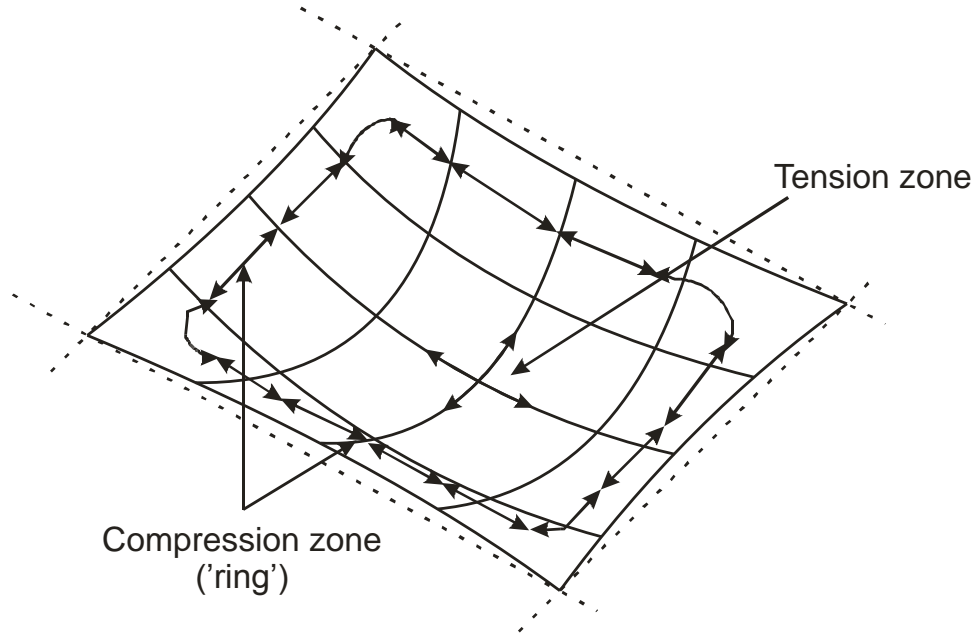


Figure 2.18 Different zones for slabs subjected to large displacements [21]

2.6 Comparison with Experimental Data

2.6.1 Data Set 1

Experimental results from round panel tests analyzed by Soranakom et. al are considered first [22]. The parameter based fit equations for moment curvature relationship are used for stages 2.1 and 3.1 which were obtained by curve fitting the simulated response from the closed form derivations and are applicable within 1% accuracy of the closed form results. Tabix steel fibers are used as the reinforcement in these SHCC material slabs.

Diameters of experimented slabs were 2000 mm and 1500 mm. Simulation was done in following steps:

(a) **Step 1** - Calculate the moment-curvature relationship using the strain hardening cement composites model as discussed in section 1.2 for all the stages. Assume that this material is governed by following stages –

- (i) Stage 1 – Elastic compression, elastic tension
- (ii) Stage 2.1 – Elastic compression, tension hardening
- (iii) Stage 3.1 – Elastic compression, tension softening.

Stages 2.2 and 3.2 are not considered here as it has been observed that tension governs the design instead of compression.

The following parameters are proposed for the design of these samples:

η = Ratio of post crack stiffness to elastic stiffness (E_{cr}/E) = 0.01

γ = Ratio of stiffness in tension and compression (E_c/E) = 1

μ = Post tensile strain capacity, $\frac{\sigma_{cst}}{E_{ocr}} = 0.6$.

Strain capacity parameter, $\alpha = \frac{\epsilon_{tm}}{\epsilon_{cr}}$, $\alpha = 10$. This parameter represents the ultimate strain

capacity in the section with the reduced tensile stiffness. The following simplified relations are obtained after the closed form solutions to the moment curvature relationship are subjected to a polynomial curve fit approach. For a homogeneous and an isotropic plate, the bending stiffness, D will be given as $EI / (1-\nu^2)$. As square of poisson's ratio will be a very small number, therefore elastic stiffness can be approximated as EI.

$$M = EI(\varphi) \quad (\text{Stage 1})$$

For stages 2.1 and 3.1, while the closed form equations can be easily used individually, it may be easier to apply a curve fit to the entire relationship between normalized moment (M') and normalized curvature (φ') in these two regions as:

$$M' = 1.342 + 0.371\sqrt{\varphi'} \quad (\text{Stage 2.1})$$

$$M' = 2.34e^{-5}\varphi'^4 - 0.0017\varphi'^3 + 0.0481\varphi'^2 - 0.5551\varphi' + 3.9454 \quad (\text{Stage 3.1})$$

(b) **Step 2** - Convert from the normalized moment and curvature for stages 2.1 and 3.1 to moment-curvature by factoring in the cracking moment and curvature corresponding to first cracking.

$$M = M' M_{cr} = [M'] \frac{\sigma_{cr} b h^2}{6}$$

$$\varphi = \varphi' \varphi_{cr} = [\varphi'] \frac{2\varepsilon_{cr}}{d}$$

For radius as 1000 mm, thickness 200 mm, cracking strain as $100\mu\text{str}$ and cracking stress as 3 MPa, one obtains for stage 2:

$$\begin{aligned} M &= \left[1.342 + 0.371\sqrt{\varphi \frac{2(100)(10^{-6})}{0.2}} \right] \frac{3(10^6)(4)(0.2)^2}{6} \\ &= 7.98 \left[1.342 + 0.371\sqrt{0.001\varphi} \right] 10^5 \text{ N} - m \end{aligned}$$

Similar expression can also be calculated for stage 3.1.

(c) **Step 3** - Since the sample is simply supported on all sides subjected to point load, from section 2.2 one can use the following moment-load relationship as equation 2-4.

$$m = \frac{P}{2\pi} \quad \text{Case (3.1)}$$

(d) **Step 4** – From section 2.3 the appropriate expression for curvature-deflection relationship for a square slab is given by equation 2-35 as below is used. From table 2-4, it can be seen that hinge length can be approximated to lie in the range of 10 mm to 50 mm. Hinge length is assumed as 10 mm for simplification. Figure 2-21 shows the effect of hinge length

$$\delta = R \sqrt{\frac{2(1 - \cos \phi L^*)}{(1 + 2 \cos \phi L^*)}}$$

(e) **Step 5** – Calculate the load-deflection result using the results from steps 3 and 4. From figure 2.20 it can be seen that only stages 1 and 2.1 are applicable and material does not go into tension softening corresponding to stage 3.1 as which can be attributed to high volume fraction of fibers.

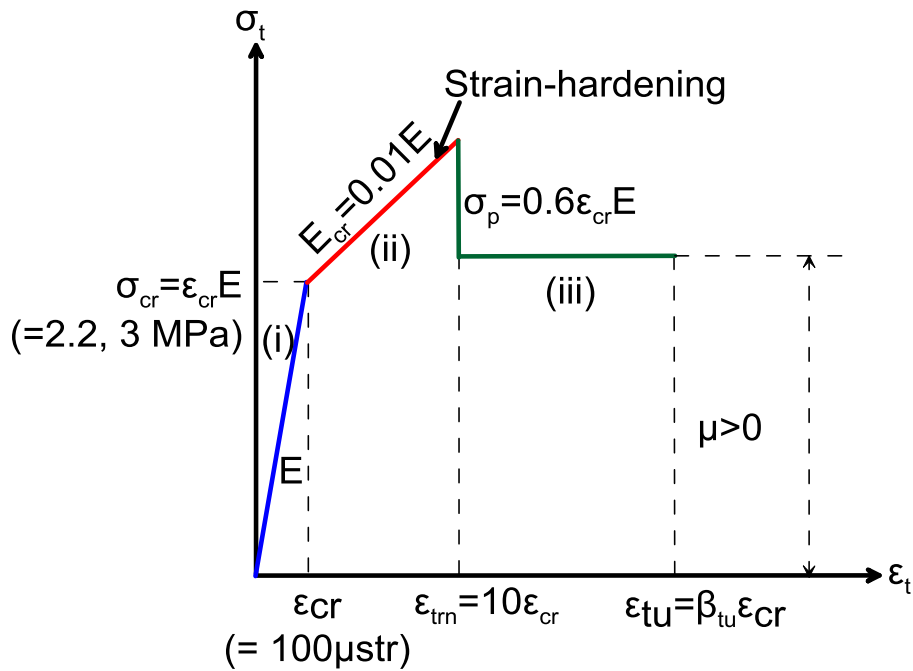


Figure 2.19 Strain hardening-softening tension model with the parameters used for fitting the model ($\eta=0.01$, $\mu=0.6$, $\alpha=5$)

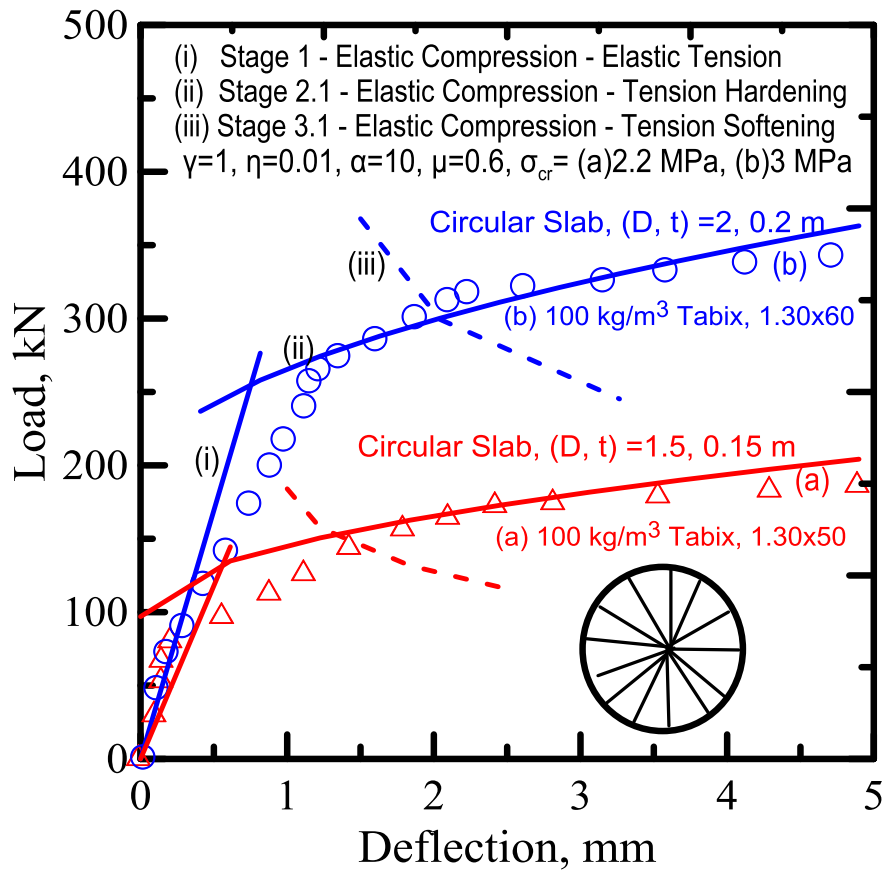


Figure 2.20 Comparison of experimental results with methodology for round panels

Figure 2.21 shows the effect of hinge length, L^* on the load-deflection response. From figure 2.21 it can be seen that for a strain capacity parameter, α value of 100, stage 3.1 can be delayed which is applicable for this dataset.

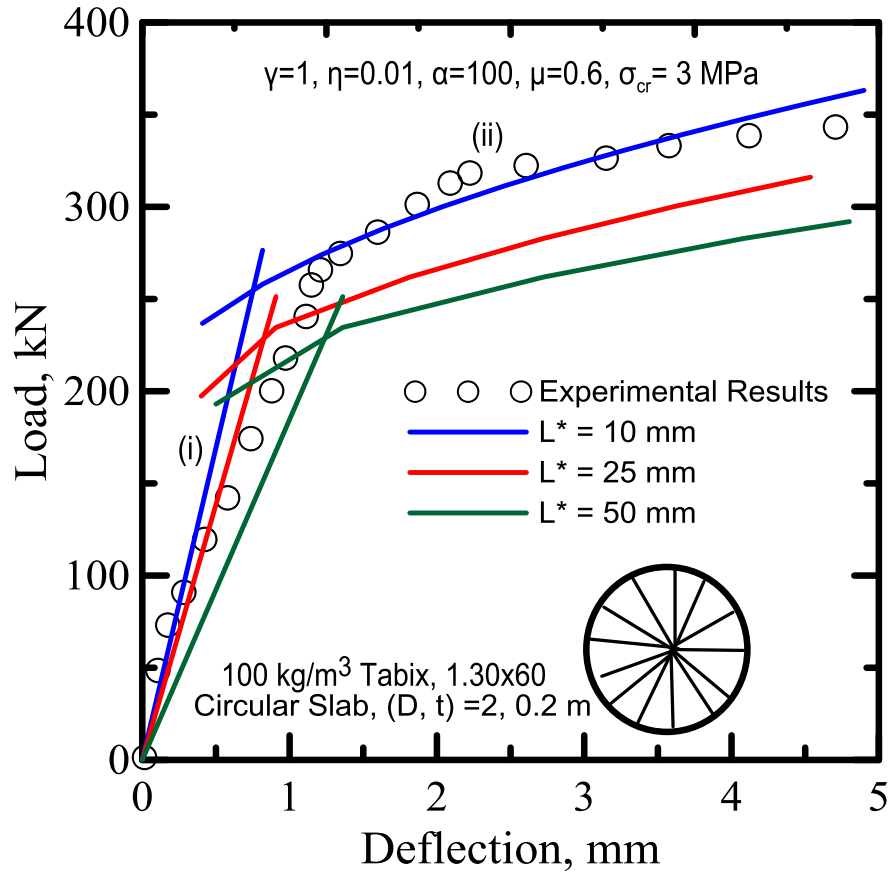


Figure 2.21 Effect of hinge length on simulated results

2.6.2 Data Set 2

Experimental results for square slabs are considered in a study published by Khaloo and Afshari here [23]. Results were digitized for comparison. The parameter based fit equations for moment curvature relationship are used for stages 2.1 and 3.1 which were obtained by curve fitting the simulated response from the closed form derivations and are applicable within 1% accuracy of the closed form results. Span of slabs was 680 mm x 680 mm with 80 mm thickness. Original test data is as shown below:

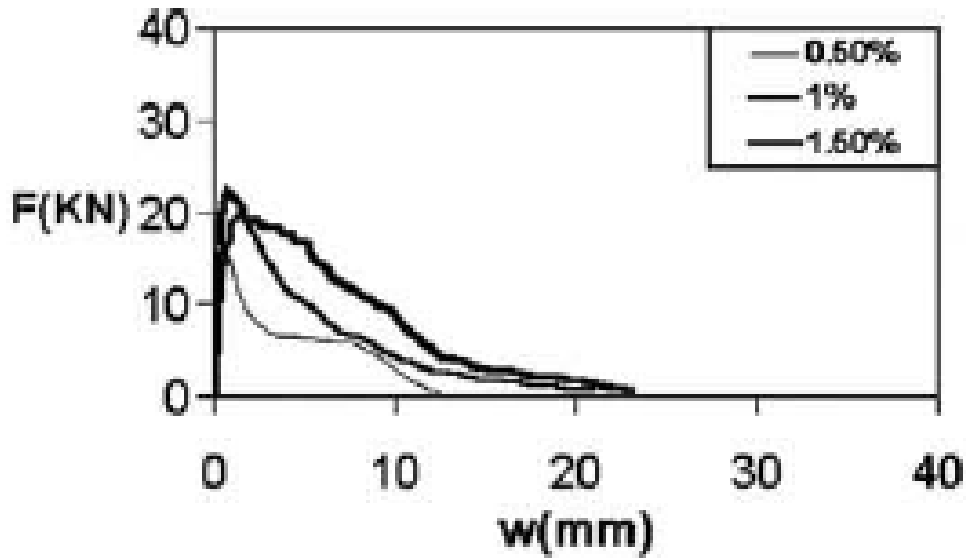


Figure 2.22 Experimental results for square slabs [23]

Steps for simulation are shown below -

Step 1 – Similar to data set 1, if one starts with calculating the moment curvature relationship using the strain hardening cement composites model as discussed in section 1.2. One can find the moment curvature response for the stages 1, 2.1 and 3.1.

The following parameters are proposed for the design of these samples –

Ratio of post crack stiffness to elastic stiffness (E_{cr}/E), $\eta = 0.01$

For strain hardening materials ($\gamma = E_c/E$), use equal stiffness in tension and compression $\gamma=1$.

Post tensile strain capacity, $\frac{\sigma_{cst}}{E_{ecr}}$, $\mu=0.4$.

Strain capacity parameter, $\frac{\epsilon_{tm}}{\epsilon_{cr}}$, $\alpha=10$. This parameter represents the ultimate strain

capacity in the section with the reduced tensile stiffness. The following simplified relations are obtained after the closed form solutions to the moment curvature

relationship are subjected to a polynomial curve fit approach. For a homogeneous and an isotropic plate, the bending stiffness, D will be given as $EI/(1-\nu^2)$. As square of poisson's ratio will be a very small number, therefore elastic stiffness can be approximated as EI.

$$M = EI(\varphi) \quad (\text{Stage 1})$$

For stages 2.1 and 3.1 we get relationship between normalized moment (M') and normalized curvature (φ') which we convert to moment-curvature as shown in step 2.

$$M' = 1.342 + 0.371\sqrt{\varphi'} \quad (\text{Stage 2.1})$$

$$M' = 1.933e^{-4}\varphi'^4 - 0.01435\varphi'^3 + 0.3862\varphi'^2 - 4.4898\varphi' + 20.2440 \quad (\text{Stage 3.1})$$

Step 2 – We then convert the normalized moment and curvature for stages 2.1 and 3.1 to moment-curvature by factoring in the cracking moment and curvature corresponding to first cracking.

$$M = M' M_{cr} = [M'] \frac{\sigma_{cr} b h^2}{6}$$

$$\varphi = \varphi' \varphi_{cr} = [\varphi'] \frac{2\varepsilon_{cr}}{d}$$

For clear span as 680 mm, thickness 80 mm, cracking strain as $40\mu\text{str}$ and cracking stress as 0.6 MPa, we get –

For stage 2.1 we get –

$$M = \left[1.342 + 0.371\sqrt{\varphi \frac{2(40)(10^{-6})}{0.08}} \right] \frac{0.6(10^6)(4)(0.2)^2}{6}$$

$$= 1.59 \left[1.342 + 0.371\sqrt{0.001\varphi} \right] 10^5 \text{ N-m}$$

Similar expression can also be calculated for stage 3.1.

Step 3 - The end conditions are simply supported on all sides. From section 2.2 we get the moment-load relationship as-

$$\text{For point load - } m = \frac{q}{24} \quad (\text{Case 1.1})$$

Step 4 – From section 2.3 the appropriate expression for curvature-deflection relationship for a square slab is given by equation 2-20 as below is used. From table 2-4, it can be seen that hinge length can be approximated to lie in the range of 10 mm to 25 mm. Hinge length is assumed as 10 mm for simplification.

$$\delta = \frac{L}{2} \sqrt{\frac{1 - \cos 2\phi L^*}{1 + \cos 2\phi L^*}}$$

Step 5 – Calculate the load-deflection result using the results from steps 3 and 4.

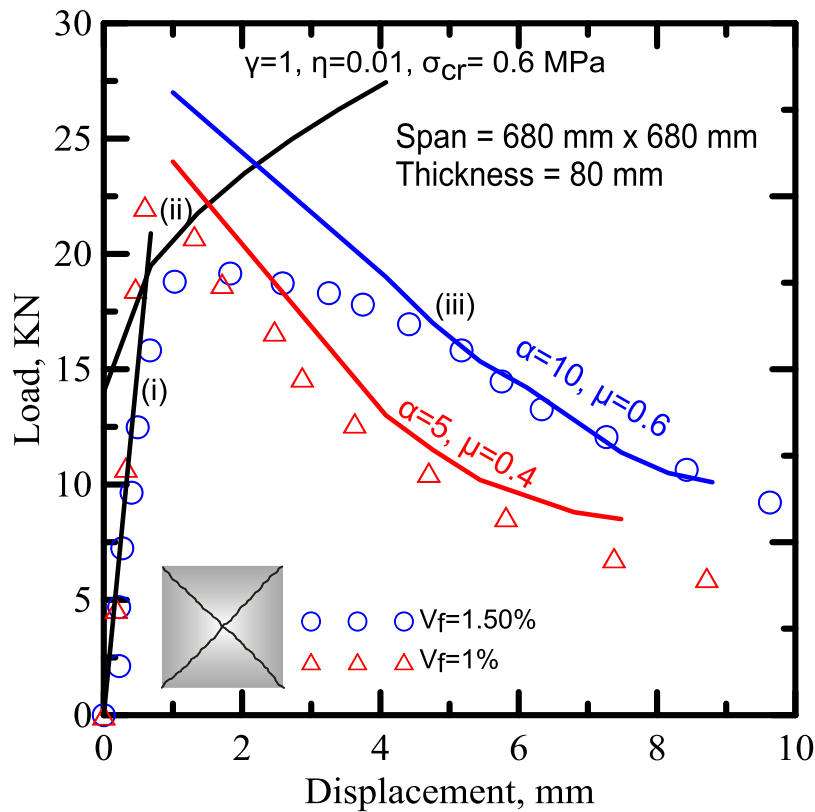


Figure 2.23 Comparison of experimental results with the methodology for square panels

2.7 Interaction of the Different Tensile Zones on the Load-Deflection Response of the Panels Based on the Moment-Curvature and Limit Analysis

Assuming that the kinematics of the problem do not change as the sample cracks and deforms, one can start the problem from the elastic response using the panel's initial bending stiffness D as, $D = EI/(1-\nu^2)$. This example illustrates how load deflection response can be simulated for a strain hardening material with known material properties such as moment-curvature relationship, cracking moment, hinge length, geometry and end conditions. Additionally the formulation addresses the interactions between the different modes of failure in stages 2.1 and 3.1 of the model presented in section 1.2. Instead of using various criteria for failure, both mechanisms of 2.1 and 3.1 are used independently and the results superposed in order to show the transition from one mode to the other. Let us assume a square slab of length 4000 mm, thickness 200 mm, cracking stress 1 MPa and factor η (E_{cr}/E) as 0.01.

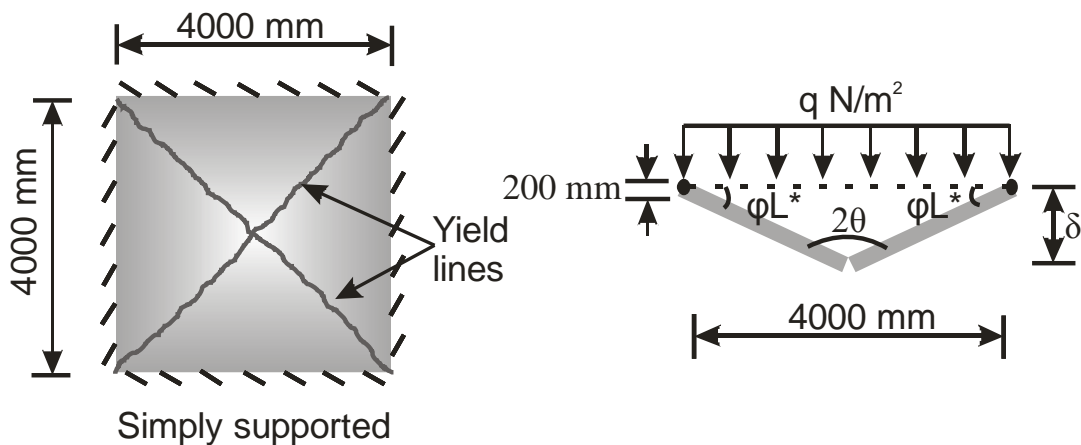


Figure 2.24 Problem parameters

Step 1 – The starting point of the procedure is the moment curvature relationship using the strain hardening cement composites model as discussed earlier obtained for all the stages defined as:

- (i) Stage 1 – Elastic compression, elastic tension
- (ii) Stage 2.1 – Elastic compression, tension hardening
- (iii) Stage 3.1 – Elastic compression, tension softening.

Stages 2.2 and 3.2 are not considered here under the assumption that tension governs the design instead of compression. They can be easily added to the formulation. In the present example the following parameters for design are used:

η = Ratio of post crack stiffness to elastic stiffness (E_{cr}/E) = 0.01

γ = Tensile to compressive stiffness ratio, (E_c/E) = 1

μ = Post tensile strain capacity, $\frac{\sigma_{cst}}{E_{cer}} = 0.6$

α = Strain capacity at the ultimate tensile strength, $\frac{\epsilon_{tm}}{\epsilon_{cr}} = 10$

The following simplified relations obtained by curve fitting the results of moment curvature relationship in accordance with the procedures developed by Mobasher [24] are used:

For a homogeneous and an isotropic plate, the bending stiffness, D will be given as $EI/(1-\nu^2)$. As square of poisson's ratio will be a very small number, therefore elastic bending stiffness can be approximated as EI.

$$M = EI(\varphi) \qquad \text{Stage 1}$$

For stages 2.1 and 3.1 we get relationship between normalized moment (M') and normalized curvature (φ') which we convert to moment-curvature as shown in step 2.

$$M' = 1.342 + 0.371\sqrt{\varphi'} \quad \text{Stage 2.1}$$

$$M' = 2.34e^{-5}\varphi'^4 - 0.0017\varphi'^3 + 0.0481\varphi'^2 - 0.5551\varphi' + 3.9454 \quad \text{Stage 3.1}$$

Step 2 – The normalized moment and curvature for stages 2.1 and 3.1 are scaled to sectional moment-curvature by incorporating the moment and curvature corresponding to first cracking point.

$$M = M' M_{cr} = [M'] \frac{\sigma_{cr} b h^2}{6}$$

$$\varphi = \varphi' \varphi_{cr} = [\varphi'] \frac{2\varphi_{cr}}{d}$$

For stage 2.1, and using a length of 4000 mm, thickness 200 mm, cracking strain as $100\mu\text{str}$ and cracking stress as 1 MPa, one obtains:

$$\begin{aligned} M &= \left[1.342 + 0.371 \sqrt{\varphi \frac{2(100)(10^{-6})}{0.2}} \right] \frac{(10^6)(4)(0.2)^2}{6} \\ &= 2.66 \left[1.342 + 0.371 \sqrt{0.001\varphi} \right] 10^5 N - m \end{aligned}$$

Similar expression can also be calculated for stage 3.1.

Step 3 – The load-moment relationship can be obtained from the equations 2-4. In this case, assume that the end conditions are simply supported on all sides. From section 2.2 the moment-load relationship is obtained as:

$$m = \frac{qL^2}{24} \quad (\text{Uniformly distributed load})$$

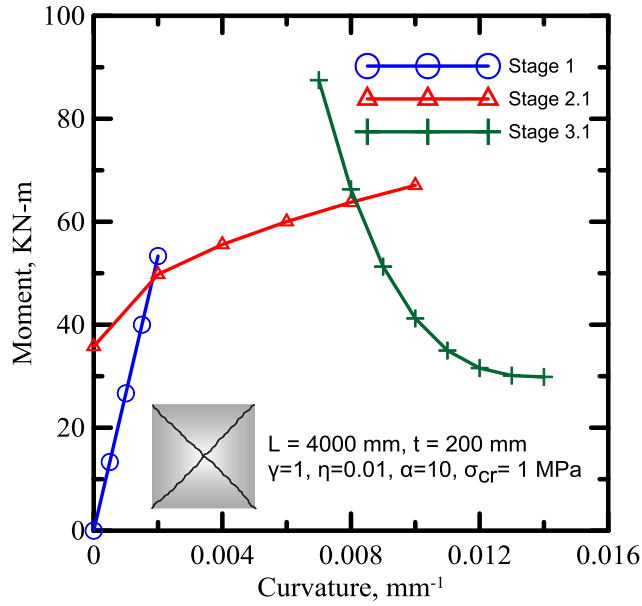


Figure 2.25 Moment-curvature relationship for SHCC

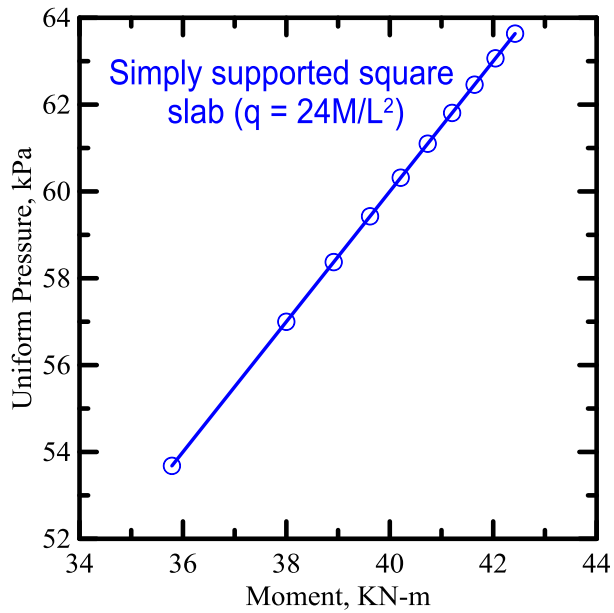


Figure 2.26 Moment-load response for (a) uniformly distrib. load, (b) point load at center.

Step 4 –Computation of Deflection-rotation response is obtained from section 2.3 where one obtains the expression for a square slab.

$$\delta = \left[\frac{L^2 [1 - \cos 2\varphi]}{4(1 + \cos 2\varphi)} \right]^{1/2}$$

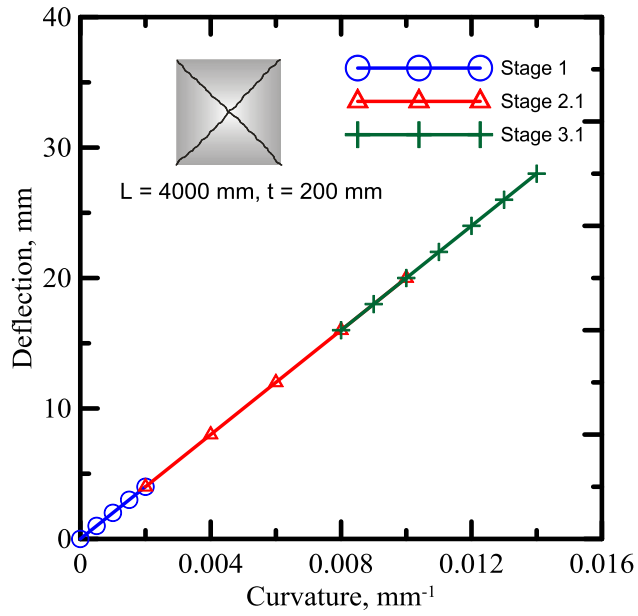


Figure 2.27 Deflection-curvature relationship

Step 5 – Finally one can calculate the load-deflection using the results from steps 1 to 4.

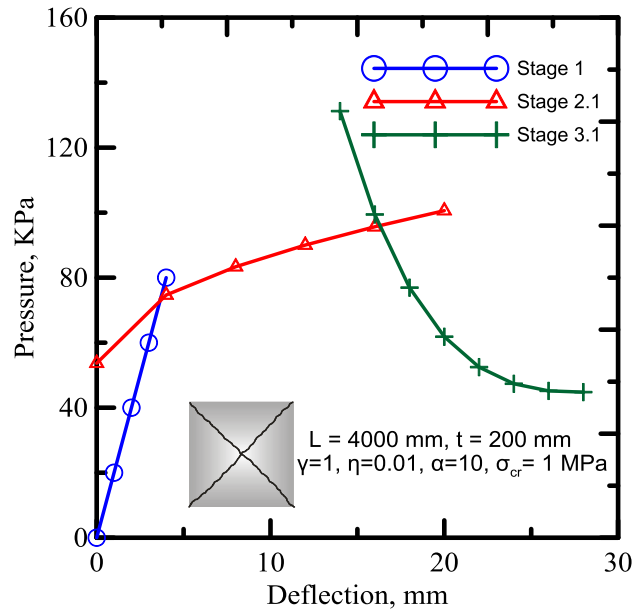


Figure 2.28 (a) Applied load-deflection relationship

Load-deflection response shown in figure 2.28 can then be integrated to give a response as shown in figure 2.29.

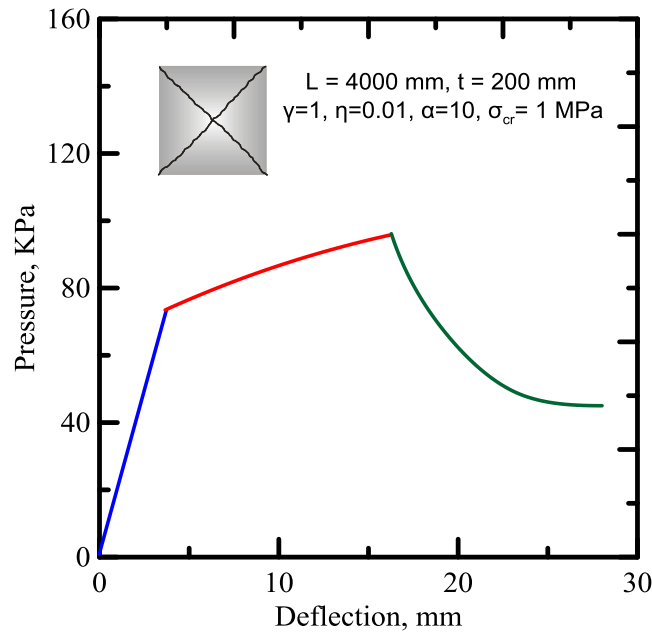


Figure 2.29 (b) Equivalent applied load-deflection relationship

2.8 Post-Crack Analysis of ASTM C1550 Test results using the Proposed Yield Line Load-Deflection Model

The proposed methodology can be used to define an effective stiffness of cracked concrete slabs under flexure. Using the moment rotation curve, one can introduce an effective stiffness using a tangent stiffness of approach to obtain the instantaneous stiffness of the fully cracked panel. The test results of ASTM C1550 [25] are used in order to verify the proposed methodology. Samples are tested using a round panel of dimensions 800 mm diameter and 75 mm thickness, that is resting on three pivotal points and subjected to a point load and were made from synthetic macro fibers.

Moment deflection relationship was proposed by Johansen [26] which can also be extended to calculate the load deflection response by implementing applied load and yield line moment relationship. Johansen showed that by a suitable choice of a one-way strip taken out of any slab with a uniformly distributed load, restrained or simply supported and analyzed using the yield line theory, the deflection, δ , could be estimated by the formula:

$$\delta = \frac{M_u L^2}{8EI} \quad (2-36)$$

This method can be implemented to SHCC using the tri-linear model as discussed in chapter 1 with the objective of fitting the results from full scale tests. The yield line method shows to be highly effective in the design of 2-D plane members subjected to bending, owing to its handiness and closeness to the actual structural behavior. Inserting the moment in terms of point load as found in equation number 2-14, we get the deflection load relationship as –

$$\delta = \frac{\frac{P}{2\pi} R^2}{8EI} = \frac{PR^2}{16\pi EI} \quad (2-37)$$

The stiffness parameter in the load deflection expression has been modified to accommodate the post peak behavior as defined in the SHCC model in chapter 1. The final equation takes the form as:

$$EI_{eff} = \frac{M' M_{cr}}{\phi' \phi_{cr}} \quad (2-38)$$

$$P = k_{eff} \delta \quad ; \quad k_{eff} = \frac{16\pi M' M_{cr}}{R^2 \phi' \phi_{cr}} \quad (2-39)$$

As this is a yield-line type analysis, therefore it is applicable only after the formation of yield lines. By using this approach, one cannot fit the peak response. The comparison shows that the yield line method provides a good estimation of the load bearing capacity of the slab after the peak load failure (formation of yield lines).

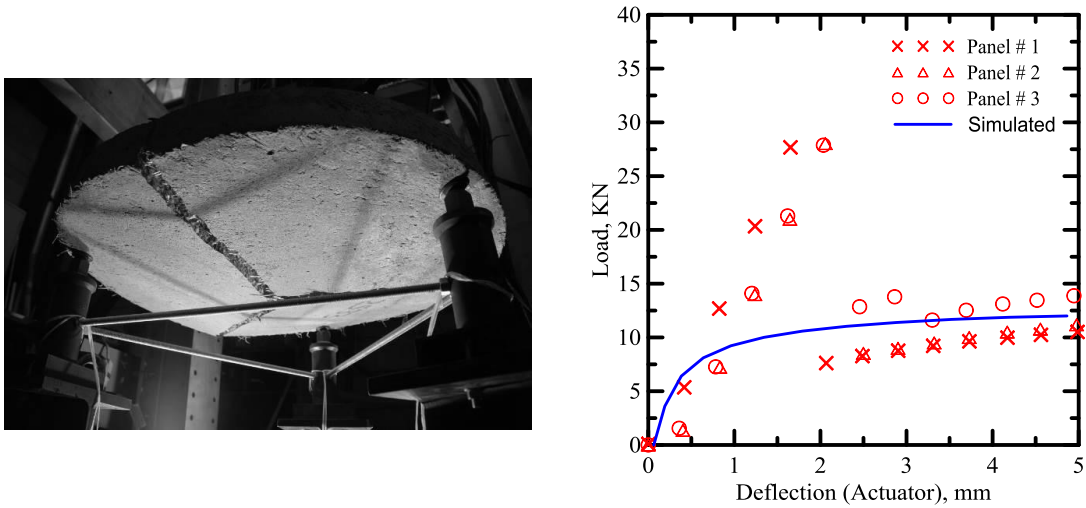


Figure 2.30 Round panel tests (a) Test set up, (b) Comparison between the experimental data and simplified model based on Johansen’s formula

The results from the equation 2-39 above and test results on a SHCC material circular slab are compared in figure 2.30. As it can be seen that initially yield line approach can only be applicable after the post peak phase which is after the formation of yield lines.

3. CHAPTER 3 - SHEAR PROPERTIES OF TEXTILE REINFORCED CONCRETE BY MECHANICAL TESTS AND DIGITAL IMAGE CORRELATION

The study of textile reinforced concrete (TRC) composites has progressed since the mid-1990s. Researchers have become increasingly interested in TRC composites because of their wide range of rheological, mechanical, chemical and aesthetic characteristics [27]. This interest is also related to the diversity of TRC applications, primarily for light work and potentially for structural work. For structural applications, TRC is primarily used under tensile solicitation (e.g. integrated formwork elements and repair and/or strengthening of reinforced concrete structures). However, the deformation behavior of the composite is greatly associated with the relative motion, thus primarily depending on the shear behavior of the fabric, which determines its performance properties when subjected to a wide variety of complex deformations, as well as its conformance to the required shape. Therefore, the in-plane shear strain can influence the behavior of certain TRC structures and can lead to their failure. The estimation of TRC's shear resistance contribution in design, which is presently deducted from TRC's tensile property, requires various investigations since the shear resistance mechanism is usually complicated [28]. Thus, to broaden the spectrum of TRC applications and get more accurate shear properties, an experimental study was conducted to characterize the in-plane shear behavior of TRC composites.

For textile reinforced concrete there is no set standard test method for determining the in-plane shear behavior. There are three main known techniques used to measure shear compliance, namely the Direct Shear Force Measurement (DSFM) method, the Bias-Extension test method, and the picture frame test method. Literature search indicated that the bias extension approach usually brings out a complex combination of shear and tension which makes it difficult to isolate the shear deformation in the test and hence complicates the characterization of pure shear behavior [29]. In the picture-frame shear test, a sample is clamped within a square frame hinged at each corner. The two diagonally opposite corners are then displaced using a mechanical testing machine. A uniform shear deformation state is produced. Therefore pictures frame was used to impose a pure in-plane shear kinematics to the specimen.

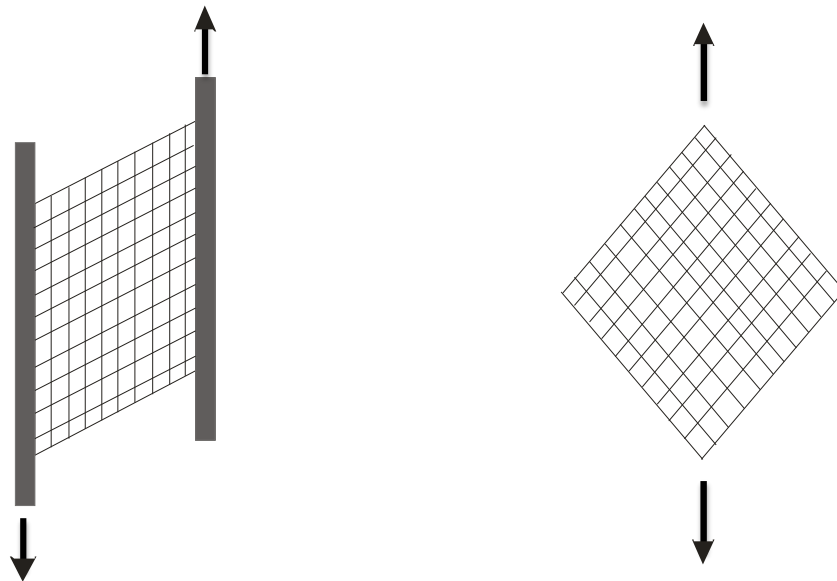


Figure 3.1 Methods of measuring shear force – (a) direct shear force measurement and (b) picture frame test

3.1 Experimental Program

A partial fly-ash substituted cement based mix design was used in the pultrusion process for making the samples as described in section 1.3. Mixture proportions of the ingredients are listed in table 3-1. Constituents of the mix are weighted and mixed using standard Hobart mixer.



Figure 3.2 Standard Hobart mixer

Table 3-1 : Mix design

| Material (each batch) | Percentage (by weight) |
|--------------------------|------------------------|
| Cement | 49.20 |
| Fly ash | 24.60 |
| Water ~ Room temperature | 25.80 |
| Super plasticizer | 0.01 |

3.2 Shear Test Procedure and Instrumentation

The specimen was clamped on the picture frame fixture by bolting the three holes on all four sides and the bolts were carefully tightened. It is very important that a constant amount of force should be applied when tightening the bolts. Loose pinning of the sample edges in the clamps may fail to induce the required kinematics, whereas tight clamping of the sample edges can cause spurious results if the sample is even slightly misaligned [30]. Then the whole fixture with attached specimen was placed onto the hydraulic grips of the testing machine, and connected with the crossheads. Top hydraulic grip was attached to the load cell to measure the force and bottom hydraulic grip was attached to the actuator. After that, the distance between the upper and lower crossheads was adjusted, and it was ensured that the angles between the arms of fixture were 90° [31]. The current distance was set as the original reference value, i.e., the displacement is made zero, in computer, so that later on, all the experiments can automatically begin from this zero point. Also, the force was adjusted to be zero at this position. Loading was at a designated speed (2.5mm/min) by moving the actuator down until the end of the test. Digital data acquisition for the instron machine collected data at every 0.5 seconds.

After several trials of this test, the average value of load, at each displacement point was calculated. The load-displacement relationship of the empty frame was also calculated by following the same procedure without the specimen. This is to record the load-displacement behavior of the empty fixture under the same condition as in the real shear experiment to calculate the resistance provided by the frame.

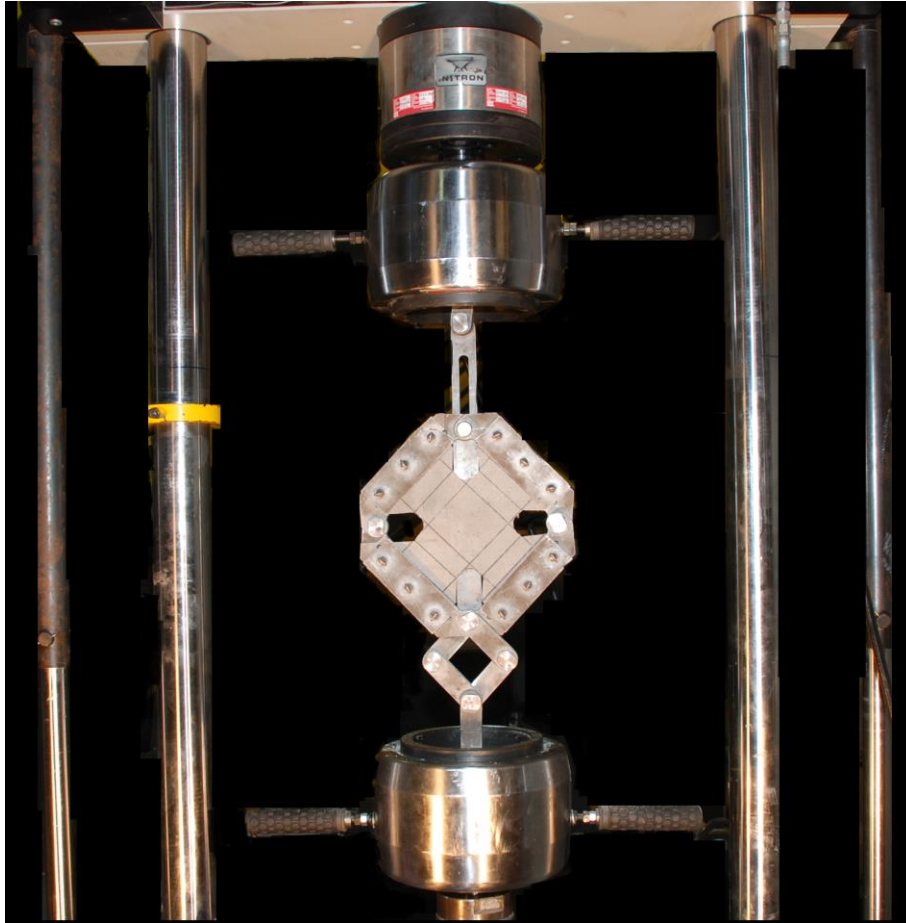


Figure 3.3 Test set-up

Simultaneously, the photos were taken of the deforming specimen at a constant rate of 10 frames per second. This is the slowest speed for the high speed phantom cameras that were used. At the end of every test, the crosshead was recovered to the zero point again. The deformed specimen was taken down and a new sample was clamped to do another round of test.

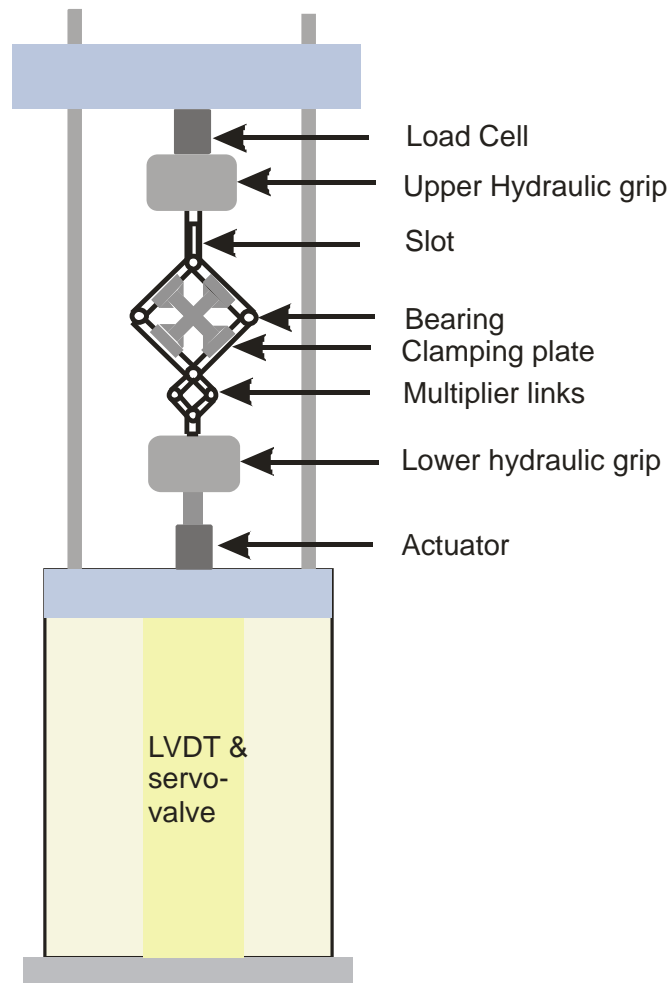


Figure 3.4 Schematics of test set-up

The rig is jointed at each corner such that its sides can rotate and the interior angle between adjacent sides can change. The initially square frame thus becomes of rhomboid (or diamond) shape. Figure 3.5 show the different stages during the experiment showing the sample going from initial configuration of square to rhomboid. Material inside the rig is subjected to pure shear deformation kinematics. The force required to deform the material is recorded at the load cell connected to the top crosshead. From this information the shear force (or stress) can be determined as a function of shear angle and shear angle rate.

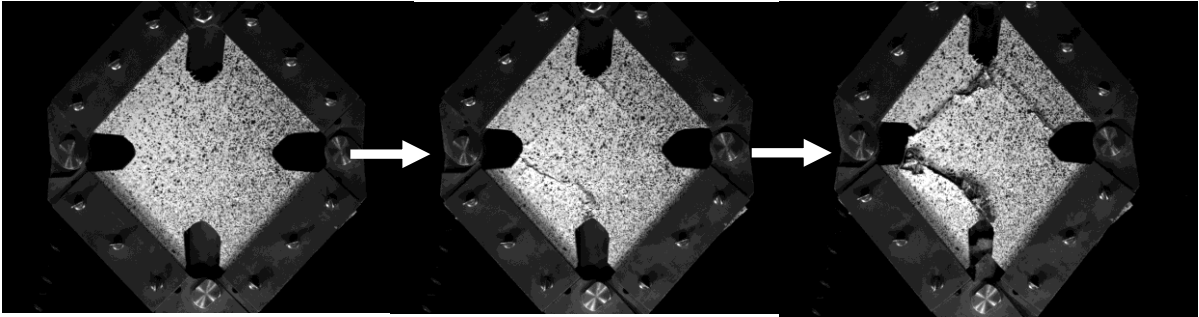


Figure 3.5 Different stages of experiment

3.3 Data Reduction Methods

3.3.1 Determination of Shear Force

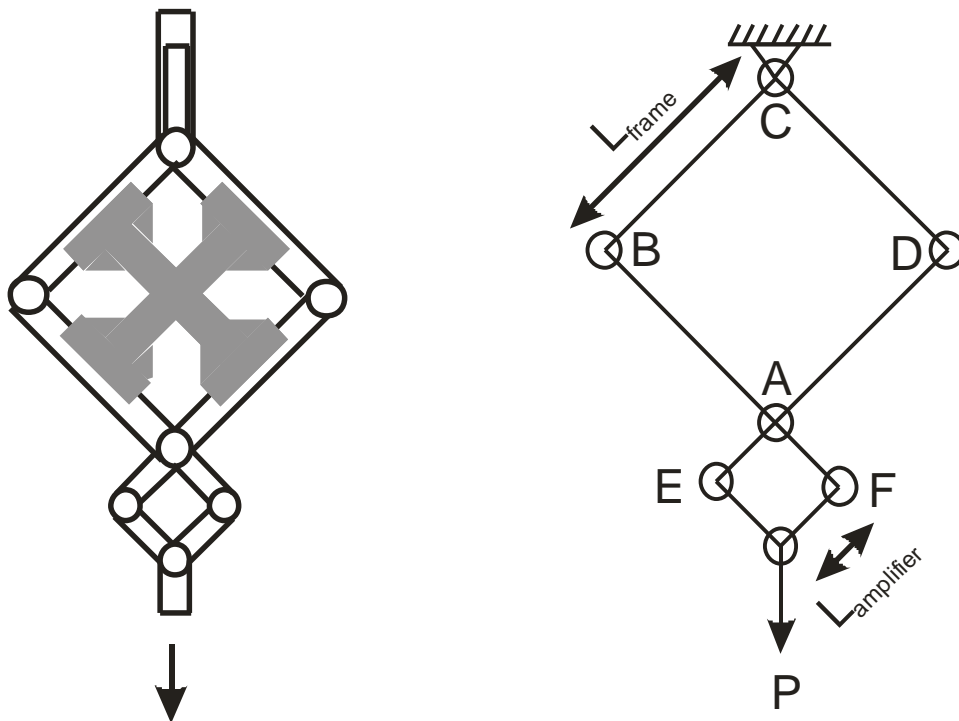


Figure 3.6 Schematics of picture frame tests

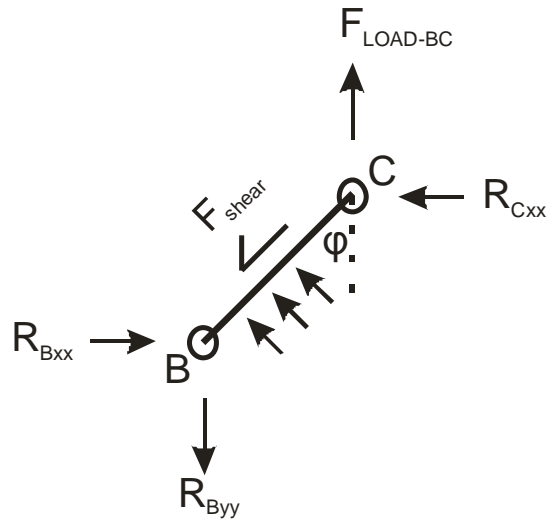


Figure 3.7 Free body diagram for link BC

The free body diagram of frame link BC is as shown in figure 3.7. All joints are free for motion. Using symmetry, it can be determined that the force applied on joint C from links CD and BC is equal and opposite in x-direction and equal and in same direction in y-direction [28][31].

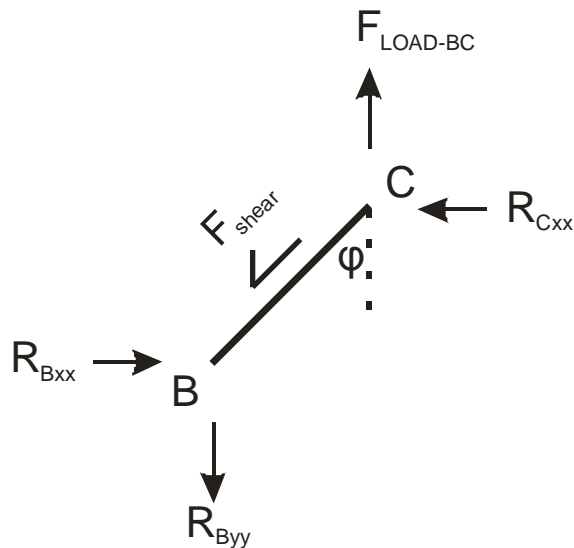


Figure 3.8 Simplified Free body diagram for link BC

In this study a simplified loading mechanism as shown in figure 3.8 has been assumed to find a direct relationship between the load recorded by the data acquisition system and shear force. Stress contours from image analysis or finite element modelling need to be used for actual mechanisms.

Using the free body diagram of link BC and performing static analysis for equilibrium in y direction, one gets:

$$F_{shear} = \frac{F_{Load-BC}}{\cos \varphi} \quad (3-1)$$

Reaction at B in y-direction, R_{Byy} has been assumed to be equal to zero because the joint B is free for motion as the resistance provided by empty frame was less than 1% of the results. Reaction at B in x-direction can be attributed to resistance to the compressive force from the samples. As $F_{Load-BC}$ and $F_{Load-CD}$ will be equal due to symmetry and their sum will be equal to the load recorded by the data acquisition system, shear force expression will be given as:

$$F_{shear} = \frac{F_{Load}}{2 \cos \varphi} \quad (3-2)$$

Shear stress, τ_{xy} can then be found by dividing shear force by the cross-sectional area of material with area parallel to the applied force vector which is the product of thickness and length of square.

3.3.2 Determination of Shear Angle

Initial configuration of the frame at the start of the test is as shown below. All the sides of frame are perpendicular to each other. Distance between top and bottom vertex is $L\sqrt{2}$.

Top is fixed to the load cell and bottom is pulled by the machine. Frame goes from a square configuration to rhomboid (diamond like) configuration.

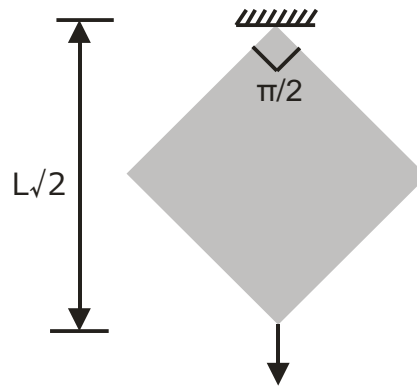


Figure 3.9 Initial configuration

Figure 3.10 below shows the configuration after a certain displacement of D and the distance between the top and bottom vertex is now $L\sqrt{2}+D$. The frame angle, ϕ which was initially $\pi/2$ has changed now. Frame angle can be related to shear angle, θ ($\alpha+\beta$) by

the relation $\theta = \frac{\pi}{2} - 2\phi$.

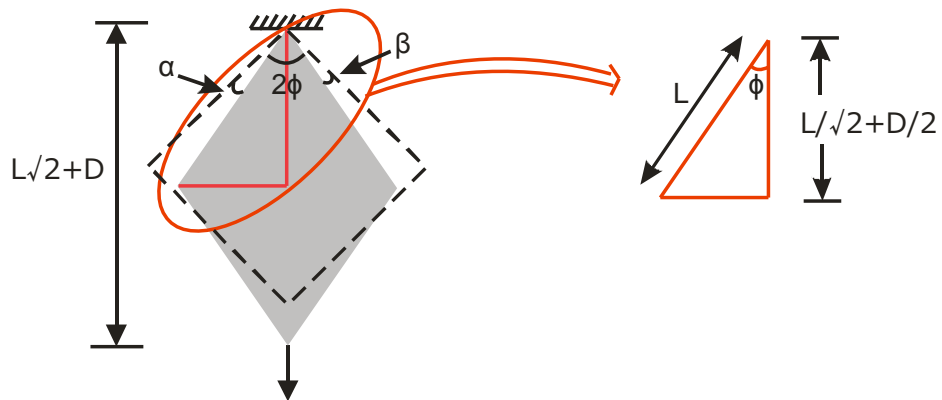


Figure 3.10 Configuration after a displacement of D units

Frame angle, ϕ after displacement D can be calculated from the figure 3.10 as:

$$\phi = \cos^{-1} \left[\frac{1}{\sqrt{2}} + \frac{D}{2L} \right] \quad (3-3)$$

The material shear angle can be calculated from the crosshead displacement using:

$$\theta = \frac{\pi}{2} - 2\phi = \frac{\pi}{2} - 2\cos^{-1}\left[\frac{1}{\sqrt{2}} + \frac{D}{2L}\right] \quad (3-4)$$

Where D is the crosshead displacement, L is the side length of the picture frame (i.e. distance between bearings) and Φ is the frame angle. It should be noted that the frame had an amplifier link, therefore the displacement of the sample D was a factor of the ratio of length of frame and length of amplifier link.

3.3.3 Determination of Shear Strain

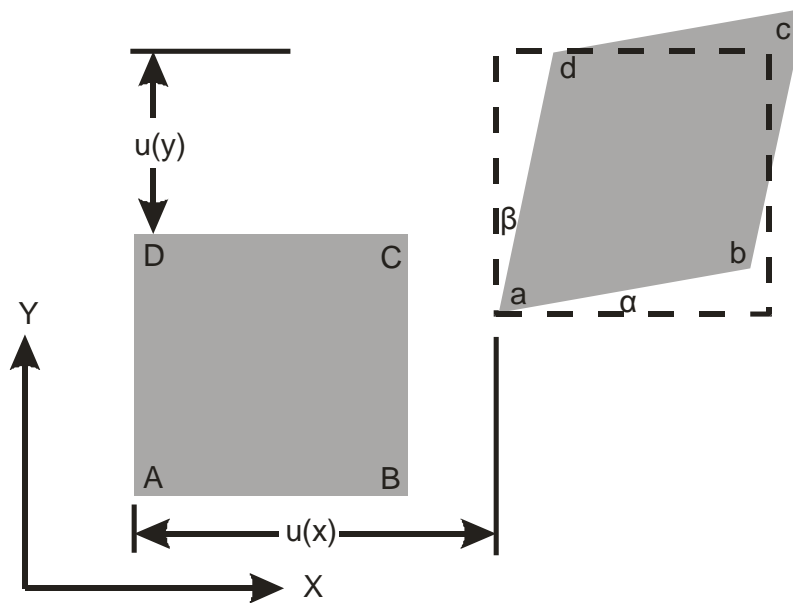


Figure 3.11 Theoretical shear strain

Engineering shear strain can be defined from figure 3.11 as the change in angle between the sides AB and AD. Therefore, the shear angle is same as the shear strain

$\gamma_{xy} = \frac{\partial u_y}{\partial x} + \frac{\partial u_x}{\partial y} = \alpha + \beta$. The shear strain is equal to shear angle and can be calculated

from the geometry of sample and displacement induced by actuator on the sample by the formula as-

$$\gamma_{xy} = \frac{\pi}{2} - 2\cos^{-1}\left[\frac{1}{\sqrt{2}} + \frac{D}{2L}\right] \quad (3-5)$$

It should be noted that this expression is only applicable for small displacements and small rotations as the approximations $\frac{\partial u_x}{\partial x} \ll 1$; $\frac{\partial u_y}{\partial y} \ll 1$ and $\alpha = \frac{\partial u_x}{\partial x}$; $\beta = \frac{\partial u_y}{\partial y}$ have been assumed. Also this approach assumes that the displacement, D of the actuator is the displacement of the sample, which is not true. Using three dimensional digital image correlation techniques, it will show the difference between the shear angle, which is the shear strain for small scale displacements and the shear strains as observed through image analysis. For this reason the shear strain calculated from the equation 3-4 has been referred as shear angle only throughout this thesis.

3.1 Digital Image Correlation (DIC) method

3.1.1 Introduction and applications

In the past decades, contacting deformation measurement techniques and devices including linear variable differential transformer (LVDT) and electrical-resistance strain gage were widely used in the field of experimental mechanics. However, both LVDT and strain gage only measure the displacement or strain at isolate locations that the deformation behavior of materials are not fully investigated [32]. Additionally, the experiments are limited by disadvantages of these methods including the effective working range, which results in varieties types of LVDT and strain gages; environments

such as the effect of temperature on strain gages; extra effort in experiment preparation like soldering, wiring and mounting; extra cost due to the disposable devices. Thus there is a demand on newer measurement techniques. Optical techniques such as moiré interferometry [33], holography [34] and speckle interferometry [35] have been proven to be matured techniques to analyze macroscopic parameters and are being applied successfully in many different applications. However, all the interferometric techniques have stringent requirements for system's stability. Moreover, the processing of fringe patterns is laborious and time-consuming [36]. This technical difficulty has raised many researchers' attention and computerized procedures [37] have been developed to automate the processing of the data from the fringe patterns.

In the thirty years, a non-contacting optical technique, digital image correlation, has been developed by Sutton et al. [38, 39, 40, 41] and Bruck, et al. [42]. As of recent years, DIC was widely applied to measurement of displacements and strains in many fields such as material science, mechanical engineering, biomechanics and structural engineering. The applications include strain measurements for anisotropic plastic deformation during tension testing [43], strain measurements in a CuAlBe shape memory alloy [44], analysis of glassy polymer networks under uniaxial compression test [45], determination of displacement distributions in bolted steel tension elements [46], deformation measurement of fiber composite pressure vessel [47]. Besides the applications on full-field deformation measurement, DIC has also been used for many other further purposes including the investigation of the bond between FRP and masonry [48], evaluation of kissing bond in composite adhesive lap joints [49], tracking fatigue damage evolution of

fiber reinforced composites [50], calibrating the constitutive models of steel beams subjected to local buckling [51], etc.

On the other hand, DIC technique can also be used together with other measurement method. For example, Rouchier et. al [52] conducted the damage monitoring in fibre reinforced mortar by combined DIC and acoustic emission; damage in CFRP composites was conducted by Goidescu et. al [53] using DIC, infrared thermography and X-ray tomography. He et. al [54] characterized the nonlinear shear properties for composite materials based on a combination of finite element method for stress calculation and DIC for measurement of deformation. The combination not only improved the accuracy of material properties but also provided an opportunity to extract material properties from experiments where the stress and strain fields are non-uniform and simple stress approximation is not feasible, reported by authors.

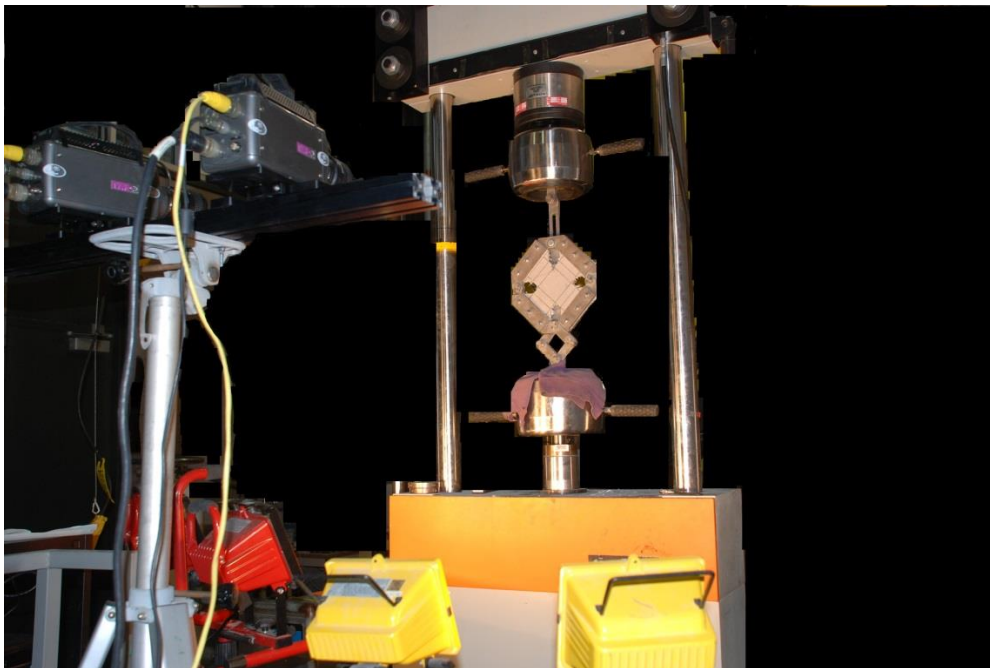


Figure 3.12 Setup of the 3D digital image correlation

3.1.2 DIC discipline

Digital image correlation is no exception, and algorithms are employed that take the physics of the underlying deformation processes into account [55]. Due to the miniscule motions that are often of interest in engineering applications, the resolution requirements are much higher than for most other applications. To accurately measure the stress-strain curve for many engineering materials, length changes on the order of 10^{-5} m/m have to be resolved. The algorithm developed by Sutton et al. [38, 39, 40, 41] targeted towards providing high resolution with minimal systematic errors. At the same time, a state-of-the-art phantom high camera mounted with high quality lens manufactured by Nikon was employed in the research.

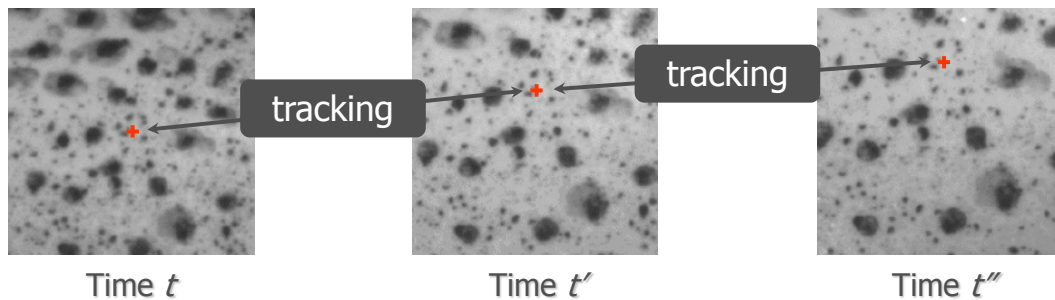


Figure 3.13 Tracking at different instances [56]

As shown in figure 3.13, a point on reference image is taken and then tracked over the set of images that were taken at sampling rate of 10 fps till the end of test. Deformation developed as the load increasing can be observed from the images taken after it starts, which is referred to as deformed images. As a result, the speckles at the surface of sample displace from their initial locations. These differences between speckle patterns can be calculated by correlating the pixels of the reference image and any deformed image.

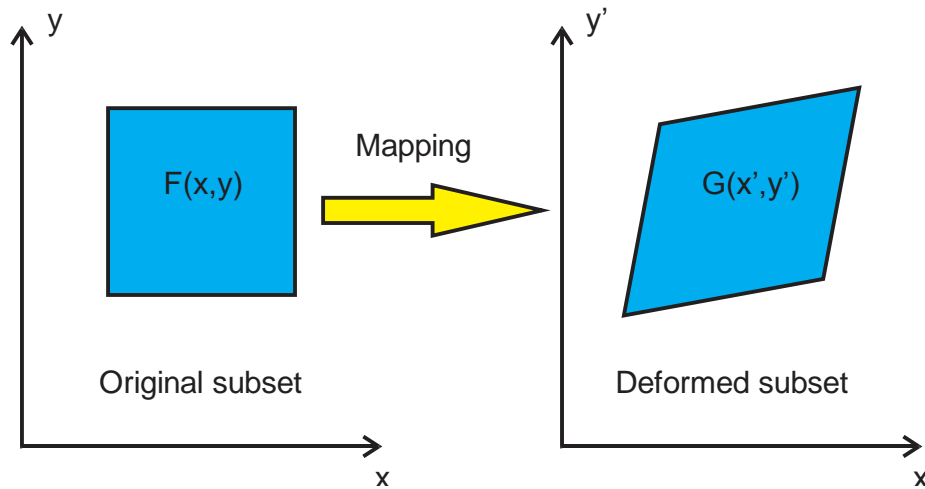


Figure 3.14 Mapping from original to deformed subset

However, it is not possible to establish the correspondence of a single pixel in terms of grey scale level from one image to another. In order to address the correspondence problem uniquely, the object surface texture should be isotropic and non-periodic, i.e., it should not have a preferred orientation or repeating textures. These requirements naturally led to the use of random textures, such as the speckle patterns shown in figure 3.15.

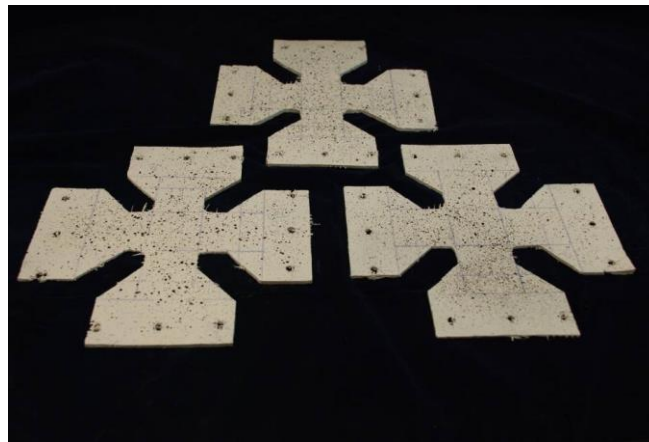


Figure 3.15 Speckled samples

The pattern used in DIC adheres to the surface and deforms with it and therefore no loss of correlation occurs even under large deformations. One of the key features of good

speckle patterns is their high information content. Since the entire surface is textured, information for pattern matching is available everywhere on the surface, and not only on a relatively sparse grid. This permits the use of a comparatively small aperture for pattern matching, referred to as a subset.

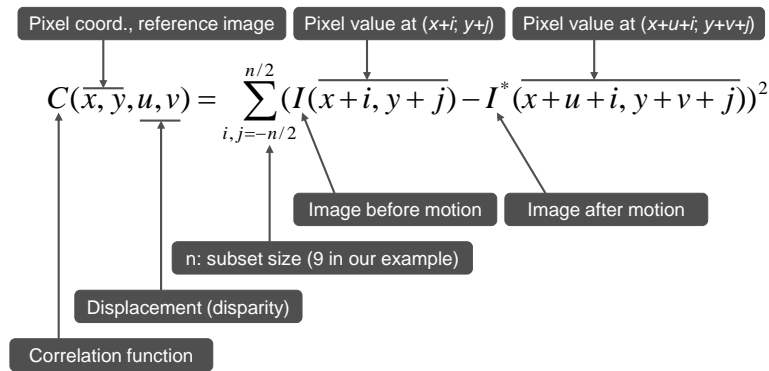


Figure 3.16 Terms involved in correlation [56]

The principle to measuring the displacement of subset is to match the subset in reference image with that in deformed image by means of a mapping function, based on the detection of grey level distribution. The grey level as a function of x and y of reference image $F(x,y)$ and that of a deformed image $G(x',y')$ are related by

$$G(x',y') = F(x,y+u(x,y)) \quad (3-6)$$

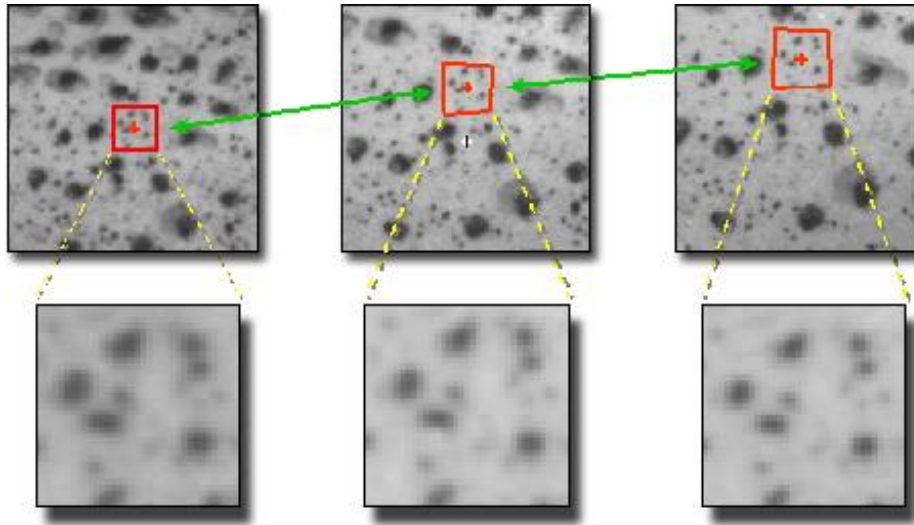


Figure 3.17 Correlation of a displaced surface [56]

Measurement of complex displacement fields is often an interest to engineering community; the specimen might experience elongation, compression, shear or rotation. An initially square reference subset might assume a distorted shape in a later image after deformation. This reduces the similarity between two subsets, which is often referred to as decorrelation. One of the significant advantages of DIC algorithm is that it is not only limited to determining pure translations but also can be easily extended to account for complex deformations. This is accomplished by introducing a subset shape function $\xi(\mathbf{x}, \mathbf{p})$ that transforms pixel coordinates in the reference subset in to coordinates in the image after deformation. The squared sum of differences (SSD) cost function [55] can be written as

$$\chi^2(\mathbf{p}) = \sum G(\xi(\mathbf{x}, \mathbf{p})) - F(\mathbf{x})^2 \quad (3-7)$$

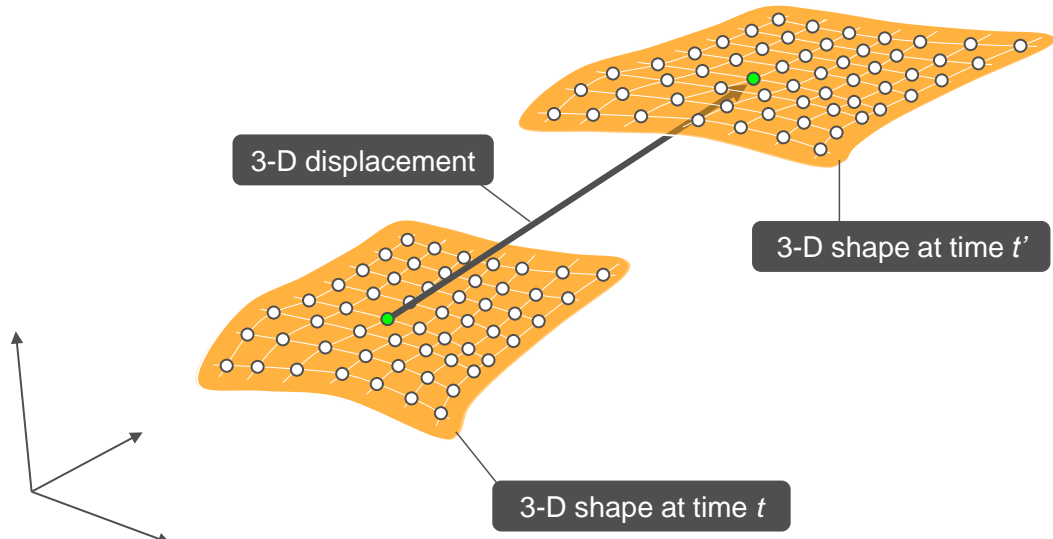


Figure 3.18 Displacement tracking in 3D fields [56]

The normalized cross-correlation criterion is bounded in the interval $[0,1]$, and attains its maximum for perfectly matching patterns. Besides the basic principle discussed in this part, the solution to issues like changes in lightening was also addressed and integrated. Furthermore, optimization in computational efficiency of the algorithm and reduction of errors were conducted [55].

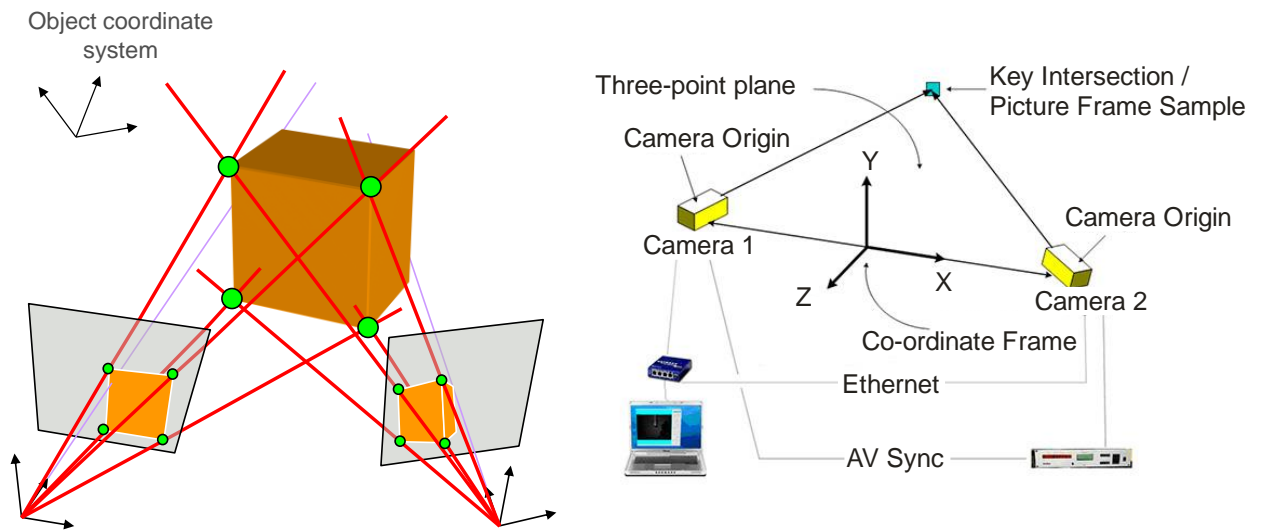


Figure 3.19 Schematics for 3D image analysis [56]

Even under near ideal experimental conditions, there will be differences between the intensity of images recorded at different times, for reasons such as changes in lighting, specimen reflectivity due to the strain or changes in the orientation of the specimen. Thus it is significant to develop matching algorithms that can accurately measure the correct correspondence between subsets even if the intensity values undergo significant changes. The way to conduct template matching is to minimize the squared gray value differences between the reference subset and the subset after motion. The squared sum of differences (SSD) is one of many optimization criteria that can be used for template matching, and indeed, gives the name of digital image correlation method.

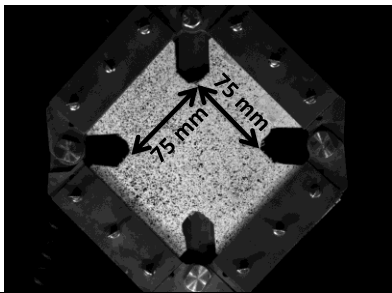
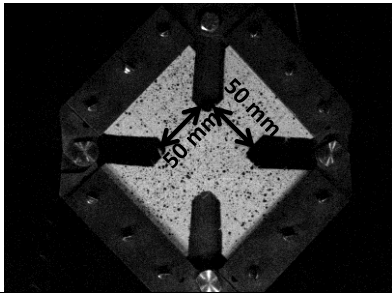
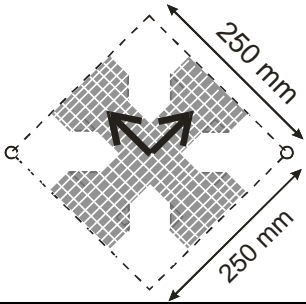
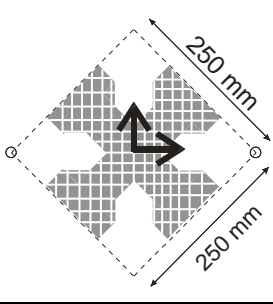
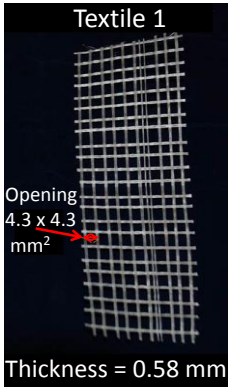
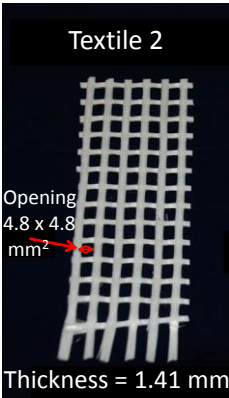
$$\chi^2_{NCC} = \frac{\sum FG}{\sum F^2 \sum G^2} \quad (3-8)$$

3.2 Experimental Parameters

Experimental tests were conducted to study the effects of thickness, planar cross-section, orientation of textiles and type of textile on the load bearing and shear strength of the composites. Thickness was taken at two levels, which are from here on referred to as T1 and T2. Thickness T1 corresponds to a thickness of 5.0 mm thick specimens with thickness of each layer of textile reinforced concrete as 2.5 mm whereas thickness T2 corresponds to a thickness of 6.5 mm thick specimens with thickness of each layer as 3.25 mm. Planar cross-section of inner-square was taken at two levels of S1 (75 mm x 75 mm) and S2 (50 mm x 50 mm). Two levels chosen for orientation were 0° and 45°. Orientation of 0° refers to textiles being orientated along the direction of shear force which is at 45° to the global axis of the testing machine whereas the orientation of 45°

refers to textile being oriented along the direction of tensile force which is at 0° to the global axis.

Table 3-2 : Parameters tested and their levels

| Parameters | Levels | |
|--------------------------------------|---|---|
| Planar cross-section of inner square | <p>75 mm x 75 mm (S1)</p>  | <p>50 mm x 50 mm (S2)</p>  |
| Orientation | <p>0°</p>  | <p>45°</p>  |
| Thickness | 5 mm (T1) | 6.5 mm (T2) |
| AR Glass Textile (Bonded Weave) | <p>Yarn thickness = 0.58 mm</p>  | <p>Yarn thickness = 1.41 mm</p>  |

Two different AR-Glass textiles were used to prepare the samples. Textiles consisted of perpendicular set of yarns (warp and weft) which were glued at the junction points and were manufactured by Nippon Electric Glass Co., Ltd. (NEG). Both the textiles had comparable material properties of tensile strength in range of 1270-2450 MPa and modulus of elasticity of 78 MPa. Volume fractions of reinforcement when two layered textile 1 was used at 5.0 mm thickness was 4.31% and at 6.5 mm was 5.63% whereas for textile 2 at 6.5 mm thickness was 14.82%. Tables 3-2 shows the four parameters tested in this study and their two levels. Table 3-3 shows the combinations used to understand the effect of the chosen parameters.

Table 3-3 : Test combinations used in the experiment

| Test Combination | | | | | | |
|-------------------------|----------------|---------------|-------------------------------|-------------|---|--------|
| | No. of samples | Thickness, mm | Planar cross-section, mm x mm | Orientation | Textile AR Glass (Bonded weave) Thickness, mm | Age |
| # 1 | 5 | 5 | 75 x 75 | 0° | 0.58 | 7 days |
| # 2 | 5 | 5 | 50 x 50 | 0° | 0.58 | 7 days |
| # 3 | 5 | 6.5 | 75 x 75 | 0° | 0.58 | 7 days |
| # 4 | 5 | 5 | 75 x 75 | 45° | 0.58 | 7 days |
| # 5 | 5 | 6.5 | 75 x 75 | 45° | 0.58 | 7 days |
| # 6 | 5 | 6.5 | 75 x 75 | 0° | 1.41 | 7 days |

3.3 Analysis of Test Data

This section discusses the MATLAB program specially developed to analyze the test data and calculate some useful properties. The idea behind developing this code was to process the raw data through necessary modifications, smoothening and filtering of the response to reduce the noise in the data, characteristic of such tests. The code was developed in several parts. First section deals with input parameters, which include physical specifications of test specimens. Next, the test data is converted to international unit (SI) of measurement, and the first row of time, load, acceleration and deflection responses is modified to start from zero. Each of these modified responses was further smoothened to reduce their inherent noise. Modified test data was then printed onto a separate file. Properties such as shear angle (in degrees and radians), shear force, shear strength, first cracking strain, toughness and stiffness were then calculated and saved onto a separate output file.

3.4 Test Results

Samples were tested at different inner square planar cross-sections of 75 mm x 75 mm (S1) and 50 mm x 50 mm (S2), different thickness of 5 mm (T1) and 6.5 mm (T2), and different textile orientation of 0° and 45° and with different textiles.

S1-T1- 0° (75 mm x 75 mm, Thickness = 5.0 mm, 0°)

Figure 3.20 shows the load-displacement response for the S1 – T1 - 0° samples. It can be seen that the stiffness and the displacement corresponding to the first crack in consistent for all samples.

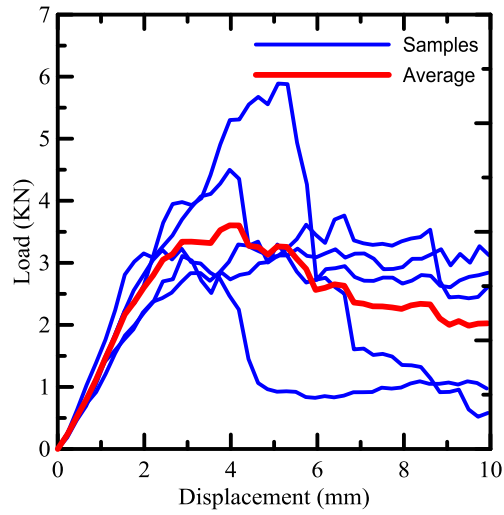


Figure 3.20 Load-deflection response for S1-T1- 0°

Displacement corresponding to first crack for all the samples lies in the range of 2.5 to 4 mm. Average stiffness is 1.105 KN/mm. Peak load varies from 2.8 KN to 5.9 KN with the average at 3.4 KN.

S2 – T1 - 0° (50mm x 50mm, Thickness=5 mm, 0°)

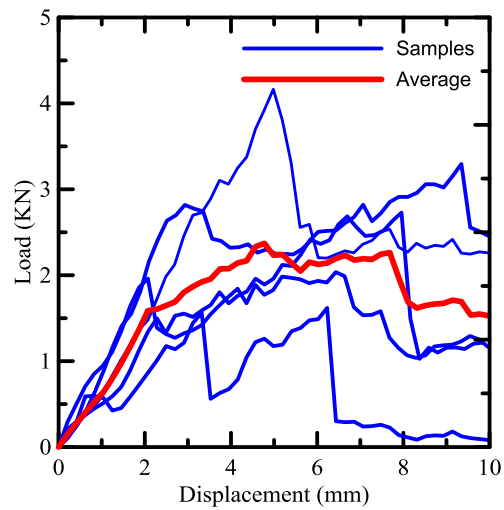


Figure 3.21 Load-deflection response for S2-T1- 0°

Figure 3.21 shows the load-displacement response for the S2 – T1 - 0° samples. Displacement corresponding to first crack for all the samples lies in the range of 2.5 to 4 mm. Average stiffness is 0.466 KN/mm. Peak load varies from 1.6 KN to 4.1 KN with the average at 2.2 KN which means 44% decrease happens when the cross-section is reduced from 75 mm square to 50 mm square.

S1 – T1-45° (75mm x 75mm, Thickness=5.0 mm, 45°)

Figure 3.22 shows the load-displacement response for the S1 – T1 - 45° samples. Displacement corresponding to first crack for all the samples lies in the range of 2.75 to 5 mm. Average stiffness is 1.210 KN/mm. Peak load varies from 2.3 KN to 8.6 KN with the average at 4.4 KN which means 23% increase happens compared to S1-T1-0° when the orientation is changed from 0° to 45° while all other parameters hold same.

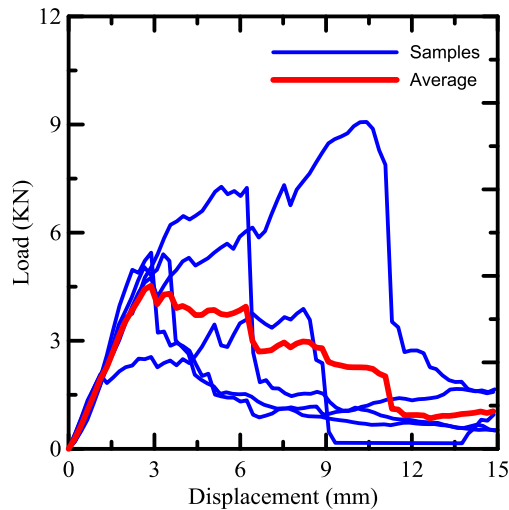


Figure 3.22 Load-deflection response for S1-T1- 45°

S1 – T2 -0° (75 mm x 75 mm, Thickness = 6.5 mm, 0°)

Figure 3.23 shows the load-displacement response for the S1 – T2 - 0° samples. Displacement corresponding to first crack for all the samples lies in the range of 2.1 to 3 mm. Average stiffness is 1.260 KN/mm. Peak load varies from 3.1 KN to 6.2 KN with the average at 3.8 KN which means 12% increase happens when the thickness is changed from 5.0 mm to 6.5 mm.

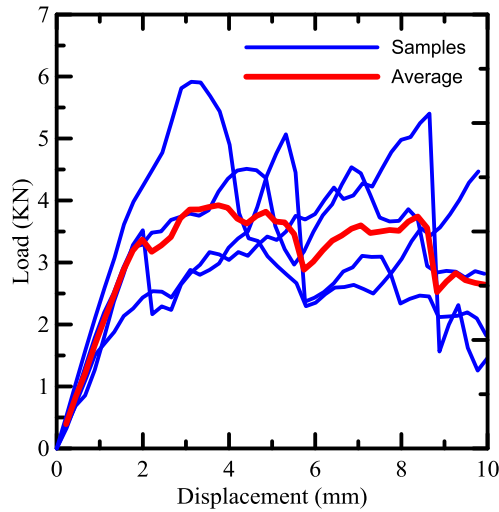


Figure 3.23 Load-deflection response for S1-T2- 0°

S1 – T2 - 45° (75mm x 75mm, Thickness=6.5mm, 45°)

Figure 3.24 shows the load-displacement response for the S1 – T2 - 45° samples. Displacement corresponding to first crack for all the sample lies in the range of 2.8 to 4.1 mm. Average stiffness is 0.861 KN/mm.

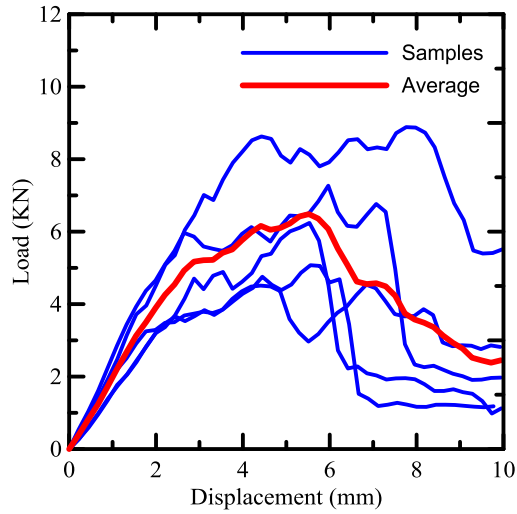


Figure 3.24 Load-deflection response for S1-T2- 45°

Peak load varies from 4.8 KN to 8.1 KN with the average at 6.8 KN which means 44% increase happens when the orientation is changed from 0° to 45° and 35% increase happens when thickness is changed from 5.0 mm to 6.5 mm.

Textile 2 – S1 – T2 - 0° (Textile 2 75 mm x 75 mm, Thickness=6.5mm, 0°)

Figure 3.25 shows the load-displacement response for the textile 2 - S1 – T2 - 0° samples. Displacement corresponding to first crack for all the samples lies in the range of 2.6 to 3.1 mm. Average stiffness is 1.488 KN/mm. Peak load varies from 4.8 KN to 8.1 KN with the average at 5.7 KN which means 33% increase happens when the textile 2 used in place of textile 1.

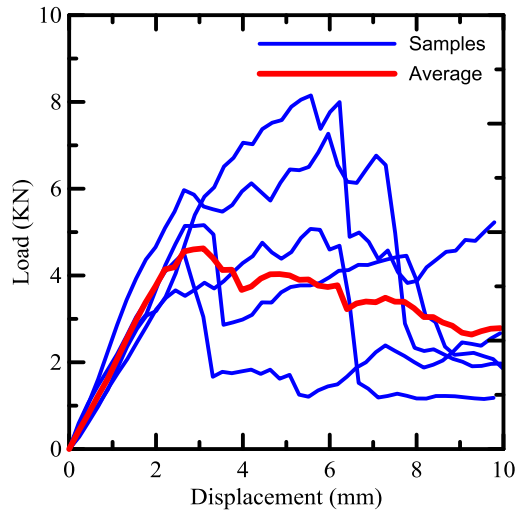


Figure 3.25 Load-deflection response for Textile 2 - S1-T2- 0°

3.5 Discussion of Experimental Results

Figure 3.20 and 3.21 shows two sets of experiments at equal thickness, same orientation and textile but with different inner square cross-section. From load versus displacement response for these two sets it was observed that bigger samples have better load bearing capacity. Displacement corresponding to first crack is very much consistent for S1 at around 3 mm whereas for S2 it is varying from 2.5 mm to 4 mm with the average around 2.8 mm only. From figures 3.20 and 3.22 it was observed the effect of orientation on load bearing capacity. The capacity increases as the textiles are stronger in tension as compared to shear. Similarly same pattern in figures 3.23 and 3.24 can be seen when compared at different orientations and constant thickness of T2. From comparisons of figures 3.20 with 3.23 and 3.22 with 3.24, effect of thickness was observed. From figures 3.23 and 3.25, effect of textiles was observed. The load bearing capacity increases as the

surface area increases with textile 2. This is because with more surface area one gets better bonding between the paste and the textile giving better matrix properties.

Table 3-4 : Summary of test results

| | S1 – T1 - 0° | S2 – T1 - 0° | S1 – T2 - 0° | S1 – T1 - 45° | S1 – T2 - 45° | Textile 2 -S1 – T2 - 0° |
|---|--------------|--------------|--------------|---------------|---------------|-------------------------------|
| Shear Strength (MPa) | 2.284 | 2.292 | 1.918 | 2.602 | 2.542 | 2.355 |
| Energy under τ - γ curve (MPa) | 0.475 | 0.461 | 0.462 | 0.497 | 0.500 | 0.550 |
| Stiffness (KN/mm) | 1.105 | 0.466 | 1.260 | 1.210 | 0.861 | 1.448 |
| First Cracking Strain (radians) | 0.080 | 0.065 | 0.095 | 0.075 | 0.080 | 0.075 |

3.6 Effect of Thickness

Figure 3.26 shows the comparison between 5.0 mm (T1) and 6.5 mm (T2) thick samples at 0° and 45° orientations. Planar cross-section of sample was constant at 75 mm x 75 mm (S1) and textile 1 was used to manufacture all the specimens. From figure 3.23 it was observed that the load bearing had increased with increase in thickness but its effect on shear strength is small as shear strength is normalized by the thickness.

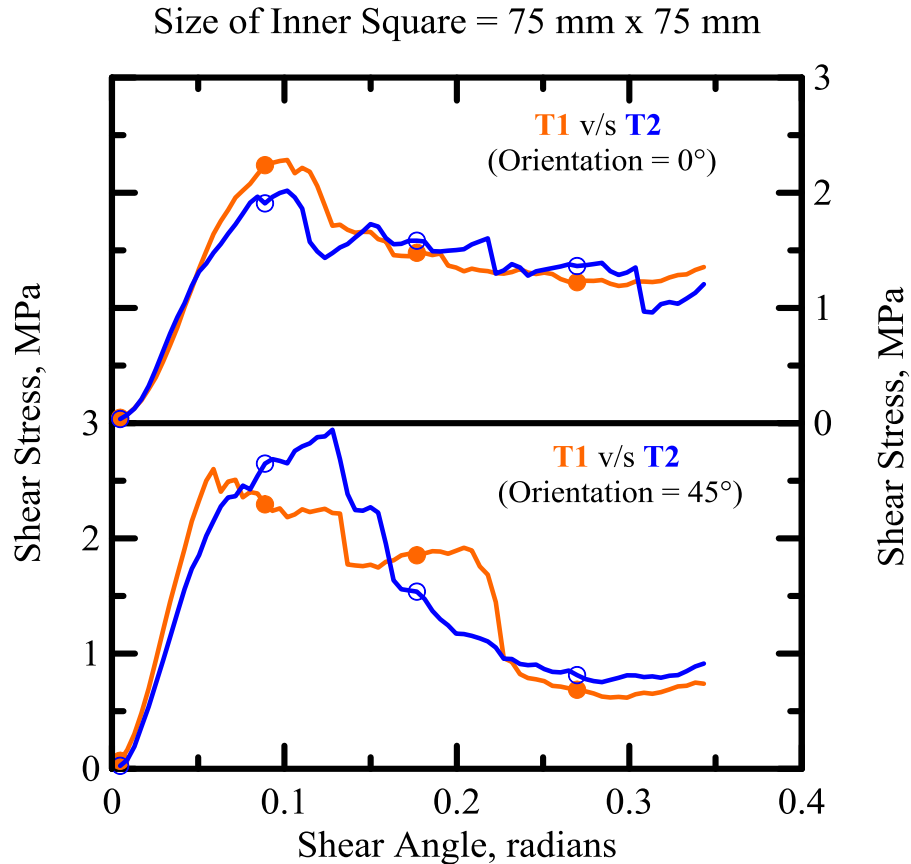


Figure 3.26 Shear stress versus shear angle response for comparison between the two thicknesses - T1 (5.00 mm) and T2 (6.5 mm) for both the orientations

A drop of 19% in shear strength can be seen when the textiles are orientated at 0° and an increase of 14% in shear strength when textiles are orientated at 45° . Also a drop of 2.8% can be seen in energy under the shear stress and shear angle for 0° textile orientation and increase of 0.6% for 45° textile orientation.

3.7 Effect of Orientation

Figure 3.27 shows the details of the orientations 0° and 45° at before and after cutting. It can be seen that yarns of 0° orientation is actually at 45° to the direction of force whereas 45° is along and perpendicular to the direction of applied force. Figure 3.28 shows the

results for 0° and 45° for 5.0 mm and 6.5 mm thick specimens. Textile 1 was used in manufacturing the specimens at both the orientations.

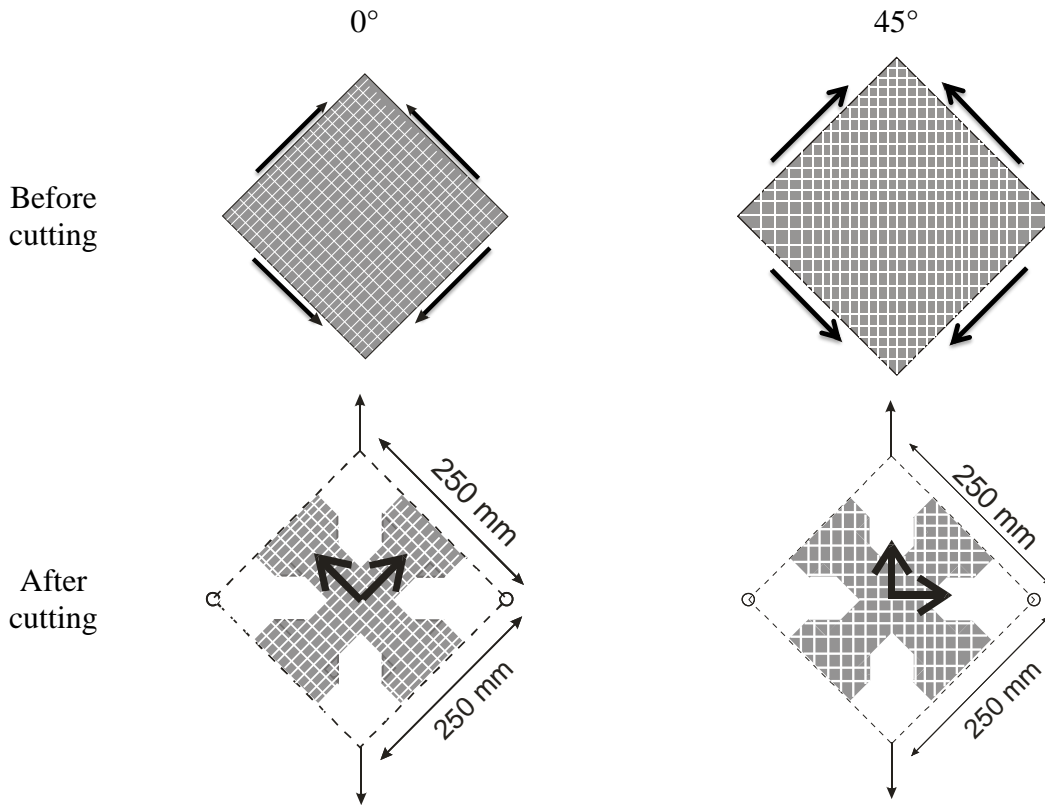


Figure 3.27 Orientations before and after cutting

From figure 3.28 it was observed that the strength increases when textiles are orientated at 45° when compared to orientation at 0° . When the textile is orientated at 45° , it is controlled by tensile action rather than the shear. Increase in strength can be therefore be explained by the previous knowledge of textile reinforced concrete being stronger under tensile force when warps and wefts are along and perpendicular to the direction of load when compared with shear force [57]. Under tensile regime (45°), the load is applied along the direction of longitudinal fibers which takes advantage of the fiber mechanical properties. Additionally, after the matrix cracks, textile bridging the cracks directly takes the tensile load and the modes of failure are dominated by fiber pullout or fracture, which

results in high strength and energy absorption capability. While on the other hand, textile arranged along 0° is not subjected to direct tension, indicating a complicated interaction process between fiber and matrix.

The increase in shear strength of textile reinforced concrete with textiles at 45° is 14% at thickness of 5.0 mm and 33% at thickness of 6.5 mm. Increase at higher thickness is more because with textile orientation at 45° , paste is more vulnerable to failure and therefore increase in thickness due to application of additional paste for each layer of textile improves the strength.

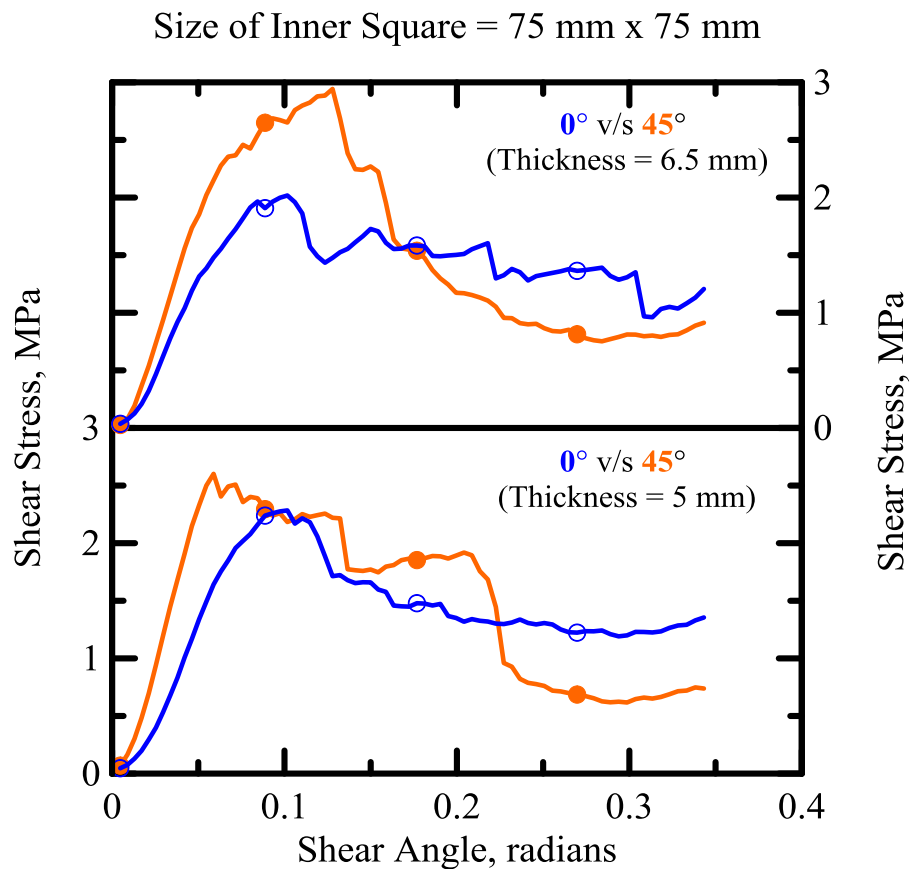


Figure 3.28 Shear stress versus shear angle response for comparison between the two orientations- 0° and 45° for both the thicknesses

3.8 Effect of Planar Cross-Section

Two planar cross-sections of 75 mm x 75 mm (S1) and 50 mm x 50 mm (S2) were tested to study the effects of cross-section. Figure 3.29 shows the samples at each level and figure 3.30 shows the dimensional details of these two levels. Figure 3.31 shows the comparison between 75 mm x 75 mm (S1) and 50 mm x 50 mm (S2). Orientation and thickness were kept constant at 0° and 5.0 mm. Textile 1 was used to manufacture all the specimens in the study of planar cross-sectional effects.

Inner square c/s - 75 mm x 75 mm (S1)

Inner square c/s - 50 mm x 50 mm (S2)

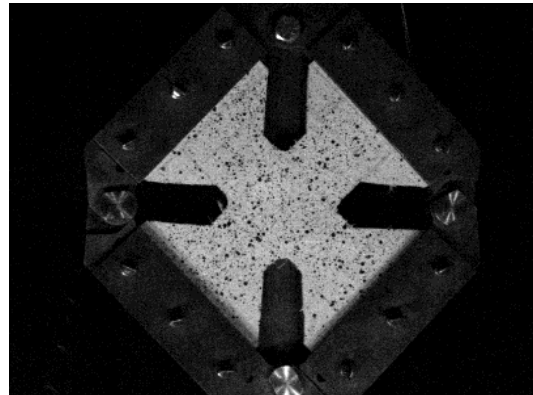
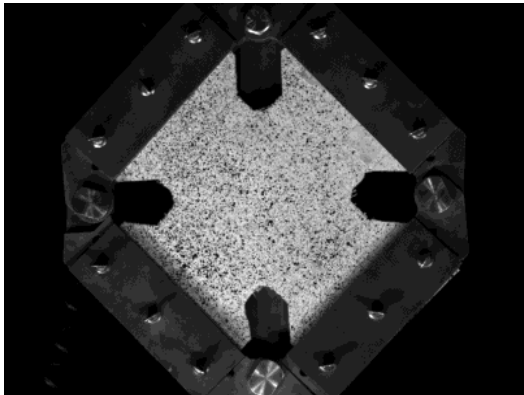


Figure 3.29 Pictures of different sample cross-sections

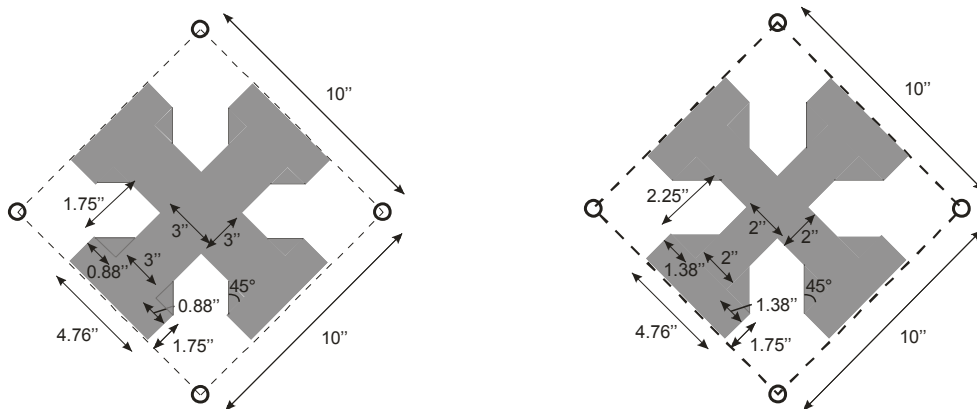


Figure 3.30 Dimensions of the two sample cross-sections

From figure 3.31 it was observed that the shear stress versus strain response is similar at both the cross-section whereas there was an increase in load bearing capacity as observed in figure 3.20.

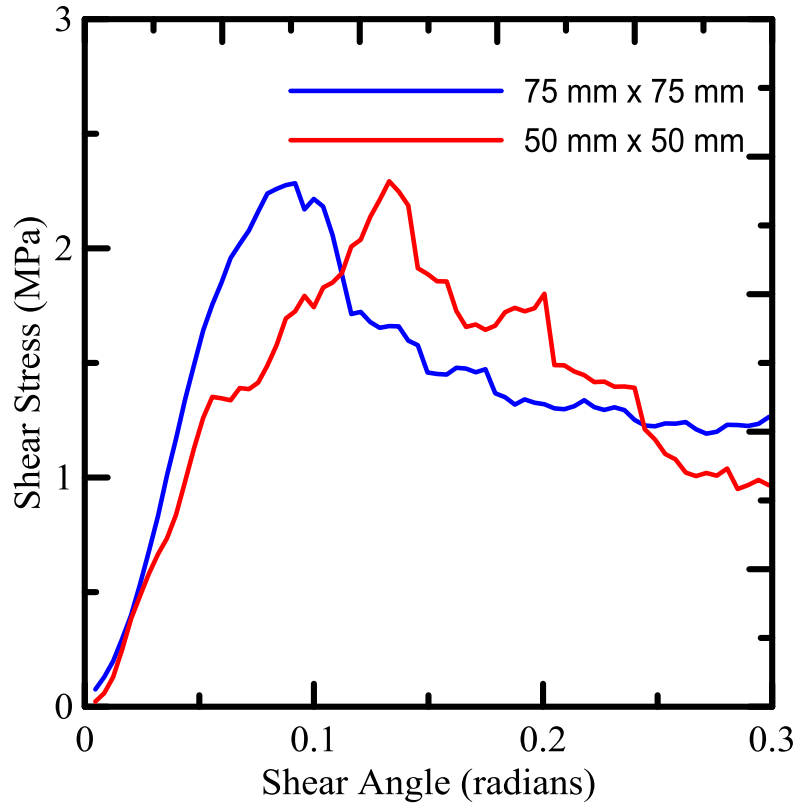


Figure 3.31 Shear stress versus shear angle response for S1 and S2

There is no change in shear strength because the shear stress is a material property and therefore the effect of dimensions is not there. Difference in the shear strength between the two cross-sections is of 0.35% which can be neglected.

3.9 Effect of Textile Type

Two different AR-Glass textiles were used in this study. They had different yarn thicknesses of 0.58 mm and 1.41 mm. Textile shown on right in figure 3.32 with

thickness 0.58 mm is referred as textile 1 whereas textile on right with thickness of 1.41 mm is referred as textile 2.

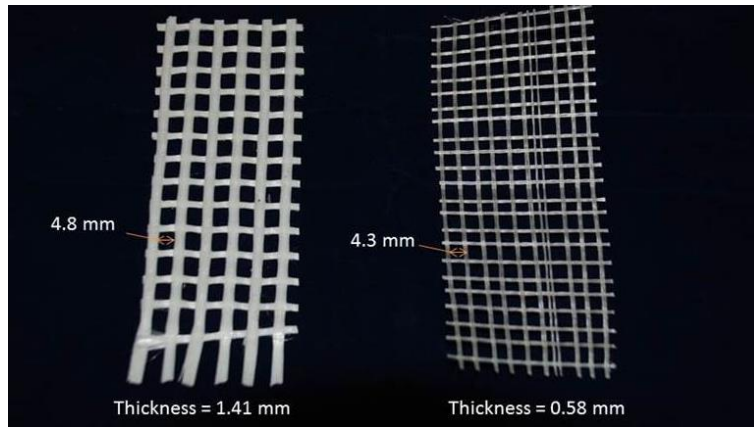


Figure 3.32 Two textiles used in this study

From figure 3.33 it was observed that the shear strength for textile 2 increases by 12%. This increase is due to the fact that the area of contact is more in textile 2 providing better bonding.

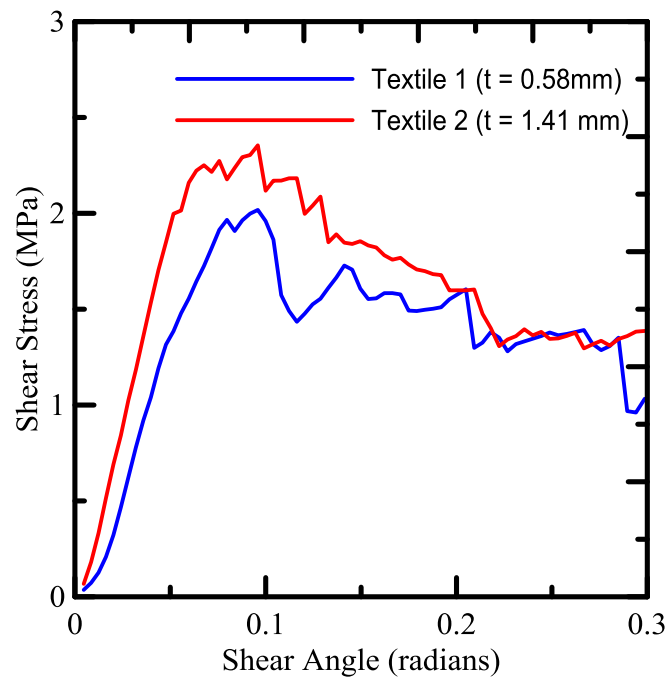


Figure 3.33 Shear stress versus shear angle response for textile 1 vs textile 2

This proves that the strength of matrix is a function of area of contact. This reinstates the benefit of using textile reinforced concrete over conventional steel reinforcement as the area of contact between paste and reinforcement in case of textile reinforced concrete is higher when compared to steel reinforcement.

3.10 Conclusion of Results

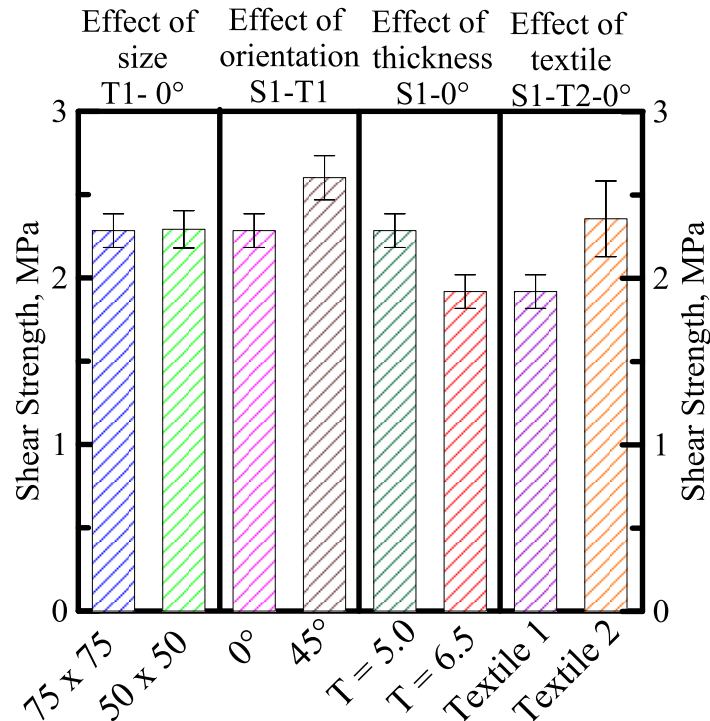


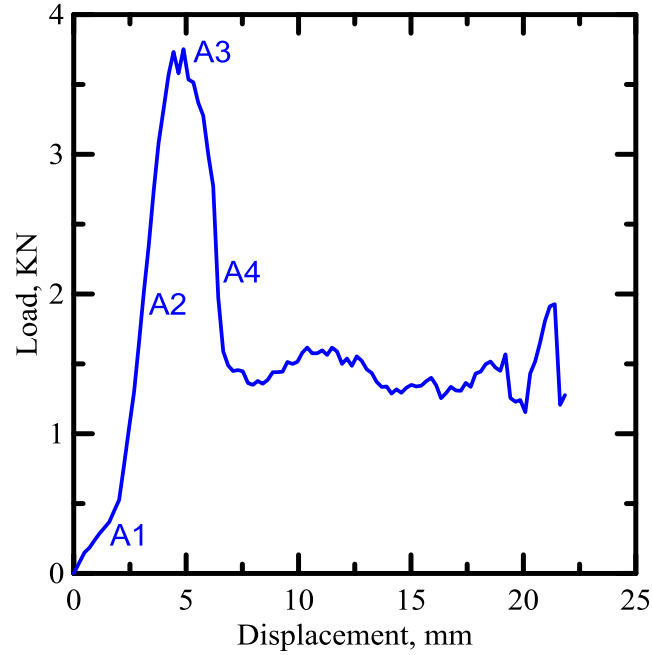
Figure 3.34 Shear strength summary

In figure 3.34 for summary of shear strengths, the effect of the four parameters used in this study can be compared. As shear strength is a material property, therefore it is expected that cross-section and thickness should not affect it. It was observed that the cross-section has a very negligible effect on shear strength as expected whereas it decreases with increase in thickness. This decrease is due to the fact that bonding of additional paste is not as good as the rest of the matrix and causes failure due to spalling

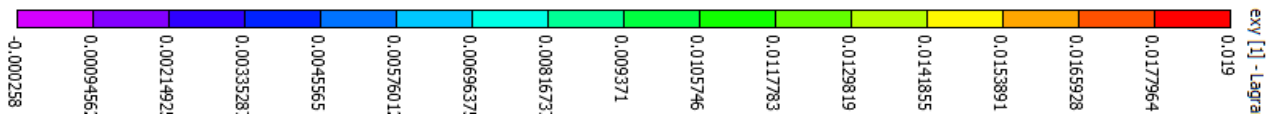
of the exterior cement layers. Shear strength increases at 45° orientation as textile is oriented along and perpendicular to the loading of direction and tensile strength is more dominant in that case instead of shear strength. Shear strength increases for textile 2 as it has more surface area and bigger openings and therefore better bonding and paste penetration takes place in those samples.

3.11 Digital Image Correlation Results

Set 1 - S1 - T1 - 0° (75 mm x 75 mm, Thickness = 5 mm, 0°, Textile 1 - AR Glass thk 0.58 mm)

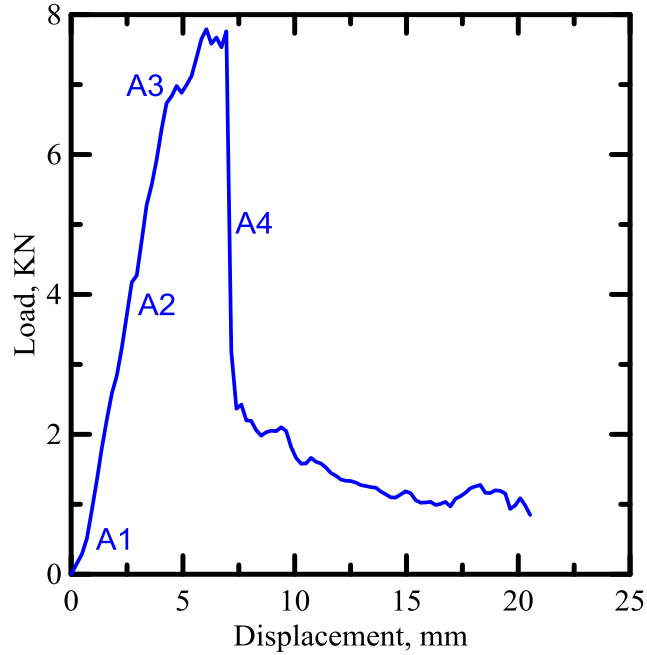


| A1 | | A2 | | A3 | | A4 | |
|-------------------|---------------------|-------------------|-----------------------|-------------------|-----------------------|-------------------|-----------------------|
| | | | | | | | |
| T = 0 sec | P = 0 KN | T = 50 sec | P = 2.1 KN | T = 75 sec | P = 3.7 KN | T = 100 sec | P = 2.3 KN |
| $\delta = 0.0$ mm | $\tau_{xy} = 0$ MPa | $\delta = 3.8$ mm | $\tau_{xy} = 1.1$ MPa | $\delta = 5.1$ mm | $\tau_{xy} = 2.1$ MPa | $\delta = 7.2$ mm | $\tau_{xy} = 1.2$ MPa |

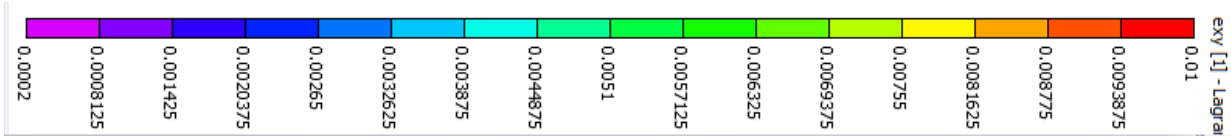


Set 2 – S1 – T1 - 45° (75 mm x 75 mm, Thickness = 5 mm, 45° Textile 1 - AR Glass thk 0.58

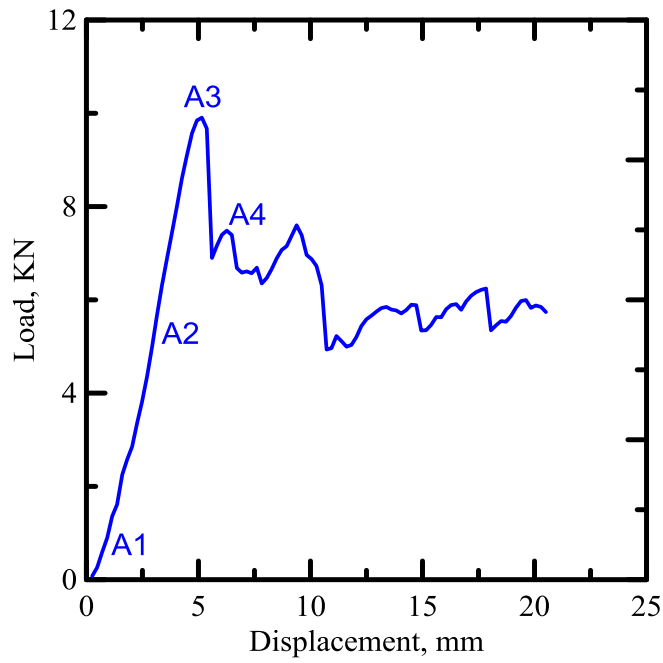
mm)



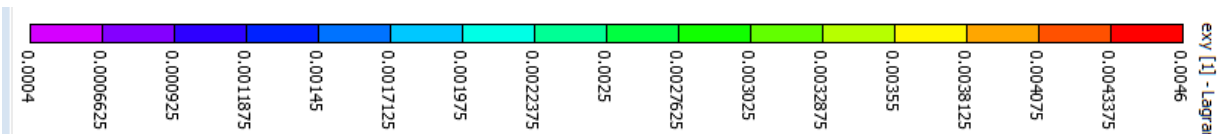
| A1 | | A2 | | A3 | | A4 | |
|-------------------|---------------------|-------------------|-----------------------|-------------------|-----------------------|-------------------|-----------------------|
| | | | | | | | |
| T = 0 sec | P = 0 KN | T = 25 sec | P = 3.9 KN | T = 50 sec | P = 6.8 KN | T = 75 sec | P = 5.2 KN |
| $\delta = 0.0$ mm | $\tau_{xy} = 0$ MPa | $\delta = 3.2$ mm | $\tau_{xy} = 2.2$ MPa | $\delta = 5.3$ mm | $\tau_{xy} = 3.7$ MPa | $\delta = 7.2$ mm | $\tau_{xy} = 2.4$ MPa |



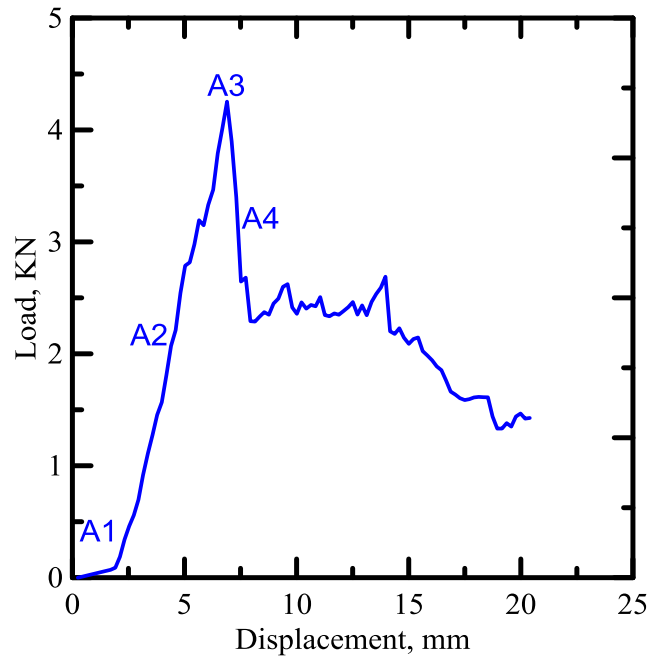
Set 3 – S1 – T2 - 0° (75 mm x 75 mm, Thickness = 6.5 mm, 0°, Textile 2 AR Glass thk 1.41 mm)



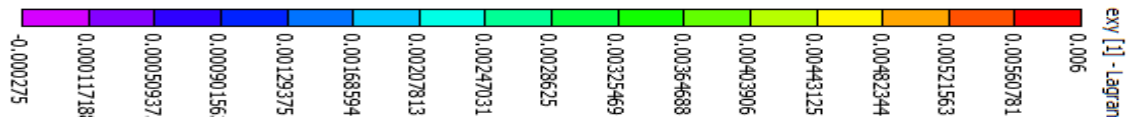
| A1 | | A2 | | A3 | | A4 | |
|-------------------|---------------------|-------------------|-----------------------|-------------------|-----------------------|-------------------|-----------------------|
| | | | | | | | |
| T = 0 sec | P = 0 KN | T = 25 sec | P = 5.6 KN | T = 50 sec | P = 9.8 KN | T = 75 sec | P = 7.6 KN |
| $\delta = 0.0$ mm | $\tau_{xy} = 0$ MPa | $\delta = 3.8$ mm | $\tau_{xy} = 2.2$ MPa | $\delta = 5.2$ mm | $\tau_{xy} = 4.1$ MPa | $\delta = 6.2$ mm | $\tau_{xy} = 3.2$ MPa |



Set 4 – S2 – T1 - 0° (50 mm x 50 mm, Thickness = 5 mm, 0°, Textile 1 - AR Glass thk 0.58 mm)



| A1 | | A2 | | A3 | | A4 | |
|-------------------|---------------------|-------------------|-----------------------|-------------------|-----------------------|-------------------|-----------------------|
| | | | | | | | |
| T = 0 sec | P = 0 KN | T = 25 sec | P = 2.2 KN | T = 50 sec | P = 4.3 KN | T = 75 sec | P = 3.3 KN |
| $\delta = 0.0$ mm | $\tau_{xy} = 0$ MPa | $\delta = 4.8$ mm | $\tau_{xy} = 1.8$ MPa | $\delta = 7.2$ mm | $\tau_{xy} = 3.4$ MPa | $\delta = 7.4$ mm | $\tau_{xy} = 2.3$ MPa |



3.12 Discussion of Digital Image Correlation results

Set 1 - 75 mm x 75 mm, Thk = 5 mm, 0° Textile 1 (AR Glass thk 0.58 mm) - From the 2-D spectrum for shear strain at 50 seconds and 75 seconds it was seen that the first crack initiates from the lower right side edge after a deflection of 5.1 mm. Testing machine gives a value of 2.1 MPa for shear stress and 3.7 KN for the load corresponding to the first crack initiation. Spectrum has been limited to 100 seconds as all the composite material mechanics takes place during this region. Maximum shear strain was 0.019 mm/mm.

Set 2 – 75 mm x 75 mm, Thk = 5 mm, 45° Textile 1 (AR Glass thk 0.58 mm) - From the 2-D spectrum for shear strain at 25 seconds and 50 seconds one can see that the first deformation takes place around the top right edge after a displacement of 5.3 mm. Testing machine gives a value of 3.7 MPa for shear stress and 6.8 KN for the load corresponding to the first crack initiation. But as the textile is oriented at 45°, that is along and perpendicular to the direction of loading, tensile properties govern in place of shear. As textile reinforced concrete is very strong in tension, compressive buckling takes places around the center. Spectrum has been limited to 75 seconds as all the composite material mechanics takes place during this region. Maximum shear strain was 0.01 mm/mm.

Set 3 - 75 mm x 75 mm, Thk = 6.5 mm, 0° , Textile 2 (AR Glass thk 1.41 mm) - From the 2-D spectrum for shear strain at 50 seconds and 75 seconds it can be seen that the crack initiation takes place around the bottom right edge after a displacement of 5.2 mm.

Testing machine gives a value of 4.1 MPa for shear stress and 9.8 KN for the load corresponding to the first crack initiation. It was seen that the shear stress and load values corresponding to first crack are higher for this case when compared with set-1. This is because the bonding is better in this case as textile two has higher surface area. Spectrum has been limited to 75 seconds as all the composite material mechanics takes place during this region. Maximum shear strain was 0.0046 mm/mm.

Set 4 – 50 mm x 50 mm, Thickness = 5 mm, O° - From the 2-D spectrum for shear strain at 50 seconds and 75 seconds it can be seen that the crack initiation takes place around the bottom right edge after a displacement of 7.2 mm. Testing machine gives a value of 3.4 MPa for shear stress and 4.3 KN for the load corresponding to the first crack initiation. Spectrum has been limited to 75 seconds as all the composite material mechanics takes place during this region. Maximum shear strain was 0.006 mm/mm.

3.13 Relationship between Shear Angle and Shear Strain

In section 3.3.3, it had discussed that the approximation of small scale displacements and rotation had been assumed to consider shear angle to be equal to shear strain. To calculate the actual strains, digital image correlation technique was used. Comparing the two results one can observe that initially shear angle over estimates the shear strain. This is because all the internal mechanics cannot be recorded by DIC system and therefore till the first crack there is no major displacement for the image analysis system to capture and analyze for strain calculations. After cracking it can be seen that high values for shear strains are recorded by DIC system.

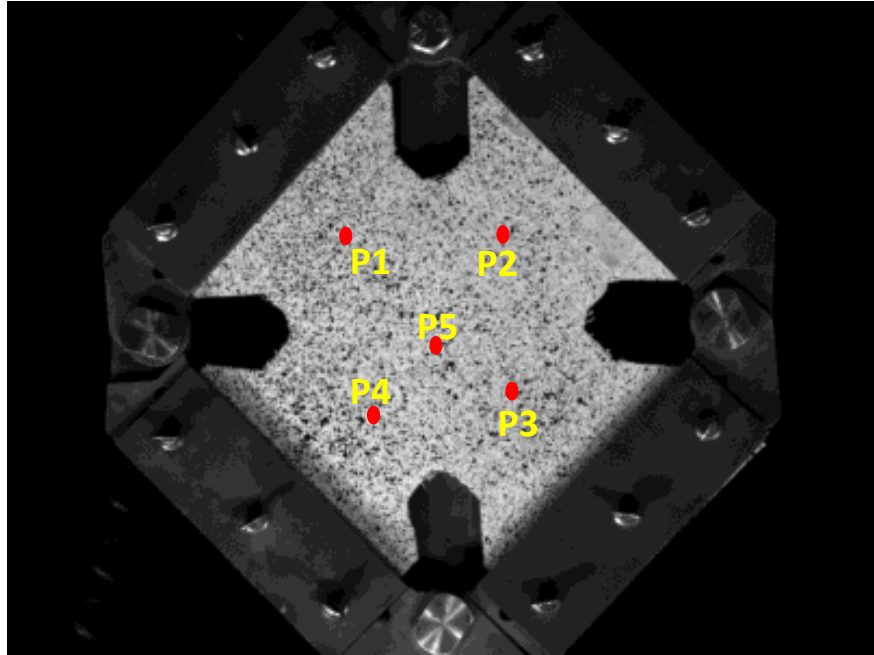


Figure 3.35 Shear strain from DIC versus shear angle

Figure 3.35 shows the five points at which the shear strain was studied. Governing shear strain was found out to be at the point where cracking took place as the magnitude was maximum at that point compared to remaining four points and overall average shear strain.

In figure 3.36, sample 1 is 75 mm x 75 mm sample with thickness of 5 mm and textiles oriented at 0° and sample 2 is 50 mm x 50 mm sample with thickness of 6.5 mm and textiles orientated at 0° . Textile 1 was used in both the samples.

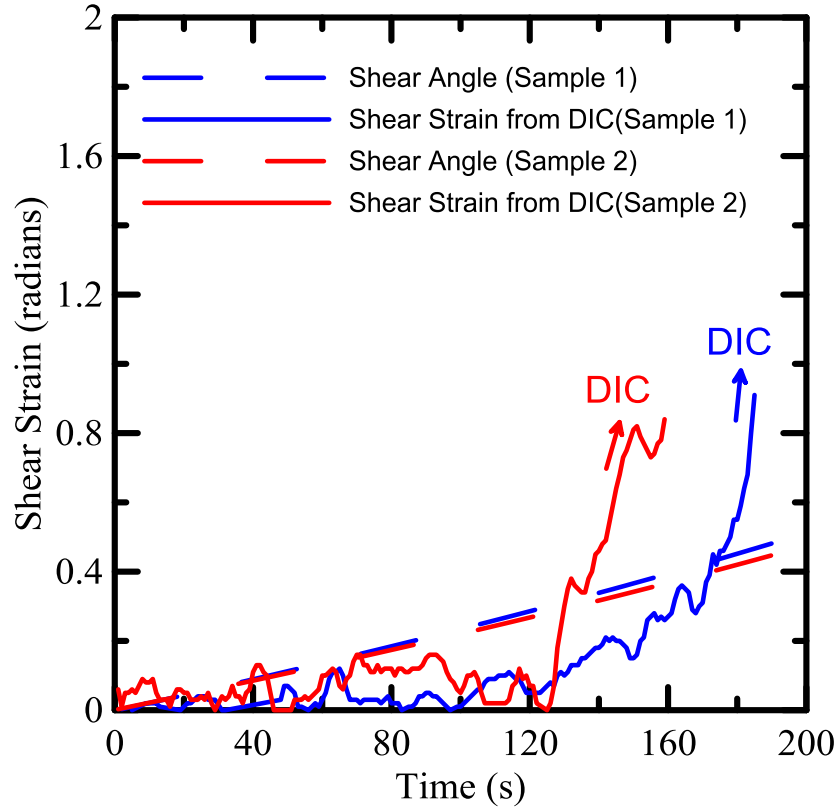


Figure 3.36 Shear strain from DIC versus shear angle

3.14 Constitutive Model for Calculating Shear Stress

A constitutive model was set up to explain the shear stress behavior in terms of shear angle. Shear stress – angle relationship for two sets of experiments has been derived here. Data sets used were S1 – T1- 0° (75 mm x 75 mm, Thickness = 5.0 mm, 0°, Textile 1) and S1 – T1-45° (75 mm x 75 mm, Thickness = 5.0 mm, 45°, Textile 1). As cross-section and thickness do not have any major effect on shear properties therefore model for S1 – T1 - 0° can be used for S2 – T1 - 0° and S1 – T2 - 0° and model for S1 – T1 - 45° can be used for S1 – T2 - 45° as well with some tolerance. Two layered of textile 1 is considered here only. Shear stress is almost linear till the point of cracking and decreases from there

on. Shear stress pattern can thereafter be explained by divided into two parts, elastic region (before cracking) and post peak region (after cracking).

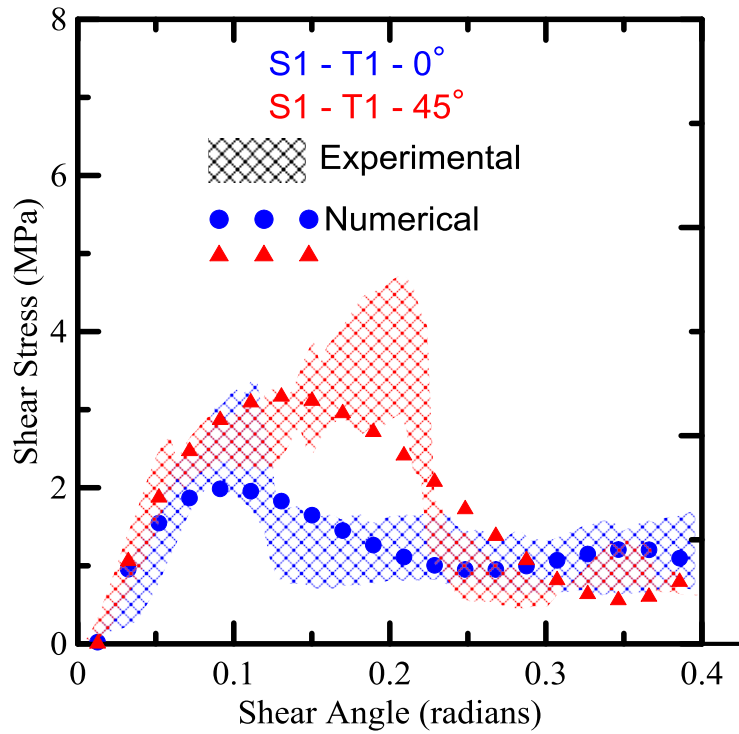


Figure 3.37 Constitutive model to calculate the shear stress

Shear stress-angle relationship has been assumed to be fourth order equation given by:

$$\tau_{xy} \text{ (MPa)} = C_1\gamma_{xy}^4 + C_2\gamma_{xy}^3 + C_3\gamma_{xy}^2 + C_4\gamma_{xy} + C_5$$

Where the shear angle, γ_{xy} is measured in radians.

| S1 – T1 - 0° | | S1 – T1 - 45° | |
|------------------|---------------|-----------------|---------------|
| $C_1 = -2052.22$ | $C_4 = 72.44$ | $C_1 = 0.00$ | $C_4 = 69.37$ |
| $C_2 = 1943.31$ | $C_5 = -0.80$ | $C_2 = 502.72$ | $C_5 = -0.79$ |
| $C_3 = -619.29$ | | $C_3 = -362.88$ | |

Similarly shear strain hardening-softening model as discussed in section 1.2 can be developed for predicting shear response here as well with the different stages as marked in figure 3.38.

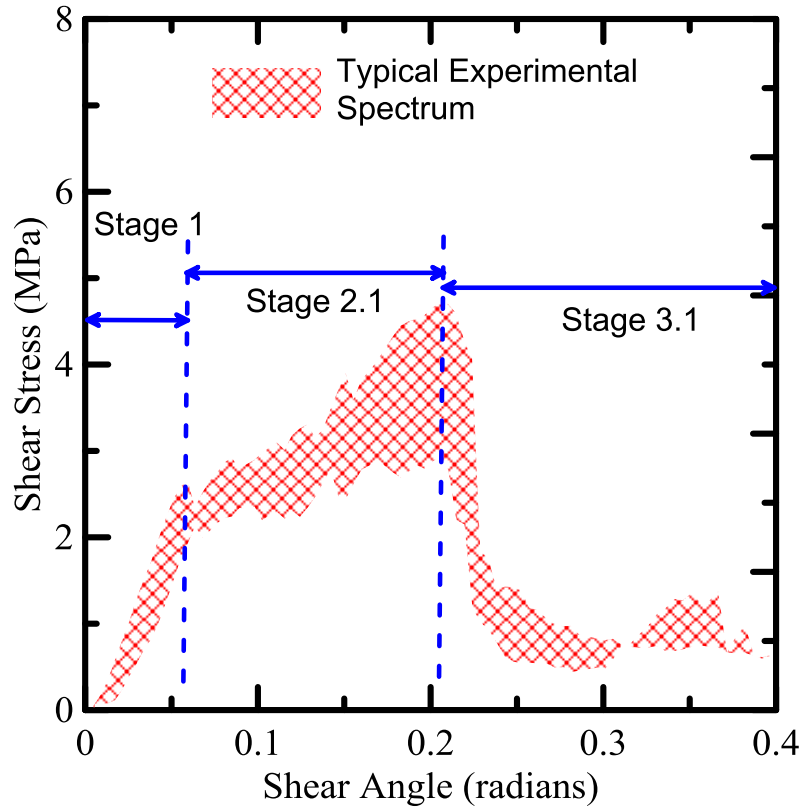


Figure 3.38 Different stage during the experiment

3.1 Crack Pattern

Failure pattern of the all the six combinations is shown below. Failure pattern, origin of crack, direction of penetration and number of cracks were a function of design parameters chosen. Although the samples did not crack in a uniform or a well-defined manner but the basic pattern is discussed.

S1 – T1 - 0° (75mm x 75mm, Thickness = 5.0 mm, 0°)

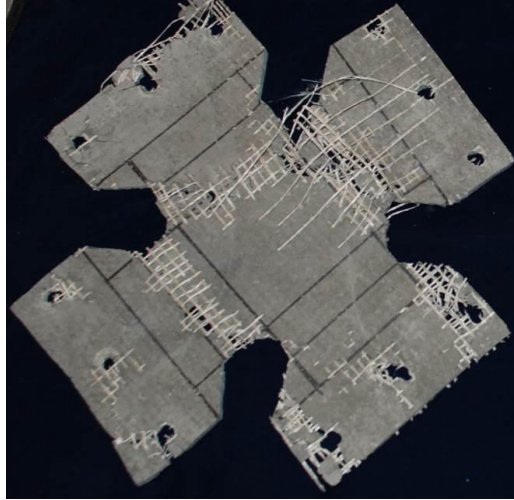


Figure 3.39 Crack pattern for S1 – T1 - 0°

For S1-T1- 0 samples, failure was seen to occur along the edges as shown in figure 3.39. Matrix failure was mostly governed by tension in y-direction and therefore textile pullout can be seen at places where paste had de-bonded.

S1 – T1 - 45° (75mm x 75mm, Thickness = 5.0 mm, 45°)

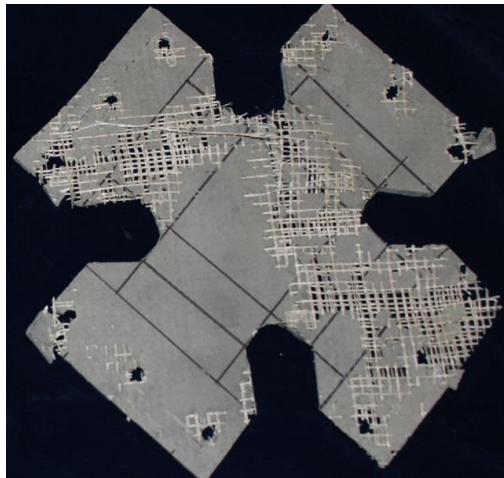


Figure 3.40 Crack pattern for S1 – T1 - 45°

Failure of S1 – T1 - 45° was as shown in figure 3.40. Yarns of textile were oriented along the global y direction. As the effect of textile is very high in tension therefore compressive buckling failure takes place along the center. Failure in paste is the governing design aspect for this combination.

S2 – T1 - 0° (50 mm x 50 mm, Thickness = 5.0 mm, 0°)

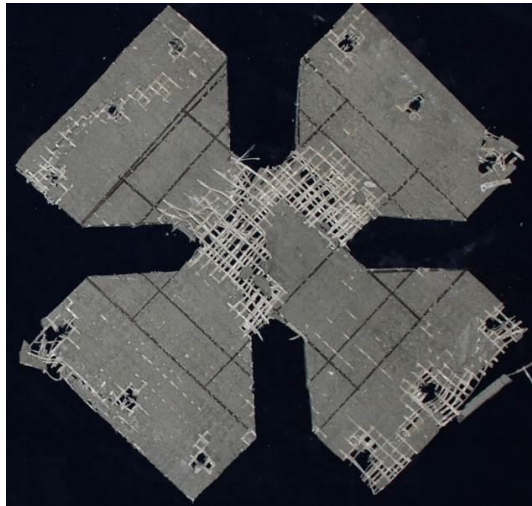


Figure 3.41 Crack pattern for S2 – T1 - 0°

Failure was seen to occur along the edges similar to S1-T1-0°. Matrix failure was mostly governed by tension in y-direction and therefore textile pullout can be seen at places where paste had de-bonded.

S1 – T0 - 0° (75mm x 75mm, Thickness = 4 mm, 0°)

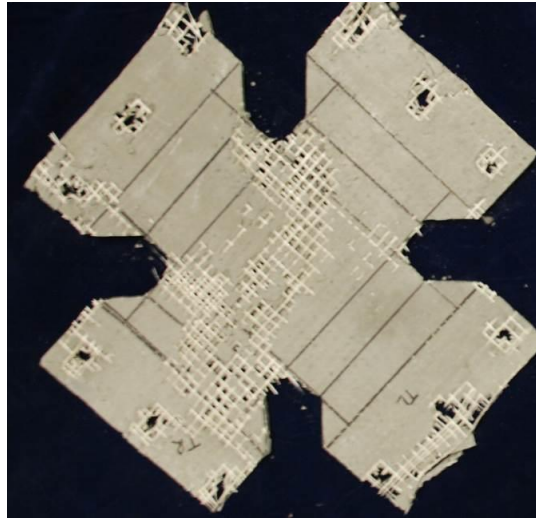


Figure 3.42 Crack pattern for S1 – T0 - 0°

Additional samples were made to understand the transition of failure pattern from being governed by compression buckling to tension and visa-versa. It was hypothesized that this might be a function of thickness of samples and therefore samples with thickness of 4.0 mm were tested with the cross-section and orientation maintained at S1 and 0°. As the thickness decreased to 4.0 mm it was observed that the failure mode was compressive buckling in global x-direction with the main crack traversing through the sample in the direction of loading. Therefore it was concluded that the amount of paste controlled the failure pattern. For c/s S1 and orientation 0°, samples with thickness 5.0 mm failed due to compressive buckling and thicker samples failed due to tension.

S1 – T2 - 0° (75 mm x 75 mm, Thickness = 6.5 mm, 0°)

When one compares S1 (75 mm x 75 mm) samples at thickness 4.0 mm, 5.0 mm and 6.5 mm, one can observe that mode of failure goes from compressive buckling at center to

tensile failure at the edges. Similarly in this sample as well it can be seen that mode of failure is tensile with cracks at edges only.

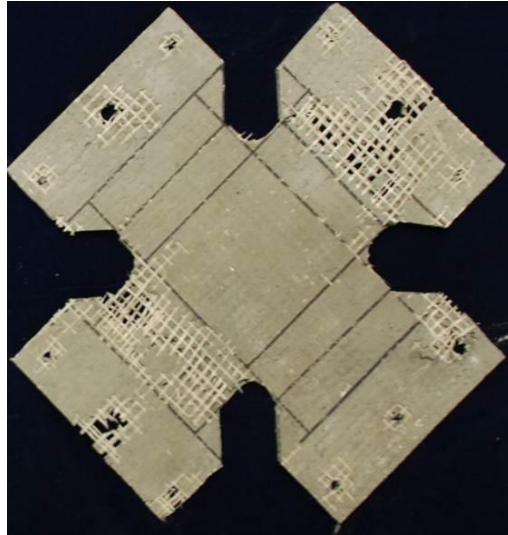


Figure 3.43 Crack pattern for S1 – T2 - 0°

Textile 2 – S1, T2, 0° (Textile 2 - 75mm x 75mm ,Thickness = 6.5 mm, 0°)



Figure 3.44 Crack pattern for Textile 2 – S1 – T2 - 0°

Textile 2 had thicker and denser yarns with higher surface area for bonding with the paste. Sample was of thickness 2 and it failed due to tensile force. Failure of paste was more predominant.

Comparing the failure pattern between the orientations 0° and 45° , one can observe that 0° had a deflection type of dislocation as shown in figure 3.45 (a). This configuration is therefore providing more of a frictional resistance instead of direct tension when compared to 45° configuration and therefore has lower capacity.

Textile Orientation - 0°



Textile Orientation - 45°

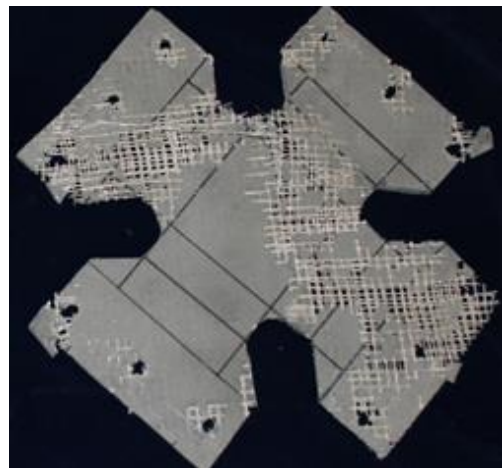


Figure 3.45 Comparison between orientations

4. REFERENCES

1. Brameshuber W., "Textile Reinforced Concrete", State-of-the-Art Report of RILEM Technical Committee 201-TRC, RILEM Report 36, pg 1-271, 2006.
2. Dey V., "Low velocity impact properties of sandwich insulated panels with textile-reinforced concrete skin and aerated core", MAI 51/04(E) - Thesis 1531165, 2012.
3. Hegger J., "Textile Reinforced Concrete", Proceedings of the 1st International RILEM Symposium", RILEM Proceedings PRO 50, pg 1-389, 2006.
4. Mobasher B., Destree X., "Design and construction aspects of steel fiber-reinforced concrete elevated slabs", Fiber Reinforced Self-Consolidating Concrete: Research and Applications, ACI Symposium Publication 274, pp 95-107, 2010.
5. Mobasher, B., "Micromechanical Modeling Of Angle Ply Cement Based Composites," Proc., 6th Int. Sym. on Brittle Matrix Comp., (BMC6) Warsaw, Poland, Woodhead Publishing Limited, pp 62-772. Oct. 2000.
6. Soranakom C, Mobasher B. Correlation of tensile and flexural response of strain softening and strain hardening cement composites. *Cem Concr Compos*, 2008;30:465-477.
7. Mobasher, *Mechanics of Textile and Fiber reinforced cement composites*, CRC press, 470 p, 2011.
8. Soranakom C, Mobasher B. Correlation of tensile and flexural response of strain softening and strain hardening cement composites. *Cem Concr Compos*;30:465-477, 2008.
9. A. Peled, and B. Mobasher, "Cement Based Pultruded Composites with Fabrics," Proceedings, 7th International Symposium on Brittle Matrix Composites (BMC7), Warsaw, Poland, pp. 505-514, 2003.
10. Peled, A., Mobasher, B., "Effect Of Processing On Mechanical Properties Of Textile - Reinforced Concrete," Textile Reinforced Concrete (TRC) - Symposium sponsored by the ACI Committees 549-544, ACI Special Publications, in review, 2007.
11. Barros J.O., Destree X., Mobasher B., et al. " Report on Design and Construction of Steel Fiber-Reinforced Concrete Elevated Slabs", ETR Report, ACI Committee 544, in review, 2014.

-
12. Quintas V., “Two main methods for yield line analysis of slabs”, *Journal of engineering mech*, 2003
 13. Kennedy G., Goodchild C., “Practical yield line design”, *Reinforced concrete council*, 2003.
 14. Scott M.H., Fenves G.L., “Plastic Hinge Integration Methods for Force-Based Beam–Column Elements”, *Structural engineering*, Volume 132, Issue 2, pg. 244-252, 2006.
 15. Kheyroddin A., Naderpour H., “Plastic hinge rotation capacity of reinforced concrete beams”, *International Journal of Civil Engineering*. Vol. 5, No. 1, 2007.
 16. Haskett M., Oehlers D.J., “Rigid body moment–rotation mechanism for reinforced concrete beam hinges”, *Engineering structures*, Vol. 31, issue 5 pg 1032-1041, May 2009.
 17. Baker A., “Ultimate load theory applied to the design of reinforced and prestressed concrete frames”, London: Concrete Publications Ltd., . p. 91, 1956.
 18. Sawyer H., “Design of concrete frames for two failure states”, *Proceedings of the international symposium on the flexural mechanics of reinforced concrete*, ASCE-ACI, p. 405-31, 1964.
 19. Corley G., “Rotation capacity of reinforced concrete beams”, *J Struct Eng, ASCE*, 92(ST10), 121-146, 1966.
 20. Mattock A., “Discussion of rotational capacity of reinforced concrete beams”, *J Struct Div ASCE* , 93(2) 519-522, 1967.
 21. Foster S.J., Bailey C.G. et al., “Experimental behavior of concrete floor slabs at large displacements”, *Engineering structures* 26, pg 1231-1247, 2004.
 22. Soranakom C., Mobasher B., Destree X., “Numerical simulation of FRC round panel tests and full scale elevated slabs”, *ACI SP-248-3*, pg 31-40, 2008.
 23. Khaloo A.R., Afshari M., “Flexural behavior of small steel fiber reinforced concrete slabs”, *Cement and concrete composites* 27, pg 141-149, 2005.
 24. Mobasher, B., “Mechanics of Fiber and Textile Reinforced Cement Composites”, CRC press, 2011, p. 480, ISBN: 9781439806609.
 25. ASTM C1550-12a, “Standard test method for flexural toughness of fiber reinforced concrete (using centrally loaded round panel)”, *Book of standards volume 04.02*, 2012.

-
26. Johansen K.W., "Yield line formulae for slabs", Translated by cement and concrete association, London, Ref. 12.044, pp 106, 1972.
 27. Hegger J., Will N., "Load-bearing behavior and simulation of textile reinforced concrete", *Materials and Structures*, Volume 39, Issue 8, pp 765-776, Oct. 2006.
 28. Contamine R., Junes A., Larbi A.S., "Tensile and in-plane shear behavior of textile reinforced concrete: Analysis of a new multi-scale reinforcement", *Construction and Building Materials* vol. 51, page 405-413, Jan. 2014.
 29. Taha, Abdin Y, Ebeid S., " Comparison of picture frame and bias-extension tests for the characterization of shear behavior in natural fiber woven fabrics", *Fibers and Polymers*, Vol. 14, No. 2, pg 338-344, 2013.
 30. Harrison P., Clifford M.J., "Shear characterization of viscous woven textile composites: a comparison between picture frame and bias extension experiments", *Composites science and technology* vol. 64, pg 1453-1465, 2004.
 31. Zhu D., "Experimental study and finite element modeling of woven fabrics", 2009.
 32. Yao Y., "Application of 2-D Digital Image Correlation (DIC) method to Damage Characterization of Cementitious Composites under Dynamic Tensile Loads", MAI 52/02(E), Thesis 1543310, 2013.
 33. Post D., "Moiré Interferometry at VPI and SU". *Experimental Mechanics*, 23(2), 203-210, 1983.
 34. Fottenburg, W. G., "Some Applications of Holographic Interferometry", *Experimental Mechanics*, 8, 281-285, 1969.
 35. Wang, Y. Y., Chen, D. J. and Chiang, F. P., "Material testing by computer aided speckle interferometry", *Experimental Techniques*, 17(5), 30-32, 1993.
 36. Po-Chih Hung and A. S. Voloshin, "In-plane strain measurement by digital image correlation", *J. Braz. Soc. Mech. Sci. & Eng.* vol.25 no.3 Rio de Janeiro July/Sept. 2003.
 37. Bastawros, A. F. and Voloshin, A. S., "Thermal Strain Measurements in Electronic Packages through Fractional Fringe Moiré Interferometry", *Journal of Electronic Packaging*, 112(4), 303-308, 1990.
 38. Sutton, M. A., Wolters, W. J., Peters, et al., "Determination of Displacements Using an Improved Digital Correlation Method", *Image and Vision Computing*, 1(3), 133-139, 1983.

-
39. Sutton, M. A., Cheng, M. Q., Peters, W. H., et. al., "Application of an Optimized Digital Correlation Method to Planar Deformation Analysis", *Image and Vision Computing*, 4(3), 143-151, 1986.
 40. Sutton, M. A., McNeill, S. R., Jang, J. and Babai, M., "Effects of Subpixel Image Restoration on Digital Correlation Error", *Journal of Optical Engineering*, 27(10), 870-877, 1988.
 41. Sutton, M. A., Turner, J. L., Bruck, H. A. and Chae, T. A., "Full-field Representation of Discretely Sampled Surface Deformation for Displacement and Strain Analysis", *Experimental Mechanics*, 31(2), 168-177, 1991.
 42. Bruck, H. A., McNeil, S. R., Sutton, M. A. and Peters, W. H., "Digital Image Correlation Using Newton-Raphson Method of Partial Differential Correction", *Experimental Mechanics*, 29(3), 261-267, 1989.
 43. Tung, S., Shih, M., Kuo, J., "Application of digital image correlation for anisotropic plastic deformation during tension testing", *Optics and Lasers in Engineering* 48, 636-641, 2010.
 44. F.M. Sánchez-Arévalo, T. García-Fernández, G. Pulos, and M. Villagrán-Muniz, "Use of digital speckle pattern correlation for strain measurements in a CuAlBe shape memory alloy", *Materials Characterization*, 60, 775–782, 2009.
 45. Stephen R. Heinz, Jeffrey S. Wiggins, "Uniaxial compression analysis of glassy polymer networks using digital image correlation", *Polymer Testing* 29 925–932, 2010.
 46. S.Sozen, and M.Guler, "Determination of displacement distributions in bolted steel tension elements using digital image techniques", *Optics and Lasers in Engineering* 49, 1428–1435, 2011.
 47. X.F. Yao, L.B. Meng, J.C. Jin, H.Y. Yeh, "Full-field deformation measurement of fiber composite pressure vessel using digital speckle correlation method", *Polymer Testing* 24, 245–251, 2005.
 48. Ghiassi, B., Xavier, J., Oliveira, D.V., Lourenço, P.B., "Application of Digital Image Correlation in Investigating the Bond Between FRP and Masonry", *Composite Structures*, 2013
 49. R.L. VijayaKumar, M.R.Bhat,C.R.L.Murthy, "Evaluation of kissing bond in composite adhesive lap joints using digital image correlation", *International Journal of Adhesion & Adhesives* 42 pg 60–68, 2013.

-
50. S. Giancane, F.W. Panella, R. Nobile, V. Dattoma, “Fatigue damage evolution of fiber reinforced composites with digital image correlation analysis”, *Procedia Engineering* 2 1307-1315, 2010.
 51. François Hild, Stephane Roux, Nestor Guerrero, et. al., “Calibration of constitutive models of steel beams subject to local buckling by using digital image correlation”, *European Journal of Mechanics A/Solids* 30 pg 1-10, 2011.
 52. Simon Rouchier, Genevieve Foray, Nathalie Godin, “Damage monitoring in fibre reinforced mortar by combined digital image correlation and acoustic emission”, *Construction and Building Materials* 38 pg 371–380, 2013.
 53. Cristina Goidescu, Helene Weleman, Christian Garnier, et. al., “Damage investigation in CFRP composites using full-field measurement techniques: Combination of digital image stereo-correlation, infrared thermography and X-ray tomography”, *Composites: Part B* 48 pg 95–105, 2013.
 54. Yihong He, Andrew Makeev, Brian Shonkwiler, “Characterization of nonlinear shear properties for composite materials using digital image correlation and finite element analysis”, *Composites Science and Technology* 73, pg 64–71, 2012.
 55. Sutton A., Jose O., Hubert W. S., “Image correlation for shape motion and deformation measurements, basic concepts, theory and applications”, 1st ed. New York: Springer publications, 2009.
 56. Correlated Solutions, “Digital Image Correlation: Overview of Principles and Software”, Short-course, 2014.
 57. Bruckner A., Ortlepp R., Curbach M., “Textile reinforced concrete for strengthening in bending and shear”, *Materials and structures*, vol. 39, issue 8, pp 741-748, Oct. 2006.